University of London

Solution-Processable Carbon Nanotube Molecular Junctions

Joseph McMorrow

Supervisor:

Dr. Matteo Palma

Submitted in partial fulfilment of the requirements of the Degree of Doctor of Philosophy

Statement of Originality

I, Joseph McMorrow, confirm that the research included within this thesis is my own work or that where it has been carried out in collaboration with, or supported by others, that this is duly acknowledged below and my contribution indicated. Previously published material is also acknowledged below.

I attest that I have exercised reasonable care to ensure that the work is original, and does not to the best of my knowledge break any UK law, infringe any third party's copyright or other Intellectual Property Right, or contain any confidential material.

I accept that the College has the right to use plagiarism detection software to check the electronic version of the thesis.

I confirm that this thesis has not been previously submitted for the award of a degree by this or any other university.

The copyright of this thesis rests with the author and no quotation from it or information derived from it may be published without the prior written consent of the author.

Details of collaboration and publications:

J. Zhu, J. McMorrow, R. Crespo-Otero, G. Ao, M. Zheng, W. P. Gillin, and M. Palma; *J. Am. Chem. Soc.*, 2016, 138, 2905-2908.

J. McMorrow, M. Freeley, and M. Palma; *Ind. Eng. Chem. Res.*, 2017, 56, 5302–5308.

Signature: J. McMorrow

Date: 30th August 2017

Abstract

Nanotechnology is the manipulation of matter at the supramolecular, molecular and atomic scale. As a result, nanotechnology is included in various fields of science including surface science, organic chemistry, molecular biology, semiconductor physics, microfabrication and molecular engineering. One of the ambitions for nanotechnology is to develop electrical devices where the active component is a single molecule or nanomoiety. In order to fabricate such devices, it is of paramount importance to develop strategies beyond the current top-down lithographic approaches typically employed in the semiconductor industry. In this regard, the ability to control the assembly of single-molecules and individual nanomoieties directly in solution can allow for the development of solution-processable approaches in nanotechnology, towards the fabrication of single-molecule devices.

In this thesis, it will be discussed how molecular junctions with functional single molecules are fabricated in aqueous solutions employing single-walled carbon nanotubes as potential nanoelectrodes. Furthermore, it will be demonstrated how the assembly of molecular junctions can facilitate other functions and the construction of both nanostructures and microstructures.

To begin, relevant work will be discussed that has been done in this field to date and outline clear ambitions of the study presented here. Subsequently, the key characterisation techniques that underpin all the results in this study will be described. In this work, it will be reported how metallic carbon nanotubes can act as nanoelectrodes in molecular junction assemblies and how conductive measurements of individual molecules are performed. Therefore, for the first time, the molecular junction conductance of a series of oligophenyls were successfully measured, which were formed *via* a solution-based assembly method. Measured molecular conductance values of the series of oligophenyls resulted in a β value of 0.5 $Å^{-1}$.

Furthermore, it will be described how the approach outlined previously can be extended to the synthesis of tri-amine molecular linkers as well as the formation of three-terminal junctions as

the foundation of carbon nanotube-based single-molecule electronic devices. This research resulted in an increase in the formation of Y-shape molecular junctions by ~25%.

Next, this report will outline the formation of molecular junctions in two-dimensional structures, which can allow for the development of electrical devices into networks. Utilising modified DNA sequences, “click” chemistry can lead to nanotube network with dimensions ranging into the micrometre scale. Building on this work, it will be further report on the change in physical properties when these two-dimensional superstructures are embedded into polymeric thin films. Finally, conclusions of the research will be drawn and it will be discussed how the findings obtained in this work can contribute to the development of novel single-molecule electronic devices.

Table of Contents

List of Abbreviations

$(Boc)_2O$ - di-tert-butyl dicarbonate

(n,m) – integers in the vector equation

°C – degrees Celsius

µL – microliter

µm – micrometres

$1/r^{12}$ – dominated at short distance, models repulsion forces

1/r6 – dominated at large distance, constitutes attraction forces

1D – one-dimensional

^1H – proton

2D – two-dimensional

2Δ – tip broadening coefficient

Å – angstroms

a_1, a_2 - unit vectors in graphene in space (0.246 nm)

AFM – atomic force microscopy

Ar – argon

ATPE – aqueous two-phase extraction

Au – gold

BDT – 1,4-benedithiol

Boc - tert-Butyloxycarbonyl

ca. - circa

C-AFM – conductive atomic force microscopy

$CDCl_3$ – deuterated chloroform

C_h – chiral vector

cm – centimetre

CNTs – carbon nanotubes

CoMoCAT – cobalt and molybdenum catalyst

COSY – correlation spectroscopy

Cr – Chromium

Cu – copper

$Cu(OAC)_2$ – copper acetate

CuAAC – copper azide-alkyne cycloaddition

$CuSO_4.5H_2O$ – copper sulfate

CVD – chemical vapour deposition

d – diameter

d – doublet

DAF – diaminofluorene

DCM – dichloromethane

dd – doublet of doublets

DFT – density functional theory

DGU – density gradient ultracentrifugation

DI – deionised

Dianiline - 4,4'-(ethyne-1,2-diyl)dianiline

DMF – dimethylformamide

DMSO – dimethyl sulfoxide

DNA – deoxyribose nucleic acid

DNA-SWCNTs – DNA-wrapped single-walled carbon nanotubes

ds-DNA – double-stranded DNA

e-beam – electron beam

EBJs – electromigrated break junctions

EDC - 1-Ethyl-3-(3-dimethylaminopropyl)carbodiimide

EDS – energy dispersive spectroscopy

e.g. – for example

et al. – and others

EtOAc – ethyl acetate

eV – electronvolt

ε - depth of potential well

FET – field-effect transistor

FTIR – Fourier transform infrared spectroscopy

g – gram

G – molecular conductance

G_0 – quantum of conductance

GTACU – guanine, thymine, adenine, cytosine, uracil

h – height

H_2O – water

H_2O_2 – hydrogen peroxide

H_2SO_4 – sulfuric acid

HCl - hydrochloric acid

HiPCO – high pressure carbon monoxide

HMMD – hexamethylenediamine

IEX – ion exchange chromatography

IR – infrared

I-V - current-voltage

J – coupling constant

i.e. – id est

K_2CO_3 – potassium carbonate

KΩ – kilo ohm

kJ/mol – kilojoules per mole

L – tunnelling distance taken to be the length of the molecule

M – molar

m – multiplet

MCBJs – mechanically controllable break junctions

MeCN – acetonitrile

MES – 2-(*N*-morpholino)ethanesulfonic acid

mg – milligram

$MgSO_4$ – magnesium sulfate

MHz – megahertz

mL – millilitre

mM – millimolar

mmol – millimole

mol – mole

MTJs – molecular transport junctions

MWCNTs – multi-walled carbon nanotubes

MΩ – megaohm

N/m – Newton/meter

NaCl – sodium chloride

NEt_3 – trimethylamine

NIST – National Institute of Standards and Technology

nm – nanometres

NMP – N-methyl-2-pyrrolidone

NMR – nuclear magnetic resonance

ϕ – wrapping angle

PCR – polymerase chain reaction

Pd – Palladium

$Pd(dba)_3$ – Tris(dibenzylideneacetone)dipalladium(0)

pm – picometre

PMMA – poly(methyl methacrylate)

PPD – p-phenylenediamine

ppm – parts per million

PVA – polyvinyl alcohol

r - inter-atomic distance (separation between particles)

R – radius

R – resistance

R_c – contact resistance

s – singlet

SAM – self-assembled monolayer

SEM – scanning electron microscopy

SiO_2 – silicon dioxide

ss-DNA – single-stranded DNA

STM – scanning tunnelling microscopy

STS – scanning tunnelling spectroscopy

Sulfo-NHS – N-hydroxysulfosuccinimide

SWCNTs – single-walled carbon nanotubes

t – triplet

t-BuOH – tert-butanol

TEM – transmission electron microscopy

Terphenyl - 4,4”-diamino-p-terphenyl

THF – tetrahydrofuran

TLC - thin layer chromatography

TPBS – tris phosphate buffered saline

V – intermolecular potential between two molecules or atoms

W_E – width effective

W_m – width measured

XPhos – 2-dicyclohexylphosphino-2’,4’,6’-triisopropylbiphenyl

β – decay constant

δ – chemical shift

π – pi

Ω – ohm

σ – the distance in which the intermolecular potential between two particles is zero

Acknowledgements

First of all, I would like to thank my PhD supervisor, Dr. Matteo Palma – I will always be grateful for you giving me the opportunity to contribute to an area of science that has always been of great interest. You took a chance on me and I have done my utmost to repay your faith. Notably, you gave me the opportunity to present our research findings at the ACS National Meeting in San Diego, an experience that will stay with me forever. We published two papers together and you taught me much about scientific rigour – it was an excellent experience working with you.

Secondly I would like to thank my thesis examiners, Dr. Christoph G. Salzmann and Dr. Emiliano Bilotti for taking the time out of their busy schedules to read and critique my work. I would also like to thank all panel members who have helped contribute to research with rigorous questioning and challenges: Prof. Stephen Goldup, Dr. Devis Di Tommaso and Dr. Ali Zarbakhsh.

Next I would like to thank all those who I worked with at QMUL. The Matteo Palma Research Group: Jingyuan, Mark, Da, Antonio, Sandra, Pierrick, Arpita, Piratheep, Haajirah, Giuseppe, Qingyu, Xinzhao, Nasir. To those outside of the group: Linda, Martina, Piera, Fosca, John, Jamie, Jess Groppi, Marzia, Geoff, Harry, Siobhan, Gabriele, Giorgio, Angelo, Rosemary, Cecile, Lazaros, Luca, Mariya, Nolwenn and Guido. Also, I would like to thank Aghar Shah and Jay Chumber for their help with suppliers and getting samples sent out in record time. I would like to thank collaborators in New York and Cardiff for their support in various projects. In particular, I would like to thank Ed Neal and Jess Pancholi for their continued support by proof-reading my thesis and interpreting mass spec data, as well as being my click chemistry consultants – I owe you both a great debt.

I would like to thank my friends outside of the lab who have helped me in their own special ways. Grant Murphy for his continual support by reminding me of what really matters in life: football, films and Batman. I want to thank Daniel Walsh; your stories are the greatest and I can say, comfortably, that I have never met anyone like you. Thank you to all my school friends who probably never saw a PhD coming – neither did I.

I want to thank all my extended family for their support. In particular, my London-based relatives for letting me sleep over and spending time with you all, thank you so much.

Most importantly, I want to thank my family. My parents have no idea what chemistry is, so they are just taking my word for it. Mum and dad, you refused to give up on me when I was at my lowest and saw something in me that I did not. As always, your faith has led to something greater. To my brothers and sister: Amos, Tez, Eddie and Anthony, I owe you every achievement and all success. For better or worse, you have made me who I am and gave me the motivation to strive for more. You have all given me a mentality that was imperative for my PhD journey and will continue to reward me for the rest of my life. To my nephews and nieces: Omar, Jamie, Grace, Gabi, Florence, Leo and Lexi, I hope you all know how important you are to me and, in your own ways, have helped me get through a long journey.

To everyone, thank you for your unwavering support throughout. The McMorrow family have gone through a lot over the past four years and your love and support has not gone unnoticed. I could not have done this without you. I love you all very much.

Per te, nonno

1.0 Introduction

Nanotechnology is the manipulation of matter at the supramolecular, molecular and atomic scale. A general description of nanotechnology was proposed by the National Nanotechnology Initiative, which provided the following definition: "*the manipulation of matter with at least one dimension sized from 1 to 100 nanometres*".[1] This definition reflects the fact that quantum mechanical effects are important considerations at this scale. Therefore, the research category is inclusive of all types of studies and technologies that deal with the special properties of matter that occur below the given size threshold.

The very broad definition means nanotechnology is included in various fields of science including surface science, organic chemistry, molecular biology, semiconductor physics, microfabrication, molecular engineering, etc.[2] Nanotechnology research and applications are equally diverse, ranging from extensions of conventional device physics to completely new approaches based upon molecular self-assembly, and from developing new nanoscale materials to direct control of matter on the atomic scale.[3–5]

Throughout history, several advances were unwitting developments to nanotechnology. For instance, nanoparticles are typically associated with modern science, however in the 9th century, Mesopotamian artisans were using nanoparticles to create glittering effects on the surface pots.[6] The earliest evidence of the use and application of nanotechnology can be traced back to carbon nanotubes (cementite nanowires) found in the microstructure of wootz steel manufactured in ancient India around 600 BC, which were exported globally.[7] Carbon nanotubes (CNTs) are used in this study and represent a relatively novel material with large potential for future applications in advancing nanotechnology further.

Carbon-based nanomaterials represent an important aspect of nanotechnology as they have integral properties that facilitate the production of single-molecule electrical devices, one of the ultimate goals for nanotechnology. Furthermore, it is also important to control the assembly

of carbon-based nanomaterials in the fabrication of nanotechnology systems and devices. However, current top-down lithographic fabrication strategies are often expensive and time-consuming. To overcome these drawbacks, it has been considered to assemble functional architectures directly in solution, ideally with single-molecule control. This will allow the development of solution-processable strategies for the fabrication of nanoscale, and single-molecule, electronic devices.

1.1. Carbon Nanotubes

1.1.1. Discovery, Synthesis and Applications

Since their discovery in 1991, CNTs have been the focal point of substantial research.[8] CNTs are allotropes of carbon in a hollow cylindrical shape with sp^2 hybridisation, forming hexagonal benzene-like rings. Possessing a high aspect ratio (*i.e.* length/diameter), CNTs have diameters in the range of nanometres and lengths reaching micrometres. They are often described as nanowires due to their size and ballistic one-dimensional configuration and, depending on structure, can be classified as single-walled (SWCNTs) or multi-walled (MWCNTs) as shown in Figure 1. CNTs can also be divided by their electronic conductive properties, *i.e.* whether they possess semiconducting or metallic character.

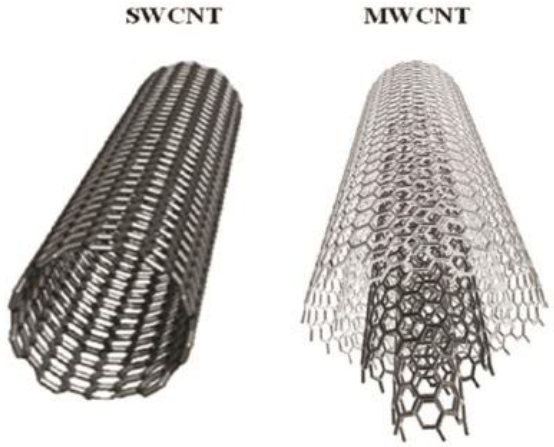

Figure 1. Schematic showing a) single and b) multi-walled carbon nanotubes.

Nanotubes possess exceptional structural, mechanical and electronic properties due to their unique combination of inherent dimensions, structure and topology. As a result, CNTs are extremely strong (tensile strength up to 63GPa), highly conducting (4.0×10^9 A/cm^2) and demonstrate high thermal (3500 W·m^{-1}·K^{-1}) and chemical stability.[9,10] They have also shown significant elasticity and over 100 times the tensile strength of steel.[11] Due to these properties, CNTs have been proposed as materials for many applications ranging from scanning probes and hydrogen storage to biosensors.[12–14] Several techniques are commonly used to synthesise CNTs – most notably, these techniques include arc discharge, chemical vapour deposition (CVD) and laser ablation.[15–17]

1.1.2. Nanotube Indices Naming Scheme

When describing the structure of nanotubes, SWCNTs can be considered as wrapping a graphene sheet (one-atom-thick, hexagonally-arranged, two-dimensional sheet of carbon) into a seamless hollow cylinder. Nanotubes are represented as a pair of indices known as the chiral vector (*n*,*m*), where *n* and *m* are integers that denote the number of unit vectors along two directions in the honeycomb crystal lattice of graphene.[18] *n* and *m* represent integers in the vector equation shown in Equation 1.

Equation 1. Chiral vector calculation using indices.

$$C_h = na_1 + ma_2$$

Where: C_h: chiral vector; a_1 and a_2: unit vectors in graphene in space

The (*n*,*m*) nanotube naming scheme describes how a graphene sheet is "wrapped up" and is illustrated in Figure 2.[19]

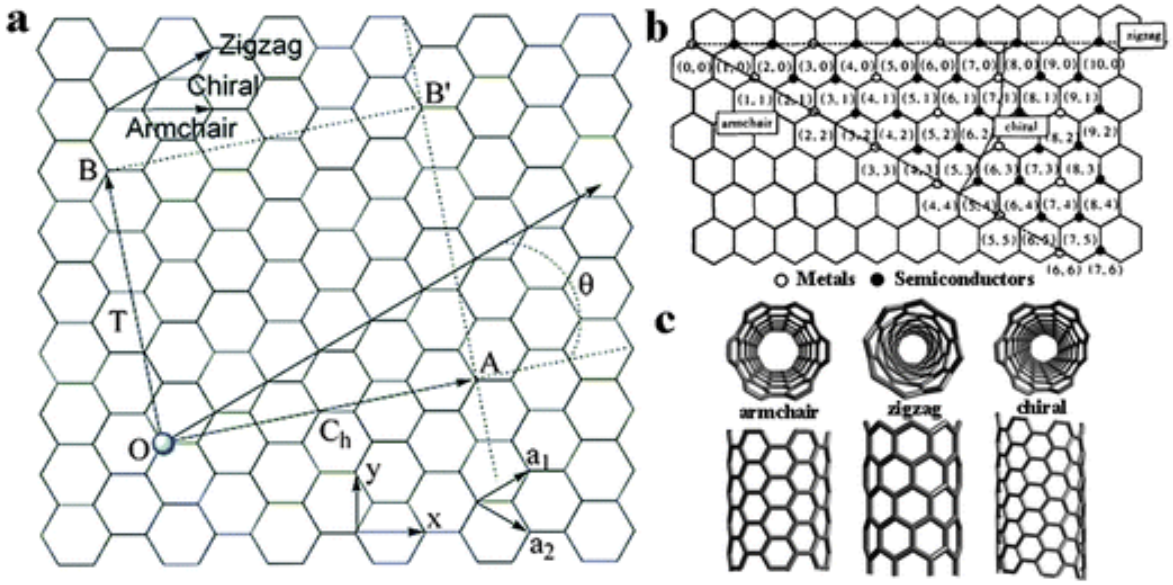

Figure 2. a) Schematic plot of C*h* in a graphene sheet. b) Schematic illustrating the relationship between indices (*n*,*m*) and nanotube electronic properties. c) Structure of CNTs in armchair, zigzag and chiral configurations. Reprinted with permission from Chem. Soc. Rev. ***40,*** *1324–1336 (2011).* Copyright 2011 Chemical Society Reviews.

The way graphene sheets wrap up will dictate the overall structure and ultimately the properties of nanotubes. If $n = m$, the CNTs take up an orientation known as the *armchair* configuration. If the wrapping angle, ϕ (not shown in Figure 2) is 30° from the "armchair" line, *i.e.* if $m = 0$, then the nanotube is described as forming a *zigzag* configuration. Otherwise, if $0° < \phi < 30°$ then the nanotube is structured as a *chiral* configuration. Indices also determine whether SWCNTs are metallic or semiconducting, as well as the band gap they possess. When: $m - n = 3k$, where k is an integer, the nanotube is metallic, but if $m - n = 3k \pm 1$ the nanotube is semiconducting. Metallic or semiconducting character is observed due to variation in the band gap from zero to 2 eV.[18,20,21] Using (*n*,*m*) indices, the diameter of an ideal nanotube can be calculated as shown in Equation 2.

Equation 2. Diameter calculation using carbon nanotube indices

$$d = \frac{a}{\pi}\sqrt{(n^2 + nm + m^2)} = 78.3\sqrt{((n+m)^2 - nm)}\text{pm}$$

Where a = 0.246 nm. (shown as a_1 and a_2 in Figure 2).

Nanometre dimensions combined with versatile electrical and excellent conductive properties mean SWCNTs are ideal candidates for assembling miniaturised electronic devices.[22,23] The potential for nanotubes to be embedded in electrical devices was first realised in 2001 when the first intermolecular logic gate using SWCNT field-effect transistor was produced.[24]

In 1999, Hiromichi Kataura designed a theoretical graph based on CNT band structure calculations.[25] A Kataura plot relates the nanotube diameter and its bandgap energies for all nanotubes in a diameter range, as shown in Figure 3.[26] The oscillating shape of every branch of the Kataura plot reflects the dependence of the SWCNT properties on the (*n*,*m*) index rather than on its diameter. For instance, (10,1) and (8,3) nanotubes have very similar diameters but the former is metallic and the latter is semiconducting.

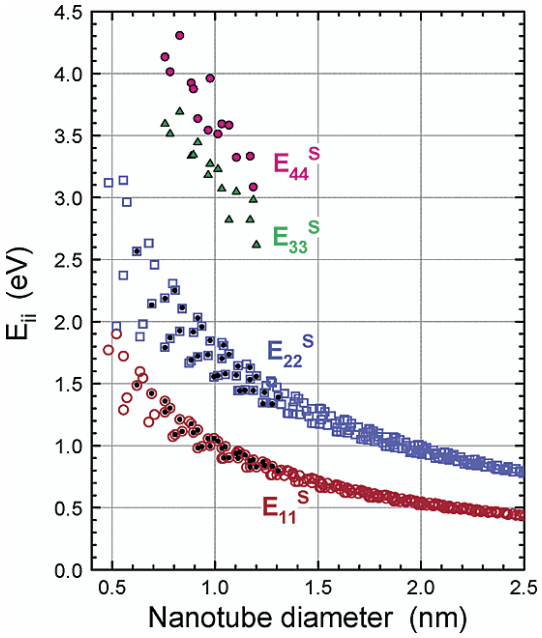

Figure 3. Kataura Plot. Where s: semiconducting. Reprinted with permission from Nano Lett. ***3,*** *1235–1238 (2003).* Copyright 2003 American Chemical Society.

The indices nanotube naming scheme shows how tubes are unique from one another in several areas. Knowing the indices allows the structure of tubes to be identified, the calculation of

nanotube diameter, and identification of electronic character as well as band gap. Each of these properties demonstrates the versatility of CNTs, meaning tubes can be selected for specific applications.

In Figure 4, the density of states are plotted for both metallic and semiconducting nanotubes. The van Hove singularities, characteristic of one-dimensional energy bands, appear at the band edges of each energy band. Metallic nanotubes show finite density of states while semiconducting tubes show an energy gap at the Fermi energy (E_F). Both metallic and semiconducting nanotubes can be attained by controlling the tube diameter.

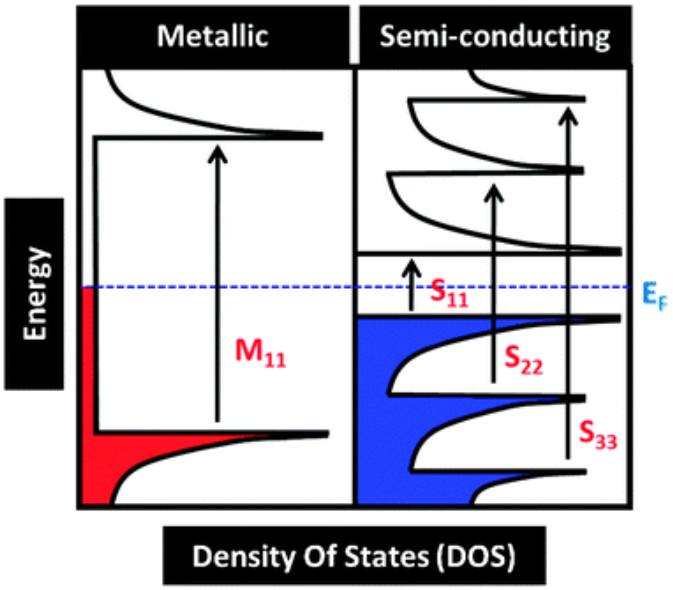

Figure 4. Plot of density of states for metallic and semiconducting CNTs. Reprinted with permission from Appl. Phys. Lett. ***60,*** *2204 (1992).* Copyright 1992 American Institute of Physics.

1.2. Functionalisation of Carbon Nanotubes

1.2.1. Covalent and Non-Covalent Functionalisation

Chemical functionalisation of CNTs offers many advantages, including improving nanotube solubility, converting them into more manageable materials and combining the unique properties of CNTs with those of other materials.[27–30] Functionalisation can be achieved *via*

covalent or non-covalent interactions. Covalent functionalisation can disrupt extended π-networks on CNT surfaces and thus can modify their mechanical and electronic properties. Electrochemical modification of individual carbon nanotubes has been demonstrated *via* attachment of substituted phenyl groups.[31–33] Two types of coupling reactions were proposed: i) Reductive coupling of aryl diazonium salts, resulting in a C-C bond formation on the graphitic surface; and ii) Oxidative coupling of aromatic amines, where aromatic molecules were directly attached to carbon nanotubes *via* amine functional groups.

As a purification method, carbon nanotubes can be oxidised *via* acid treatment, inducing openings at the tube caps and the formation of holes in the side-walls.[34,35] In 1998, Chen *et al.* treated oxidised carbon nanotubes with long chain alkylamines *via* acylation, as shown in Figure 5. This process resulted in functionalised CNTs that were soluble in organic solvents for the first time.[36]

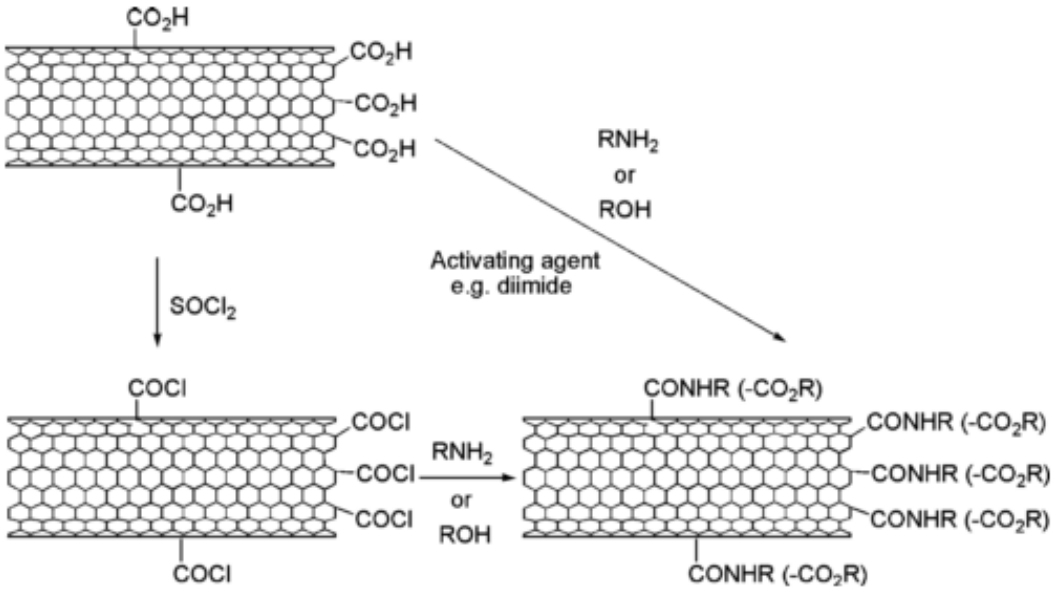

Figure 5. Derivatisation reactions of acid-treated CNTs *via* side-walls and terminal positions. Reprinted (adapted) with permission from Science. **282,** 95–98 (1998). Copyright (2017) Science.

The challenge of controlled deposition and alignment of nanotubes on different types of surfaces has been studied extensively over the last few years. Theoretically, attachment of acidic moieties to a graphitic surface can drive assembly on any substrate. Notably, controlled deposition of CNTs onto gold surfaces was achieved by the thiolation reaction of carboxyl-terminated nanotubes.[35,37,38] Short-length oxidised CNTs were treated with an appropriate thiol derivative, resulting in a chemical attachment to the gold surface.

Each example described (including Figure 5) outlines how covalent functionalisation can occur and at various positions along the tube, *i.e.* both side-wall and terminal positions. They also demonstrate the range of reactivity strategies that can be exploited: C-C bond formation, C-N bond formation and thiol-gold formation. From a synthesis perspective, one of the key purposes of this study is to control the positioning of a single C-N bond formation in the terminal position of a carbon nanotube to ensure a one-dimensional molecular junction is formed *via* a double amidation reaction.

Conversely, non-covalent interactions preserve all CNT's unique properties while being dispersed in aqueous environments. Two of the main forces that drive non-covalent interactions are van der Waals and π–stacking interactions. Utilising polymers, copolymers, biomolecules, surfactants and polyaromatic compounds, non-covalent functionalisation of CNTs has been demonstrated in literature.[39,40] For instance, in 2007, Salzmann *et al.* found dispersion effects of SWCNTs were 3.5 times higher with copolymers containing tryptophan than compared to tyrosine-containing copolymers.[40]

A range of polymers have been used in the formation of supramolecular complexes of CNTs. In particular, the formation of supramolecular complexes between DNA and CNTs has drawn attention in recent years.[41] These hybrids can take advantage of the recognition capabilities of DNA while maintaining the CNTs' unique properties. DNA-wrapped CNTs exist as well-

defined hybrids in aqueous environments due to the strong non-covalent interaction between the DNA and the CNTs.[42] Compared to other polymers used, DNA offers the advantage of defined lengths and sequences, a high dispersion efficiency (up to 4 mg/mL) and well-developed chemistries for further functionalisation – specifically at the terminal positions.

1.2.2. DNA-Wrapped CNTs

Several groups reported the synthesis of DNA-wrapped CNTs in 2003.[41,43–46] Their simple preparation consists of adding nanotubes to an aqueous solution of DNA and sonicating components in a water ice bath. Synthesis of DNA-CNTs aids nanotube dispersion, in which the wrapping effect by ss-DNA is a major driving force.[47] DNA wrapping is facilitated by the aromatic hydrophobic bases interacting with CNT sidewalls *via* π-stacking.[41] Wrapping in this orientation exposes the hydrophilic phosphate backbone to the aqueous environment and thus, DNA acts as a dispersing agent, as shown in Figure 6.[48]

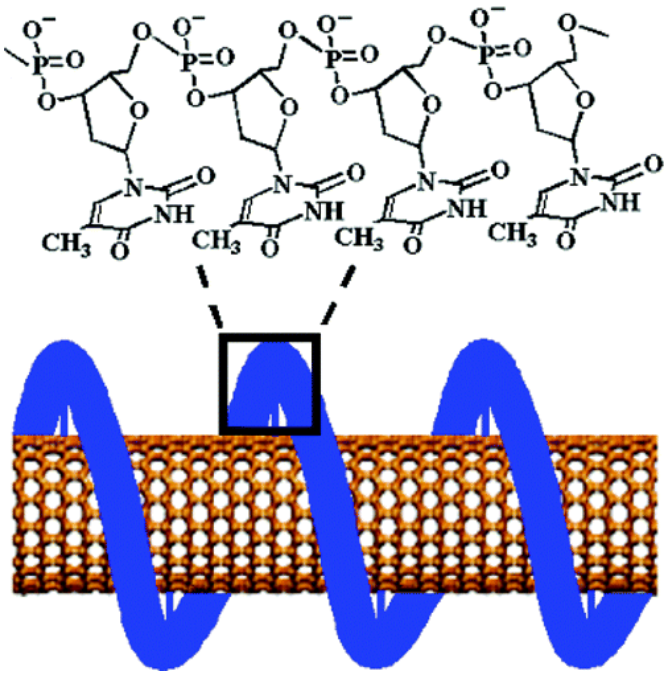

Figure 6. Schematic showing the aromatic DNA bases non-covalent binding to a SWCNT. Reprinted with permission from *J. Phys. Chem. B* ***110,*** *16359–16365 (2006).* Copyright 2006 American Chemical Society.

The nature of wrapping can differ as different DNA strands complement different CNTs from different manufacturing techniques. For example, DNA-CNT hybrids have been produced *via* denatured calf thymus DNA with SWCNTs formed by arc discharge.[44,45] Other CNT fabrication techniques include High-Pressure Carbon Monoxide conversion (HiPCO), which formed hybrids with DNA from salmon testes.[46] Short synthetic oligonucleotide sequences have also been used in the preparation of DNA-CNTs.[41,43] Other examples include short fragmented DNA, asymmetric polymerase chain reaction (PCR) synthesised DNA, and single-stranded DNA (ss-DNA) obtained *via* rolling circle amplification.[49,50,51] However, there have also been reports that certain fragments of lambda DNA and double-stranded DNA (dsDNA) formed *via* symmetric PCR lacked the capability to wrap effectively around disperse CNTs.[50,52]

1.2.3. Wrapping Procedure

Dispersions of CNTs in DNA solutions have been investigated to observe the optimum wrapping conditions. Investigations into parameters of DNA sequence and length, sonication time, CNT type and solvent conditions have been reported. Investigations showed that DNA strands with T_{60} (thymine) sequence produced the highest yield among other homopolymers to form DNA-SWCNTs.[41] Additionally, T_{30} resulted in the highest dispersion efficiency among different poly(T) DNA lengths.[41] It was also discovered that d(GT)n (where n = 10 – 45) DNA sequences have both a high dispersion yield and the highest efficiency in facilitating CNT separation *via* anion exchange chromatography.[43]

Shorter DNA sequences have displayed high dispersion yields, and a mixture of the complementary oligonucleotides $d(GT)_3$:$d(AC)_3$ showed the highest dispersion efficiency among all the sequences studied.[53] Yang *et al.* showed in 2009 that by increasing the DNA strand length, both the degree of compactness of the wrapping around the nanotube and the diameter selectivity decrease.[54]

1.2.4. DNA-Wrapped-CNT Conjugates

Studies have been conducted to investigate the synthesis of complex conjugates based on DNA-CNTs. Functionalisation of DNA-CNTs has previously been functionalised with platinum and gold nanoparticles, quantum dots, haemoprotein cytochrome c, biotin conjugated antimouse IgG as Raman biomarkers, photosensitizer, and through incorporation into polymeric film.[48,55–62]

Incorporating DNA-CNT hybrids into polymeric films was explored by Ma *et al.* where a composite was prepared between poly-(anilineboronic acid) and DNA-CNTs.[48] As shown in Figure 7, 3-aminophenylboronic acid is synthesised *via* in-situ polymerisation, of which the composite product displayed enhanced stability, conductivity and redox chemistry.[48]

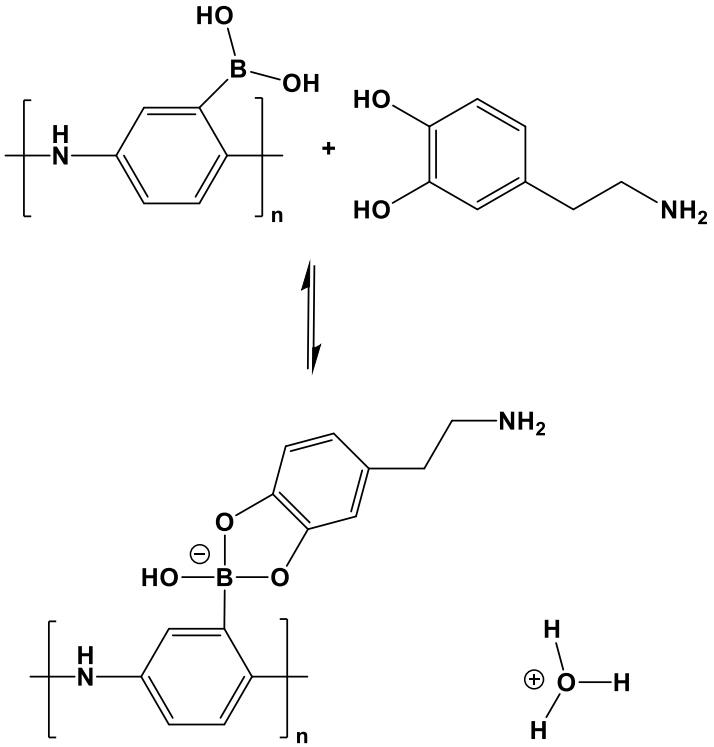

Figure 7. In situ polymerisation to synthesise 3-aminophenylboronic acid.

1.2.5. Characterisation of DNA-CNTs

There have been many techniques used to study the structure and formations of DNA-CNTs. These include: atomic force microscopy (AFM), transmission electron microscopy (TEM), Raman spectroscopy, Fourier transform infrared spectroscopy (FTIR), absorption spectroscopy, scanning electron microscopy (SEM), fluorescence spectroscopy, scanning tunnelling microscopy (STM), circular dichroism, small angle neutron scattering, optical microscopy, photoluminescence spectroscopy, energy dispersive spectroscopy (EDS), capillary electrophoresis, and electrochemistry.[44,63–76]

Structural properties of DNA-CNT hybrids have been studied using AFM, Raman spectroscopy and photoluminescence spectroscopy, which are among the most common techniques. Investigations have highlighted the use of high resolution tip-enhanced near-field microscopy to differentiate between wrapped and unwrapped CNT segments. This works by monitoring the photoluminescence energy shift along the nanotube surface.[77] Other studies found that the CNT synthetic method used dictates the DNA wrapping mechanism. Studies by AFM suggest that the DNA-wrapping mechanism for SWCNTs prepared by arc discharge may be different from HiPCO SWCNT synthesis due to variation in tube diameter.[78] Cobalt and molybdenum catalyst (CoMoCAT) synthesised SWCNTs were also studied and similar results found with respect to dependence upon tube diameter.[79]

1.2.6. Separation of Carbon Nanotubes

By utilising surfactants and dispersing agents effectively, individualisation of tubes can be achieved in solution, which leads to a sorting process with a greater control over dimension and electronic properties. Different strategies have been reported to sort CNTs by length, diameter, chirality, metallic/semiconducting character, and handedness.[42,43,80–82] In 2006, Arnold *et al.* developed a method that takes advantage of the differences in surfactant

organisation on individual suspended/encapsulated tubes.[81] Based on the density gradient ultracentrifugation (DGU) technique, this strategy is often employed in biochemistry for protein and nucleic acid purification. As part of the DGU process, ultracentrifugation causes SWCNTs to migrate in the density gradient medium until they reach their corresponding isopycnic points (where their buoyant density equals that of the surrounding medium). Therefore, objects with differing buoyant density spatially separate within the gradient.[81]

Another nanotube sorting strategy is based on ion exchange chromatography (IEX) that is commonly used to separate ions or polar molecules.[43] Separation is greatly dependent on DNA sequence, as the procedure utilises an oppositely charged resin that molecules reversibly adsorb onto. Due to the exposed phosphate backbone, the DNA-SWCNTs hybrids are negatively charged and their behaviour within in the column during the IEX process is dependent on their linear charge density.

The effective negative charge on DNA-SWCNTs is dictated by the linear charge density of the phosphate backbone along the tube axis; *i.e.* how ss-DNA is orientated along the nanotube. These properties were used to fractionalise DNA-SWCNT solutions by optical absorption, which can be identified by a nanotube's individual chiral properties. Zheng *et al.* rationalised the exploration of ss-DNA libraries and identified short DNA sequences that enabled nanotube separation by chirality.[83] They observed that the successful sequences showed periodic purine-pyrimidine patterns. It was reported that purine-pyrimidine patterns could form a two-dimensional sheet by hydrogen bonding and formed a well-ordered three-dimensional barrel, which is illustrated in Figure 8.[83]

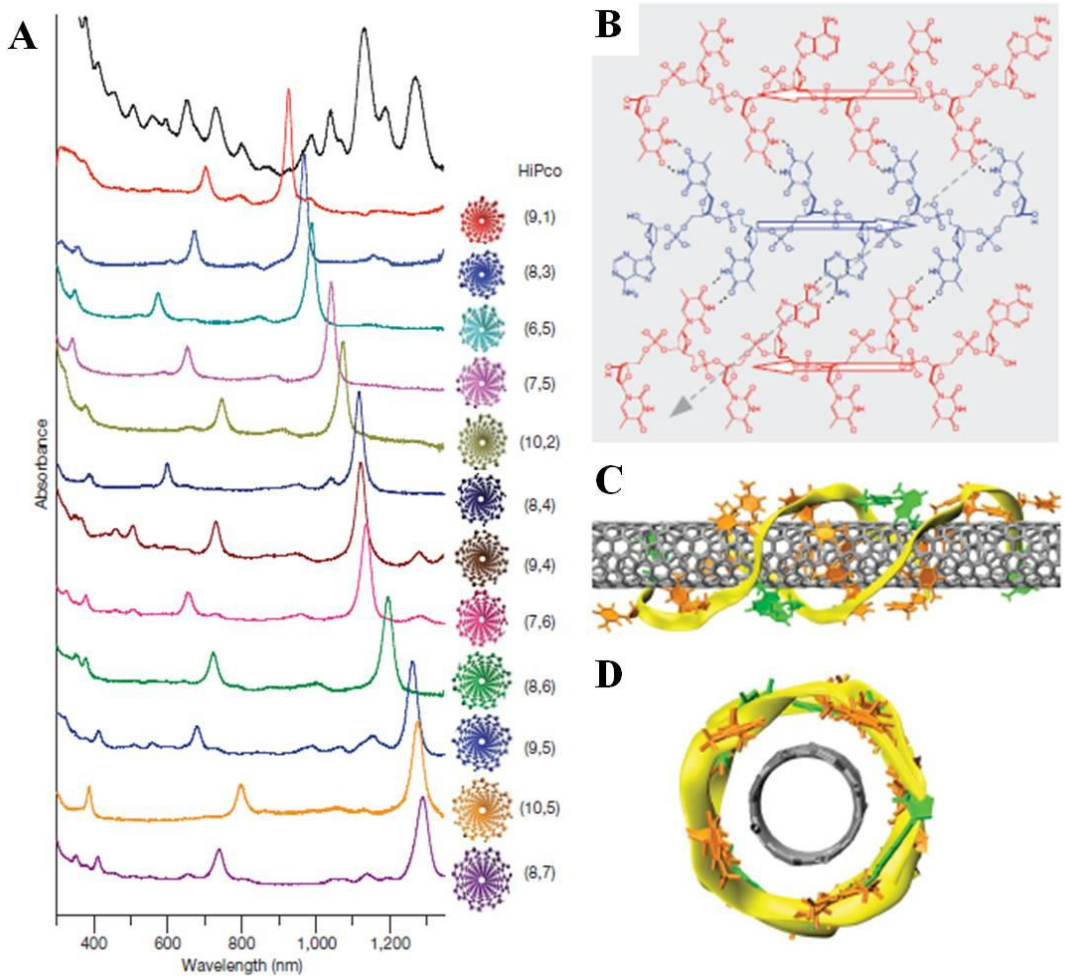

Figure 8. A) UV-Vis-NIR spectra of semiconducting SWCNTs sorted by chirality. B) Proposed organisation of a two-dimensional DNA sheet structure formed by three antiparallel $(ATT)_2$ strands. C) and D) schematic representation of the DNA barrel on a (8,4) nanotube formed by rolling up of the previous two-dimensional DNA sheets. Reprinted with permission from *Nature* ***460,*** *250–253 (2009).* Copyright 2009 Nature.

In another study, the effective separation of SWCNTs was achieved with diameters larger than 1 nm *via* multi-stage aqueous two-phase extraction (ATPE).[84] This strategy also demonstrated that refined species are readily obtained from both the metallic and semiconducting SWCNT populations. The aqueous two-phase separation experiments can be designed across a range of surfactant concentrations that separate SWCNTs of relatively small (~0.62 nm) and relatively large diameters (>1.7 nm). Furthermore, this technique also demonstrates how redox reactions can facilitate sorting of DNA-SWCNTs according to their electrical properties.[85]

1.3. Carbon Nanotubes in Single-Molecule Electronic Devices

1.3.1. Single-Molecule Electronic Devices

One of the most attractive properties of metallic CNTs is the excellent conductive properties that can be incorporated into electronic applications. The fabrication of single molecule electronic devices using CNTs as nanoscale electrodes has shown substantial promise in this field. Single-molecule electronic devices are defined as functioning electronic devices where the active component is a single molecule.[86–95]

As the dimensions of electrical devices diminish, single molecules are considered a realistic target for the miniaturisation of electrical circuits. Electronic devices, where single molecules are the active component, allow the properties of those molecules to affect the bulk properties of a material. In a typical device configuration, a single molecule is bridged between two metal electrodes, as illustrated in Figure 9.[96]

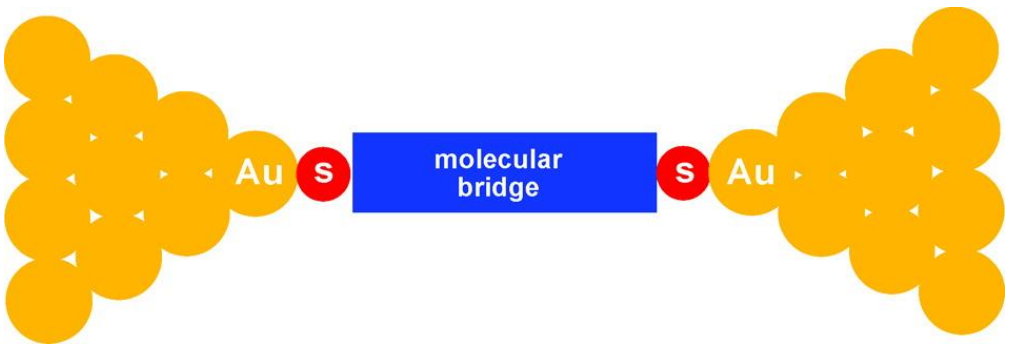

Figure 9. Schematic of single-molecule electronic device. Molecular bridge between gold electrodes *via* thiol contacts. *Reprinted with permission from* Acc. Chem. Res. ***41,*** *1731–1741 (2008). Copyright 2008 American Chemical Society.*

The technological trend, known as Moore's law, has allowed the performance and complexity of integrated circuits to grow exponentially, while the size of components have shrunk accordingly. As those features shrink, device fabrication strategies become increasingly demanding and expensive. The alternative is to build up individual atoms/molecules to form

components, which is known as a ‘bottom-up’ technique, rather than to carve them out of bulk materials, known as a ‘top-down’ technique. Bottom-up strategies permit circuits to be built in a chemistry laboratory, allowing billions of copies to be synthesised simultaneously. This approach facilitates particular molecules that resemble traditional electronic components, such as wires, transistors or rectifiers.[97,98] The continuous demand for higher computing power, in conjunction with the limitations of top down lithographic techniques, means the arrival of single-molecule electronics is necessary to continue satisfying Moore’s law. A key step in the overall synthesis is to discover reliable and reproducible methods that establish contacts between the electrically active components and electrodes.

Miniaturisation of electrical devices down to individual molecules means that quantum effects should be considered.[99] Typical electronic components function because electrons can be filled in or drawn out in a continuous flow of charge – however in single-molecule devices, a single electron alters the system significantly. When transferred from source electrode to electrically active molecule, there must be sufficient energy levels available for electron transfer, otherwise there is a disruption in the continuous flow of charge.

1.3.2. Organic Components in Single-Molecule Electronic Devices

Organic electronic materials have impacted the development of semiconducting, photovoltaic, and thermoelectric devices.[59,100,101] Organic synthesis accommodates precise molecular control, allowing properties in devices to be adapted sufficiently. For instance, hole/electron-transporting (*i.e.* p- and n-type) semiconductors can be designed and synthesised, which has led to significant advancements in organic electronics.[102–104] To improve electron transport, other strategies have been explored, including the incorporation of electronegative functional groups onto conjugated molecules to increase electron affinity.[105–107]

Generally, there are two main experimental test beds that are most commonly utilised to study single molecule electronic devices: 1. Break junctions and 2. Scanning probe microscopy techniques.

Break junctions are fabricated *via* the formation of nanometre-sized gap electrodes and consist of two types: mechanically controllable break junctions (MCBJs) and electromigrated break junctions (EBJs).

MCBJs were first illustrated in 1997.[86] In this study, a self-assembled monolayer (SAM) of 1,4-benzenedithiol (BDT) was formed on a gold wire. Two gold electrodes could bind *via* thiol functional groups, allowing the gold wires to be subsequently elongated in the molecular solution until breakage. Once broken, the wires were brought together until the onset of a conductance value.

In 1999, Park *et al.* first developed EBJs.[108] Fabrication is achieved by a controlled passing of a large electrical current through a gold nanowire predefined by electron-beam lithography. The current flow causes the electromigration of gold atoms and eventually the breakage of the nanowire. The process results in two stable metallic electrodes separated by 1-2nm gap with high efficiency, ideally suited for electron-transport studies of chemically synthesised nanostructures.

Differently to break junctions, scanning probe microscopy techniques are utilised in single-molecule electrical devices investigations. Scanning tunnelling microscopy (STM) and conductive atomic force microscopy (C-AFM) have been widely used to measure the charge transport properties of a single molecule (and up to several tens of molecules). STM combines high-resolution imaging and spatially resolved electrical spectroscopy (so-called scanning tunnelling spectroscopy, STS) that provides local density of states with atomic spatial resolution.[109–111] Electrical contact is established between the molecule or molecular

monolayer and the STM tip through the air gap or vacuum tunnelling gap in ultra-high vacuum STM. Determining whether there is contact between a single molecule or monolayer means it is difficult to evaluate the true conductance of a single molecule. Therefore, STM measurements can often lead to a wide range of conductance values. The technique employed in this study shows a 4% variation in conductance results. Furthermore, DFT calculations on molecular junctions display a single molecule junction is more thermodynamically favourable than a system with multiple molecules. Both factors illustrate that the technique employed provides a reliable contact of a single molecule.

C-AFM utilises a metal-coated tip that acts a mobile electrode and is gently brought into direct contact with the molecules on a conducting substrate, which acts as the counter electrode.[112–114] This process is monitored by the feedback loop a part of the AFM apparatus and an external circuit is used to measure the current-voltage (*I-V*) characteristics. This characterisation technique is utilised and further discussed in the studies presented in chapter 3.

1.3.3. Carbon Nanotubes in Single-Molecule Electronic Devices

One technique by Guo *et al.* described the incorporation of an electrically active single molecule bridging two SWCNTs in a one-dimensional configuration (*i.e.* end-to-end).[96,115] This was accomplished by establishing a nano-sized gap into a nanotube by precise oxidative cutting through a lithographic mask. Using electron-beam (e-beam) lithography, a window was created in poly(methyl methacrylate) (PMMA) forming the lithographic mask. Oxidative cutting induces the formation of terminal carboxylic acid functional groups that are utilised in a double amidation reaction with a single conjugated diamine molecule, as shown in Figure 10.[115] Bridged nanotubes *via* covalent bonding can withstand and respond to large environmental changes based on the molecule's functional groups.[96,116] For instance, molecular bridges made up of oligoanilines produce a device in which the conductance is sensitive to pH,

due to protonation on nitrogens.[102] Furthermore, using diarylethenes as molecular bridges formed devices that can switch reversibly between conjugated and non-conjugated states.[115]

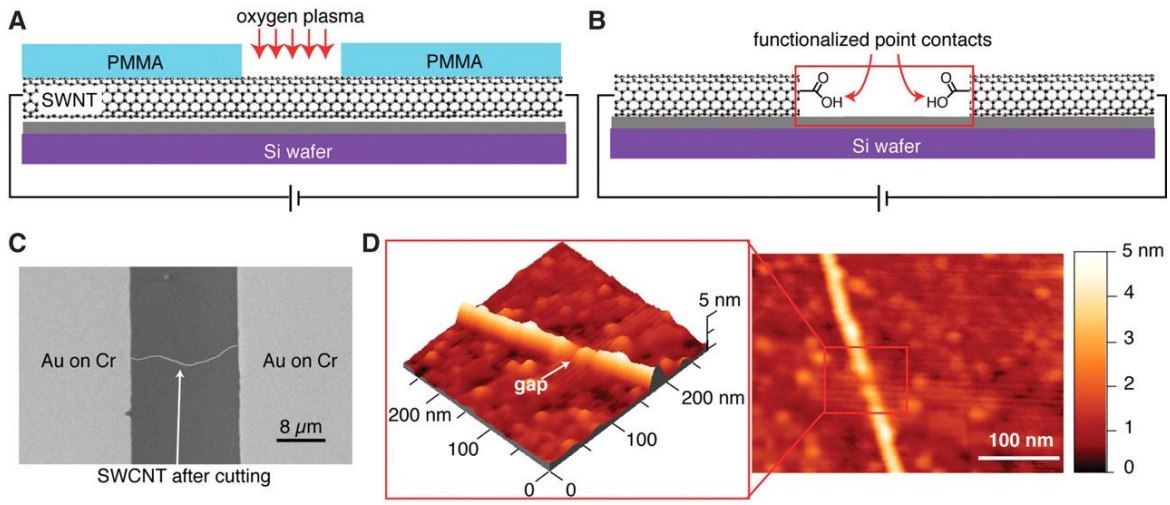

Figure 10. (A) Oxygen plasma of SWCNTs introduced through an opening in a window of PMMA defined with e-beam lithography. (B) Oxidative opening of a tube produces two point-contacts functionalised with carboxylic acids in the terminal positions. (C) Scanning electron micrograph of a SWCNT with gold on chromium leads that had been cut using e-beam lithography and an oxygen plasma. (D) AFM image of the gap cut into the nanotube. (Inset) Height profile of the isolated tubes. Reprinted with permission from *Science* (80). **311,** 356–359 (2006). Copyright 2006 Science.

Biologically active molecules, including DNA (ss and ds), have also been shown to bridge terminal SWCNTs *via* a similar procedure.[117,118] This approach has shown great potential in a growing area of single-molecule electronics; however, the methodology has limitations. Top-down strategies to create PMMA windows involve an expensive, time-consuming and low yielding (typically ~5%) electron-beam lithographic process, meaning that device fabrication is not generally accessible. In recent times, further development on this methodology has expanded to graphene electrodes to form stable molecular conduction junctions.[119] Despite improving the yield of junction formation to 20%, the procedure still endures a time consuming and expensive top-down lithography strategy.[119]

Improving upon this method, a bottom-up strategy to form SWCNT molecular junctions in solution has been investigated by Palma *et al.*[120] Utilising DNA-SWCNTs, terminal carboxylic defects facilitate an amidation reaction with a range of non-conjugated diamine linkers in an aqueous environment. This approach can produce multiple molecular junctions as shown in Figure 11.

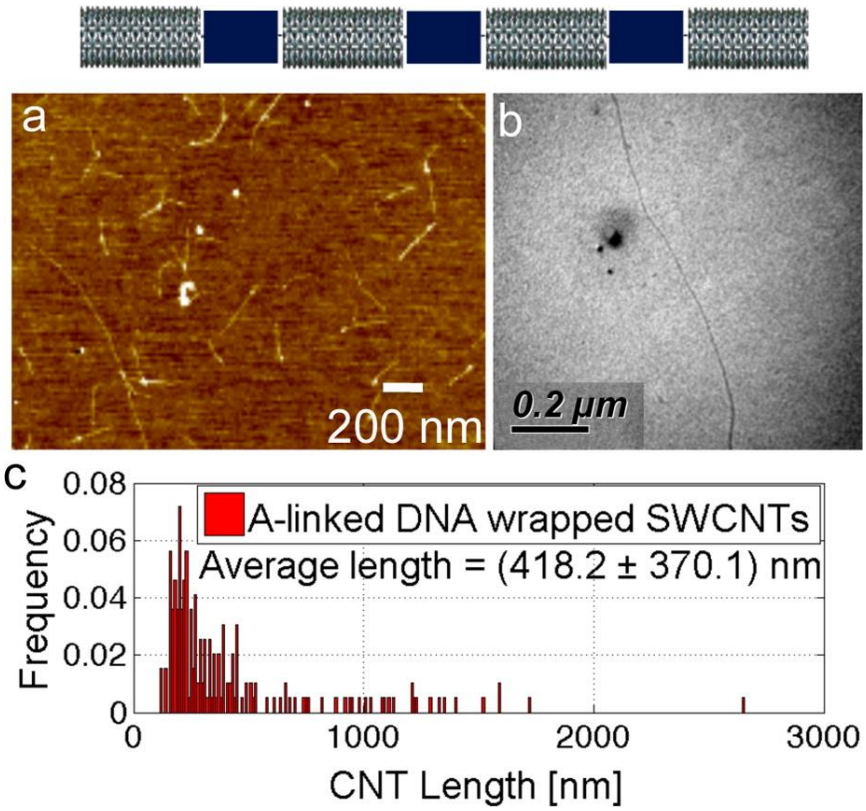

Figure 11. (top) Schematic of linear one-dimensional SWCNT junctions. (a) AFM topographical image and (b) TEM image of SWCNT junctions formed using molecular linker hexamethylenediamine (HMD). (c) Normalised histogram showing the length distribution of the observed linear junctions. The average length of 418.2 ± 370.1 nm was determined from ca. 200 nanotube junctions. Reprinted with permission from *J. Am. Chem. Soc.* **135**, *8440−8443*, (2013). Copyright 2013 American Chemical Society.

1.3.4. Bottom-Up Strategies

Alternative strategies can also overcome the limitations of e-beam lithography. One approach focuses on colloidal metallic nanoparticles as building blocks for fabricating nanogaps, which are subsequently bridged to electrodes (fabricated lithographically).[121,122] A combination of

bottom-up and top-down methods have also been exploited in fabricating gold nanorods as potential nanoelectrodes.[123–125]

1.4. Concluding Remarks

The properties of CNTs have shown great potential in several key areas – the aim of this research is to exploit the properties of CNTs *via* the formation of molecular junctions. Using a bottom-up technique, molecular junctions can be synthesised by bridging CNTs that are appropriate to form one-dimensional (1D) and two-dimensional (2D) structures. Forming 1D CNT-based structures will open possibilities for novel single-molecule devices for the next generation of electronics. The work described in this study will illustrate the key milestones required of achieving a CNT-based single-molecule device in the future.

One of the key milestones for my research was performed by Zheng and co-workers in 2003. Their work outlined how CNTs can be sorted by size and electronic properties, which has facilitated my research into forming molecular junctions. By sorting tubes by length and chirality, 1D CNT structures could be analysed that have specific dimensions and properties. For example, the formation of molecular junctions was characterised *via* the measurements of nanotube lengths. Therefore, there is a fundamental necessity for CNTs to be sorted into uniform lengths prior to junction formation. For SWCNTs to act as nanoelectrodes, they must exhibit metallic character and therefore, there is a need to sort nanotubes per their electrical properties.

By utilising the sorting process, the unique properties of CNTs and conjugate formation techniques, this study will build upon the work done by Palma *et al.* in 2013.[120] Fabricating molecular junctions with conjugated diamine molecular linkers will enable the electrical properties of single molecules to be investigated using a solution-based, bottom-up procedure that is inexpensive, relatively fast, facile and environmentally friendly. Furthermore, different

molecular junctions have been fabricated to establish device configurations and 2D (side-by-side) structures.

1.5. Aims

The overall ambition described in this thesis is in three main parts. The first ambition of this work is to investigate how metallic CNTs act as nanoelectrodes in a novel molecular junction assembly and how conductive measurements of individual molecules are performed. Once established, the next objective is to develop a novel synthetic pathway of a tri-amine molecular linker, as well as the formation of three-terminal junctions based on the previously developed junction fabrication methodology. This will provide a foundation to a CNT-based single-molecule electronic device. Lastly, this work will target the development of molecular junctions in a 2D superstructure, which can allow for the development of electrical devices into networks. This work will also attempt to find an application to utilise the versatility of carbon nanotubes.

2.0 Materials and Methods

2.1.0 Microscopy Techniques

2.1.1 Atomic Force Microscopy (AFM) Characterisation Technique

Atomic force microscopy (AFM) was developed in 1986 by Binning and co-workers to image samples with low electrical conductivity.[126,127] AFM maps out surfaces and interfaces at a resolution that ranges from hundreds of micrometres to nanometres.[127] The versatile technique can provide information regarding the structural and dynamic properties of thin films. The AFM microscope used, as part of the Matteo Palma Research Group, was provided by Bruker and is shown in Figure 12.

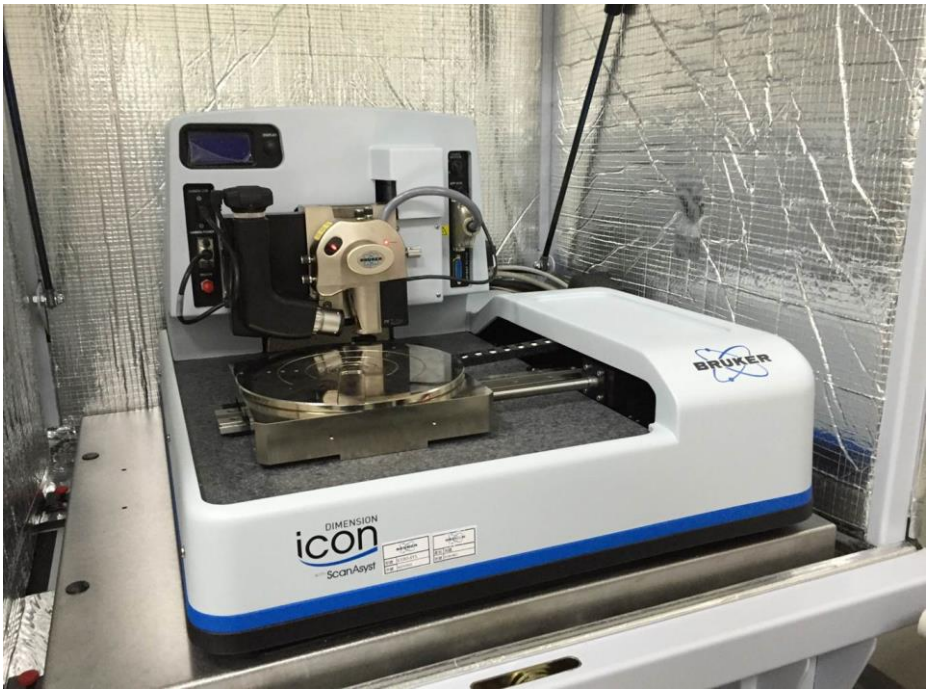

Figure 12. Dimension Icon ScanAsyst atomic force microscope from Bruker used by the Matteo Palma Research Group.

Utilising a sharp tip with a terminal radius typically ~10 nm (~100 Å), AFM probes the surface of a sample. Tips are positioned at the end of a cantilever, which is ~100 µm long and has an elastic modulus that can reach tenths of N/m. Forces between the tip and sample surface cause

deflections of the cantilever – these forces are typically in the range of pico-Newtons. Monitoring of the tip is performed by a laser that rebounds off the back of the cantilever onto a position-sensitive photo detector. As deflections occur, the laser beam will change position on the detector – this facilitates the mapping of surface topography on the micrometre and nanometre scale.

Forces that contribute to the deflection of a cantilever can be initially estimated as Van der Waals and repulsive forces, e.g. inter-atomic repulsion forces. These initial approximations are described in the Lennard – Jones potential:

$$V = 4\varepsilon\left[\left(\frac{\sigma}{r}\right)^{12} - \left(\frac{\sigma}{r}\right)^{6}\right]$$

Where:

V = intermolecular potential between two molecules or atoms, (kJ/mol)

ε = depth of potential well (kJ/mol)

r = inter-atomic distance (separation between particles, Å)

σ = the distance in which the intermolecular potential between two particles is zero (Å)

$1/r^{12}$ = dominated at short distance, models repulsion forces (Å)

$1/r^{6}$ = dominated at large distance, constitutes attraction forces (Å)

In Figure 13, forces between the tip and sample in the dependence of distance are plotted. The two highlighted areas refer to two important distance regimes: 1) the contact regime; and 2) the non-contact regime. Within the contact regime, the tip is less than a few hundred picometres from the sample surface – the interatomic force between the cantilever and sample is repulsive. Within in the non-contact regime, the tip is at a distance range of tens to hundreds of angstroms from the surface – the interatomic force between the cantilever and sample is an attractive force, which is largely because of long-range van der Waals interactions.

Figure 13 also highlights Tapping Mode, whereby the vibrating cantilever is brought closer to the sample so that the tip comes into brief contact with (or "taps") the sample.[128] This mode utilises both repulsive and attractive forces to map the surface topography and is a typical technique in obtaining AFM images in this research. Under tapping mode, the cantilever will oscillate at near its resonant frequency, in which the tip contacts the surface on each oscillation. To overcome the stickiness of a surface, the oscillation amplitude of the cantilever facilitates a wide range of vertical positions, typically ranging from 20 to 100 nm.[128] An oscillation amplitude of this scale is much larger than ranges found in non-contact mode. Intermittent contact with the surface leads to perturbation on the oscillation amplitude, which the feedback system is designed to detect. As the tip scans laterally across a surface, the height variation may be adjusted with the feedback system to maintain a constant setpoint value. The combination of a setpoint established by a modified oscillation amplitude and the feedback system, generates topographical images. Tapping mode relies on the change in oscillation amplitude *via* tapping the surface and not a shift in frequency, as seen in non-contact mode.[128]

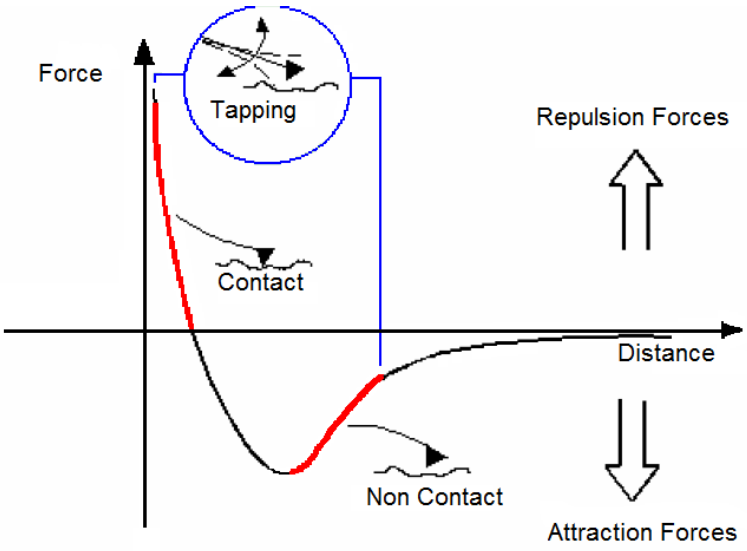

Figure 13. Lennard - Jones potential force curve.

2.1.2 AFM for Electronic Properties of Samples

Several AFM based techniques have been developed that exploit electrically conducting probes.[129] The prime physical properties they measure are current flows, resistance, capacitance, electrostatic forces, charge distribution, surface potential or voltage drops on sub-100 nm lengths. One of these techniques that is fundamental to this research is conductive probe atomic force microscopy (C-AFM).

C-AFM is utilised *via* a tip with a conductive coating, which is used as mobile electrode in a typical AFM setup. Once a position of interest has been identified, the tip meets the sample surface (*i.e.* enters contact mode) under a specified force that is maintained by a feedback system. A voltage is applied between tip and a fixed counter electrode, which generates current vs voltage (*I*-*V*) characteristics at fixed points on the sample surface. Measured currents can range from pico-amperes to hundreds of nano-amperes, depending upon the system under study. To measure the resistance of the tip-sample junction, the inverse slope of the *I*-*V* trace is used. Ohm's law dictates that at small voltages *I*-*V* behaviour is conventionally linear, this facilitates the inverse of the slope to measured.

Both AFM techniques will provide the foundation in characterising all CNT structures and molecular junctions. To establish a methodology to fabricate molecular junctions with a high yield, low cost and high efficiency, a bottom-up strategy must be performed. Establishing a strategy that forms molecular junctions in solution means utilising an appropriate surfactant to disperse SWCNTs.

2.1.3 Transmission Electron Microscopy (TEM) Characterisation Technique

First demonstrated by Max Knoll and Ernst Ruska, transmission electron microscopy (TEM) was invented in 1931. Following its invention, the technique displayed a resolution greater than

that of light in 1933 by the same group who produced the first commercial TEM in 1939. Ruska eventually won the Nobel Prize in physics by 1986 for the development of TEM.[130]

TEM is a microscopy technique in which a beam of electrons is transmitted through a sample, resulting in an image.[131] Typically, the specimen is an ultrathin section less than 100 nm thick or a suspension on a customised grid. An image is formed from the interaction of the electrons with the sample as the beam transmits through. The image is then magnified and focused onto an imaging device, such as fluorescent screen, a layer of photographic film, or a sensor such as a charge-coupled device.[130]

Transmission electron microscopes are capable of imaging at a significantly higher resolution than light microscopes, owing to the smaller de Broglie wavelength of electrons compared to the wavelength of photons. This results in finer details being captured, thousands of times smaller than a resolvable object seen in a light microscope.[130,131] TEM is a major analytical method across a range of fields including nanotechnology.[132] TEM will provide key contributions to chapter 5, where relatively large 2-dimensional nanotube-based structures are formed on the macroscopic scale. The TEM microscope used was a JEOL 2010: high resolution TEM instrument operating at 200kV, lattice image resolution to 0.15nm, provided by NanoVision and is shown in Figure 14.

Figure 14. TEM microscope JEOL 2010: high resolution TEM operating at 200kV, lattice image resolution to 0.15nm, provided by NanoVision.

2.2. Experimental Procedures

2.2.1 Experimental Procedure of DNA Wrapping and SWCNT Chirality Separation

DNA-wrapped Single-walled Carbon Nanotubes (SWCNTs) were dispersed in DI water at a concentration of *ca.* 1 mg/mL. In a typical dispersion experiment, 1 mg of CoMoCAT SWCNT powders (SG65 grade, lot no. SG65EX-002, Southwest Nanotechnologies) were suspended in 1 mL aqueous DNA (Integrated DNA Technologies) solution (1 mg/mL $(TCG)_4TC$, 0.1 M NaCl). The mixture was sonicated (Sonics, VCX130) in an ice-water bath for 2 hours at a power level of 8 W. After sonication, the samples were divided into 0.1 mL aliquots, and centrifuged (Heraeus Fresco 17) for 90 min at 17,000 g to remove insoluble material, leaving

DNA-dispersed carbon nanotube solutions at a mass concentration around 0.5 mg/mL. DNA-wrapped SWCNTs were separated into single chirality (7,4) to obtain a solution of tubes with metallic properties only via a polymer aqueous two-phase separation method.[133]

Single chiral DNA-wrapped SWCNTs (DNA-SWCNTs) were then cast onto hydrophobic silicon dioxide (SiO_2) surfaces. Prior to casting, surfaces must be treated to form a hydrophobic layer. All experiments required casting onto clean, flat surfaces to ensure physisorption. All experiments were performed on 500-550 μm thick silicon wafers (Silicon Quest International) covered on both sides with 295nm of thermal SiO_2, cut into $1cm^2$ sections with a diamond tip scriber. Once cut, all SiO_2 substrates were exposed to piranha solution for 5 minutes before being washed with ultra-pure H_2O and ethanol (VWR), and dried under nitrogen flow. Piranha solution is a strong oxidising agent and was made up of sulfuric acid (H_2SO_4, VWR) and hydrogen peroxide (H_2O_2, Sigma Aldrich) in a 3:1 ratio respectively.

Once cleaned, surfaces were treated with Sigmacote® (Sigma Aldrich) self-assembled monolayer (SAM) solution via overnight incubation. Sigmacote® SAM solution consisted of: toluene (200 mL, VWR), acetic acid (3 mL, Sigma Aldrich) and Sigmacote® (10 mL). Once overnight incubation was complete, surfaces were washed with acetone (VWR), ethanol and ultra-pure H_2O and dried under nitrogen flow.

Adopting drop cast techniques, solutions were cast onto Sigmacote® treated SiO_2 surfaces and electrode patterned substrates, and allowed to dry in air. Once fully dry, the samples were washed with ethanol and ultra-pure H_2O followed by blow drying with nitrogen. Surfaces were then placed into an *N*-methyl-2-pyrrolidone (NMP, Sigma Aldrich) bath overnight. Surfaces were once again washed with ethanol and ultra-pure H_2O and dried under nitrogen flow.

Utilising AFM, samples were imaged under ambient conditions with a Bruker Dimension Icon microscope, with a NanoScope IV control unit and PF-TUNA add-on module. Tapping mode

AFM imaging was performed with TESPA tips (Bruker, spring constant 40 N/m). Images were analysed with NanoScope Analysis (version 1.5, Bruker) software.

AFM images of DNA-SWCNTs were then analysed: length distributions where calculated with NanoScope Analysis software (Bruker) and histograms where generated by Matlab version 2015 a. Both straight and non-straight Nanotube structures were measured using the measuring tool on NanoScope Software: non-straight structures were measured multiple times at various points along the tube to ensure accuracy.

2.2.2 Experimental Procedure of Amidation Reaction

Molecular junctions were formed via an amidation reaction between terminal DNA-wrapped SWCNT carboxylic defects and amine-terminated molecular linkers. Amide bond formation in aqueous conditions was performed with coupling reagents 1-ethyl-3-[3-dimethylaminopropyl]carbodiimide hydrochloride (EDC, 4 mM, Sigma Aldrich) and *N*-hydroxysulfosuccinimide sodium salt (sulfo-NHS, 10 mM, Sigma Aldrich) in an MES buffer (pH 4.7, 0.2 M, ThermoScientific). Pristine DNA-wrapped SWCNTs in DI H_2O were added to the activating solution in a 1:1 equivalence and left to incubate for 30 minutes. The solution was then diluted with BupH Phosphate Buffer Saline (pH 7.2, TPBS, ThermoScientific) solution in a 1:1 volume ratio and left incubating for 1 hour. Molecular junctions were synthesised with metallic DNA-SWCNTs (*i.e.* nanotubes with (7,4) chirality only) and a mixture of semiconducting/metallic DNA-SWCNTs (a range of chiral vectors).

Each molecular linker was solubilised in an ethyl acetate (VWR) solution (1 µL at 0.1 mM concentration) before being diluted in 1mL of ultra-pure H_2O (100 nM, 18 MΩ, Millipore). The molecular linker solution (10 nM) was then added to the SWCNT solution and left incubating overnight. A separate solution of activated DNA-wrapped SWCNTs was subsequently added to the reaction mixture in a 1:1 ratio, to increase linker coupling and was

left incubating overnight. The mixture was then cast (20 µL) onto Sigmacote® (Sigma Aldrich) treated silicon dioxide surfaces and characterized by AFM. DNA-wrapped SWCNT segments and junction lengths were measured analysing the AFM images. Lengths were recorded and plotted onto a histogram with average and standard deviation values calculated. Bin sizes in histograms were set at 100 nm intervals to observe the spread of results and to give a clear indication of junction formation.

2.2.3 Fabrication of Macroscopic Metal Electrodes

Micrometre-scale electrodes on SiO_2 substrates were made of Chromium/Gold bi-layer (1 nm Cr/ 20 nm Au) or Chromium/Palladium bilayer (1 nm Cr/ 10 nm Pd) by physical vapour deposition and lift-off procedures. Image reversal photolithography formed a negative pattern of the mask by applying a photoresist (AZ 5214E, Microchem Gmbh) that was first introduced to pattern the substrates to guarantee a sharp edge. AZ 726 MIF was used as a developer to remove the photoresist. After metal deposition, the lift-off procedure was performed in NMP at 70 °C for 2 hours to remove the sacrificial stencil layer (photoresist). Samples were then rinsed with acetone, isopropanol and dried under nitrogen flow. Cr/Au electrodes were additionally flame annealed to flatten electrode surfaces.

2.2.4 Conductive-AFM Measurements

DNA-wrapped SWCNT junctions were interfaced to macroscopic gold or palladium electrodes fabricated as described previously. I-V curves were recorded along the MTJs. C-AFM tips (coated with Platinum/Iridium) were used as the mobile counter electrode to contact the SWCNTs (PeakForce-TUNA tips, Bruker) as shown in Figure 18.[134] Sites along the tube junctions were selected with gaps of 15 nm to 25 nm during the I-V recordings. The voltage bias was ramped between -500 mV to 500 mV. The data was then analysed by NanoScope Analysis (version 1.5, Bruker) and Matlab (version 2015 a).

2.2.5 4-Chlorobenzene-1,3-diamine with NaN_3

4-Chlorobenzene-1,3-diamine (0.028 mol, 1.82 g) and sodium azide (7.01 mmol, 1.00 g) were added to a sealed round bottom flask and purged under nitrogen. Anhydrous DMF (20 ml) was added and reaction was heated to 100°C and allowed to stir for 24 hours.

Reaction mixture was diluted with DI H_2O and extracted with diethyl ether. Organic phase was dried with $MgSO_4$ and solvent evaporated under reduced pressure to give grey product.

2.2.6 CuAAC: 2-azidobenzene-1,4-diamine with $CuSO_4.5H_2O$

2-azidobenzene-1,4-diamine (0.402 mmol, 59.90 mg), $CuSO_4.5H_2O$ (0.03 mmol, 7.5 mg), sodium ascorbate ($9.99x10^{-3}$ mmol, 1.98 mg), propagylamine (0.402 mmol, 22.13 mg) were all added to and sealed within a round bottom flask. H_2O/*t*-BuOH (20 ml) was added to dissolve all reagents. Reaction mixture was stirred at room temperature for 24 hours.

Thin layer chromatography (TLC) was used to observe the progress of the reaction. TLC revealed starting material remained after 24 hours.

2.2.7 Boc Protection: 2-chlorobenzene-1,4-diamine

2-chlorobenzene-1,4-diamine ($5.26x10^{-3}$ mol, 0.75 g) was dissolved in THF (10 ml) and purged under nitrogen at 0°C. Triethylamine (0.021 mol, 2.93 ml) was added to reaction mixture over a period of 5 minutes. Di-tert-butyl dicarbonate (0.012 mol, 2.52 g) was dissolved in THF and added to the reaction mixture over a period of 30 minutes, followed by stirring at 0°C for 1 hour. Reaction mixture was stirred for 18 hours at room temperature.

Crude product was washed with citric acid and saturated brine sequentially followed by extraction by diethyl ether. Organic phase was dried under $MgSO_4$ and solvent removed under reduced pressure to give white solid which was purified with flash column chromatography to give white crystal product.

2.2.8 Sonogashira Cross-Coupling: Boc-2-chlorobenzene-1,4-diamine and Boc-propagylamine

$Pd_2(dba)_3$ ($4.37x10^{-3}$ mmol, 4.01 mg), potassium carbonate (0.219 mmol, 30.24 mg), XPhos ($4.37x10^{-3}$ mmol, 3.70 mg) were all added to a round bottom flask and purged with argon. Solids were dissolved in anhydrous DMF (20 ml) and then bubbled with argon for 3 minutes. Separately, Boc-2-chlorobenzene-1,4-diamine (0.146 mmol, 50.0 mg) and Boc-propagylamine (0.219 mmol, 33.99 mg) were dissolved in anhydrous DMF and bubbled with argon in a round bottom flask. Alkyne/chloro solution was added to Pd catalyst solution with stirring at 110°C for 24 hours. Reaction was monitored by TLC until all Boc-2-chlorobenzene-1,4-diamine was consumed.

Reaction mixture was washed with DI H_2O and extracted with diethyl ether. Organic phase dried under $MgSO_4$ and solvent removed under reduced pressure to produce brown solid. Crude product was purified under flash column chromatography to produce light-brown solid.

2.2.9 Boc Deprotection: di-tert-butyl (2-(3-((tert-butoxycarbonyl)amino)prop-1-yn-1-yl)-1,4-phenylene)dicarbamate with Ethyl Acetate/Hydrochloric Acid

di-tert-butyl (2-(3-((tert-butoxycarbonyl)amino)prop-1-yn-1-yl)-1,4-phenylene)dicarbamate (0.029 mmol, 13.4 mg) was added to a round bottom flask. Separately, a solution of hydrochloric acid (HCl, 3 M) in ethyl acetate (EtOAc, 1 ml) was made. HCl/EtOAc (200 µl) was added to starting material and stirred for 1 hour. Solvent was removed under reduced pressure to give red-brown solid.

2.2.10 Molecular Junction Formation – Tri-Amine and Porphyrin Ring Linkers

Amide bond formation in aqueous conditions was performed with coupling reagents 1-ethyl-3-[3-dimethylaminopropyl]carbodiimide hydrochloride (EDC, 4 mM) and N-

hydroxysulfosuccinimide sodium salt (sulfo-NHS, 10 mM) in an MES buffer (pH 4.7, 0.2 M). Pristine DNA-wrapped SWCNTs in DI H_2O were added to the activating solution in a 1:1 equivalence and left to incubate for 30 minutes. The solution was then diluted with BupH Phosphate Buffer Saline (pH 7.2, TPBS) solution in a 1:1 volume ratio and left incubating for 1 hour. Molecular junctions were synthesised with metallic DNA-SWCNTs (*i.e.* nanotubes with (7,4) chirality only).

Tri-amine molecular linker was solubilised in methanol solution (1 µL at 0.1 mM) before being diluted in 1mL of ultra-pure H_2O (100 nM, 18 MΩ). Porphyrin Ring linkers were solubilised in ethyl acetate solution (1µL at 0.1 mM) before being diluted in 1mL of ultra-pure H_2O (100 nM, 18 MΩ). The molecular linker solution (10 nM) was then added to the SWCNT solution and left incubating overnight. A separate solution of activated DNA-wrapped SWCNTs was subsequently added to the reaction mixture in a 1:1 ratio, to increase linker coupling and was left incubating overnight. The mixture was then cast (20 µL) onto Sigmacote® treated silicon dioxide surfaces and characterised by AFM. DNA-wrapped SWCNT segments and junction lengths were measured analysing the AFM images. Lengths were recorded and plotted onto a histogram with average and standard deviation values calculated. Y-shape and X-shape configurations were counted and yield calculated.

2.2.11 Three-terminal Junction Identification

Step 1. Y-Shape Structure Identified.

Step 2. All three nanotube structures measured using Nanoscope Analysis measuring tool.

Step 3. Junction point estimated – i.e. where do all three nanotube terminations meet?

Three-terminal junctions confirmed if: a) all three nanotubes are within tolerance of pristine CNT length. b) Angle of all tubes are different to one another.

2.2.12 ss-DNA Wrapping SWCNT/MWCNT Procedure

1 mg of Elicarb SWCNT powders (Thomas Swan) was suspended in aqueous NaCl (0.1 M) with 1 mL of aqueous DNA (Integrated DNA Technologies) to form a 1 mg/mL solution. The mixture was sonicated (Sonics, VCX130) in an ice-water bath for 2 hours at a power level of 8 W. After sonication, the samples were divided into 0.1 mL aliquots and centrifuged (Heraeus Fresco 17) for 90 min at 17,000 g to remove insoluble material, leaving DNA-dispersed carbon nanotube solutions at a mass concentration around 0.5 mg/mL. DNA-SWCNT solutions (15 µL) were cast onto SiO_2 hydrophilic surfaces and cleaned *via* H_2O and ethanol (Sigma Aldrich, 96%) baths followed by drying under nitrogen flow. Samples were then characterised *via* AFM and statistical analyses performed with NanoScope Analysis 1.5.

2.2.13 SWCNT Assemblies Formation Procedure with Alkyne-DNA-SWCNT/MWCNT

Four ss-DNA sequences were used, where U is uracil with alkyne functionality: $(GT)_{20}$-U; $(GT)_8U(GT)_4GUT(GT)_7$ Parallel Alkyne ;$(GT)_8U(GT)_2U(GT)_2GUT(GT)_7$ Zig-zag Alkyne. Azide linker used: 1,12-diazidododecane

25 µL of alkyne-DNA-SWCNTs/MWCNTs (0.5 mg/mL) was added to 25 µL of azide linker (0.2%) and incubated for 30 minutes at room temperature. Aqueous $Cu(OAc)_2$/$CuSO_4$ (Sigma Aldrich, 0.4 M, 50 µL) solution was added to the reaction mixture and incubated for 24 hours at room temperature. The resulting mixture was diluted 1:8 with H_2O before cast onto SiO_2 hydrophilic surfaces and cleaned *via* H_2O and ethanol (Sigma Aldrich, 96%) baths followed by

drying under nitrogen flow. Samples were characterised *via* AFM and statistical analyses performed with NanoScope Analysis 1.5.

2.2.14 2D SWCNT Assemblies Formation Procedure with Azide-DNA-SWCNT

ss-DNA sequence where U is uracil with azide functionality: $(GT)_{20}$-U. Alkyne linkers used: 1,8-octadiyne and tripropargylamine.

25 µL of azide-DNA-SWCNTs (0.5 mg/mL) was added to alkyne linker (25 µL, 0.2%) and incubated for 30 minutes at room temperature. Aqueous $Cu(OAc)_2/CuSO_4$ (Sigma Aldrich, 0.4 M, 50 µL) and incubated for 24 hours at room temperature. The resulting mixture was diluted 1:8 with H_2O before cast onto SiO_2 hydrophilic surface and cleaned *via* H_2O and ethanol (Sigma Aldrich, 96%) baths followed by drying under nitrogen flow. Samples were characterised *via* AFM and statistical analyses performed with NanoScope Analysis 1.5.

2.2.15 2D Nanotube Structure Formation Procedure with Azide-DNA-SWCNT and Alkyne-DNA-SWCNT

ss-DNA sequence where U is uracil with azide functionality: $(GT)_{20}$-U. ss-DNA sequence where U is uracil with alkyne functionality: $(GT)_{20}$-U.

25 µL of azide-DNA-SWCNTs (0.5 mg/mL) was added to 25 µL of acetylene-DNA-SWCNTs (0.5 mg/mL) and incubated for 30 minutes at room temperature. Aqueous $Cu(OAc)_2/CuSO_4$ (Sigma Aldrich, 0.4 M, 50 µL) was incubated for 24 hours at room temperature. The resulting mixture was diluted 1:8 with H_2O before cast onto SiO_2 hydrophilic surface and cleaned *via* H_2O and ethanol (Sigma Aldrich, 96%) baths followed by drying under nitrogen flow. Samples were characterised *via* AFM and statistical analyses performed with NanoScope Analysis 1.5.

2.2.16 SWCNT-network formation with Azide-DNA-SWCNT and Alkyne-DNA-SWCNT

ss-DNA sequence where U is uracil with azide functionality: $(GT)_{20}$-U.

ss-DNA sequence where U is uracil with alkyne functionality: $(GT)_{20}$-U.

30 µL of azide-DNA-SWCNTs (0.5 mg/mL) was added to 45 µL of alkyne-DNA-SWCNTs (0.5 mg/mL) and incubated for 30 minutes at room temperature. Aqueous sodium ascorbate solution (1 M, 30 µL) was added followed by aqueous $Cu(OAc)_2$/$CuSO_4$ (Sigma Aldrich, 0.4 M, 3 µL) was incubated for 24 hours at room temperature. The resulting mixture was diluted 1:8 with H_2O before cast onto TEM grids and washed *via* H_2O and dried in a desiccator overnight. Samples were then imaged *via* TEM and statistical analysis performed.

2.2.17 Polymer Film Formation with Nanotube Structure and Young's Modulus Measurement

Aqueous polyvinyl alcohol solution (4%, 10 mL) was prepared. Nanotube structures (20 µL) were dispersed into PVA solutions (180 µL) and cast into 8-well plates and allowed to dry overnight. Films were removed and characterised *via* AFM. Force-distance curves obtained *via* AFM experimental software Peakforce QNM in Air using ScanAsyst AFM tip. Young's Modulus values measured *via* NanoScope Analysis software.

3.0 Solution-Processable Carbon Nanoelectrodes for Single Molecule Investigations

3.1 Introduction and Aims

Electrical devices in integrated circuits have been decreasing in size exponentially for decades in a technological trend known as Moore's Law.[135] Moore, in 1965, stated the following:

"The complexity for minimum component costs has increased at a rate of roughly a factor of two per year... Certainly over the short term this rate can be expected to continue, if not to increase. Over the longer term, the rate of increase is a bit more uncertain, although there is no reason to believe it will not remain nearly constant for at least 10 years. That means by 1975, the number of components per integrated circuit for minimum cost will be 65,000. I believe that such a large circuit can be built on a single wafer"

As a result, top-down fabrication techniques for silicon-based devices are becoming limited, as quantum mechanics and thermodynamic restrictions are encountered by electrical devices with dimensions lower than 100 nm.[136] In an attempt to continue miniaturisation, one alternative strategy is to develop optoelectronic devices based on organic single-molecules.[137,138] Organic molecules offer nanometre dimensions, a wide-range of functionalities and high-level control through chemical synthesis.[139]

Single-molecule electronic devices are those where the electrically active component is a single molecule. In a typical single-molecule device, gold electrodes are bridged by a dithiol molecule in a metal-molecule-metal configuration, which has received substantial attention in recent years, as shown in Figure 8 (page 30).[96,140–146] Utilising the metal-molecule-metal orientation, a range of strategies have been developed to form molecular transport junctions (MTJs), including scanning probe techniques, lithographic approaches, and mechanical/electromigration break junctions.[139,147–150]

In chapter 1, section 1.3.2, different strategies were discussed in investigating the electrical properties of single molecules, including break junctions and scanning probe microscopy techniques. Top-down fabrication methods have provided substantial progress from a fundamental and technological standpoint. However, there are notable limitations, primarily the fabrication time and cost as well as the difficulty in ensuring only a single molecule bridges electrodes.[151] Also, due to electromigration, the device is not stable at room temperature and has ultimately led to the stark contrast in experimental and theoretical results.[89] Our approach looks to ensure junctions are formed with a single molecule only *via* a bottom-up self-assembly strategy in an aqueous solution without the need for expensive lithographic processes. Our approach also drives junction formation at room temperature and will be able to withstand the temperatures experienced during an annealing step. Furthermore, our approach builds molecular junctions without the need of an AFM tip as part of the electrically active device. This is an important implication for next generation devices, as it offers greater versatility without the need for expensive and impractical equipment.

An improved strategy would ensure a single well-defined contact is made between the molecule and electrode due to a limited number of binding sites. The use of carbon-based nanoelectrodes, in particular, has emerged as a promising approach.[96,115,145,152–155] SWCNTs display desirable qualities to fulfil this requirement and have the potential to form molecular junctions where they act as metallic electrodes due to their intrinsic nanoscale size and a reduced electronic mismatch with organic molecules.[96,115,145,152–156]

Guo *et al.* explored the incorporation of an electrically active molecule between two SWCNTs in an end-to-end assembly.[115] Precise oxidative cutting through a lithographic mask facilitated the formation of a nano-sized gap into a nanotube, ultimately leading to 1-dimensional assemblies. Expanding upon this methodology with electron-beam lithography, graphene has also been utilised as nanoelectrodes.[119] The field of carbon-based nanoelectrodes has been

discussed in chapter 1, section 1.3.3 and will be discussed later in this chapter. This chapter will discuss the investigation of molecular junction formation between metallic SWCNTs and conjugated diamine single molecules. The aim of this section of the project is to establish a methodology to form molecular junctions and then to investigate the conductive properties of single molecules *via* conductive atomic force microscopy (C-AFM).

3.2. SWCNT Wrapping of Single-Stranded DNA

In chapter 1, the work of Guo *et al.* was outlined as a top-down fabrication process to immobilise a single conjugated diamine between two SWCNTs via a nanogap.[96] This procedure proved to be challenging as e-beam lithography does not allow to precisely control the size of the nanogaps, leading to very low yield of subsequent junction formation (less than 5%). Gap sizes were difficult to control due to varied electron wavelengths creating windows in PMMA masks of different sizes, which ultimately led to gap sizes with differing lengths (<10 nm). The lithographic process was also expensive and time-consuming. To improve upon these limitations and ultimately the yield of junction formation, Palma *et al.* in 2013 developed a self-assembly process with DNA-wrapped SWCNTs to form molecular junctions in an aqueous solution *via* a bottom-up strategy.[120] Nevertheless, this work only demonstrated junction (formation in solution) of unconjugated molecules, and did not prove the potential of these junctions to act as molecular transport junctions, *i.e.* with the SWCNTs acting as nanoelectrodes.

The advantages of wrapping ss-DNA around SWCNTs, as outlined in chapter 1, include, most notably: a) the DNA acts as a dispersing agent, allowing insoluble SWCNTs to be dispersed in aqueous conditions, b) DNA protects the side-walls of the nanotube, meaning only terminal

carboxylic defects are available for subsequent functionalisation, and c) specific DNA sequences can separate SWCNTs with electronic properties.[43]

In collaboration with Dr. Ming Zheng (National Institute of Standards and Technology, NIST) SWCNTs were wrapped with DNA and separated per length *via* size-exclusion chromatography and chirality (thus electronic properties), *via* polymer aqueous two-phase separation method.[157,158] To image DNA-SWCNTs, we cast low-coverage films on silicon wafer substrates and characterised them *via* AFM to monitor both self-assembly and the degree of junction formation.

3.2.1. Pristine Semiconducting/Metallic Mix, and pristine single-chirality metallic DNA-SWCNTs Length Analysis

Figure 15 displays an AFM image and the measurements of the starting material of this study. Analysed *via* AFM, the starting material of pristine semiconducting/metallic mixture DNA-SWCNTs exhibit an average length of 429.7 ± 177 nm – this value will be the benchmark in all future 1-D molecular junction formation experiments from semiconducting/metallic mixture nanotubes. The average length and standard deviation is calculated from ca. 100 nanotube structures and measurements are performed on Nanoscope Analysis software. This statistical analysis method was conducted with all AFM images.

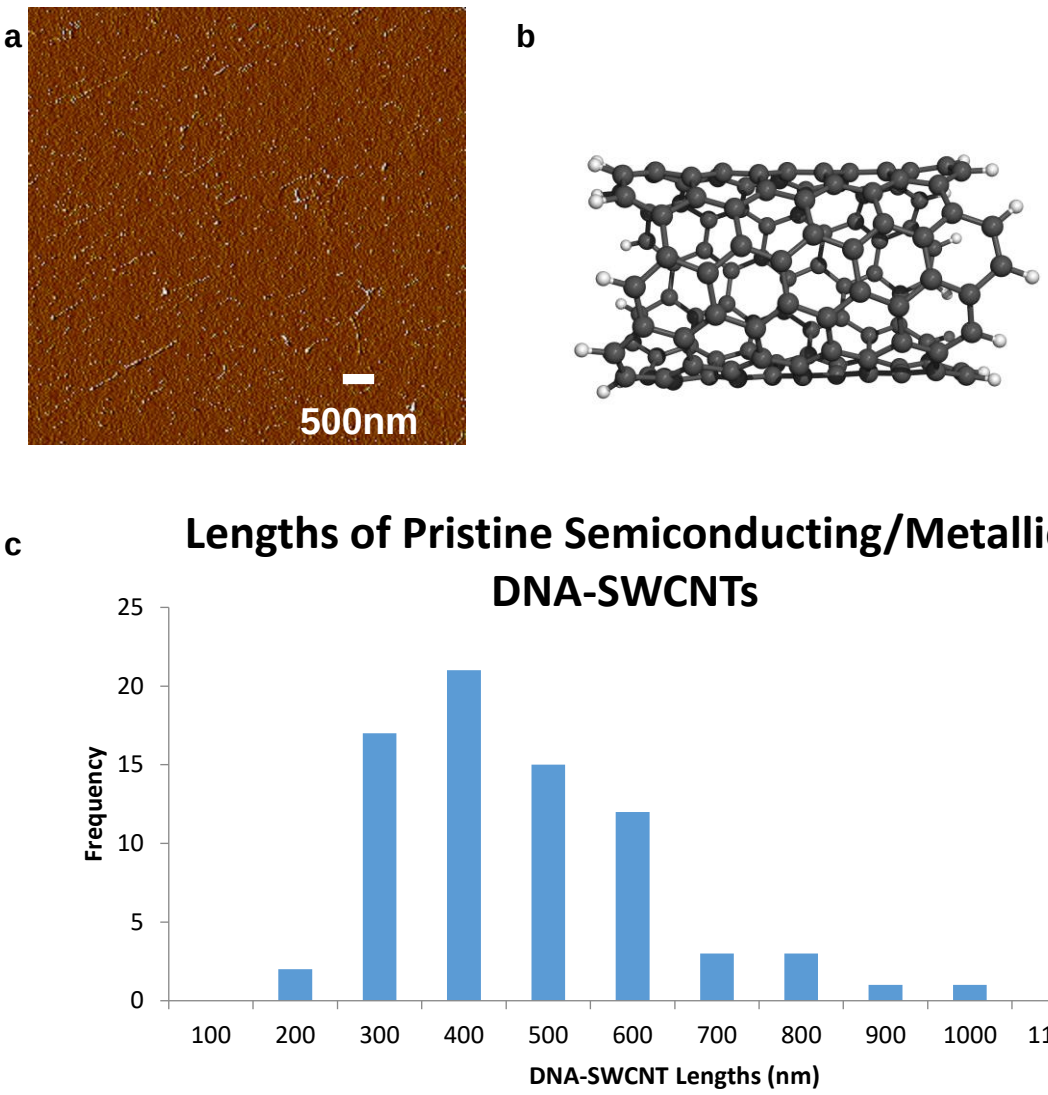

Figure 15. a) AFM topographical image displaying pristine semiconducting/metallic mix DNA-wrapped SWCNTs. b) Schematic of pristine semiconducting/metallic mix DNA-wrapped SWCNT. c) Histogram of pristine semiconducting/metallic mix DNA-wrapped SWCNTs measured. Average tube length: 429 ± 177 nm.

Figure 16 displays a characteristic AFM image and the measurements of the length of the other starting material of our study, namely pristine metallic (7,4) DNA-SWCNTs. Analysed *via* AFM, the starting material of pristine metallic (7,4) DNA-SWCNTs exhibit an average length of 473.7 ± 179.5 nm – this value will be the benchmark in all future 1-D molecular junction formation experiments from metallic nanotubes. Frequency is defined as the number of nanotube structures counted and measured.

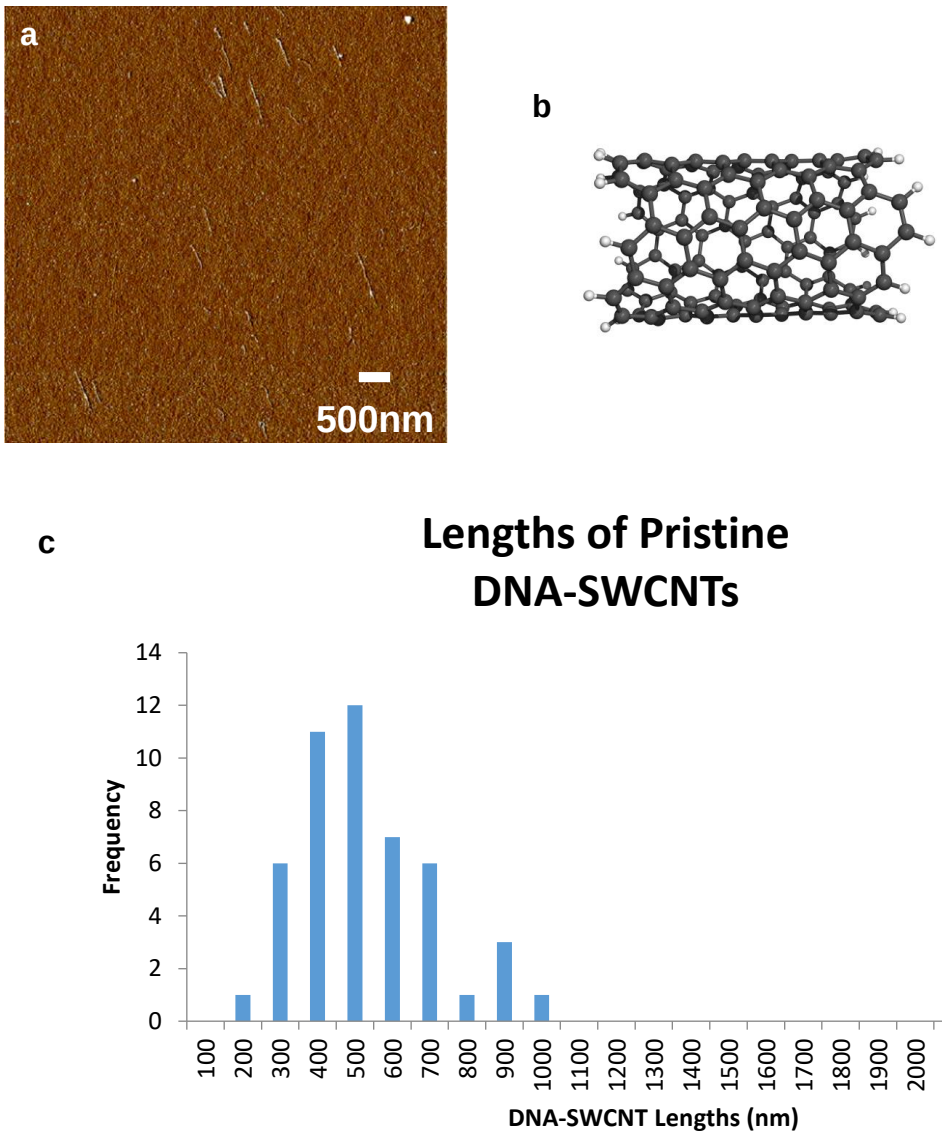

Figure 16. a) AFM topographical image displaying metallic pristine DNA-wrapped SWCNTs. b) Schematic of pristine DNA-wrapped SWCNT. c) Histogram of metallic DNA-wrapped SWCNTs measured. Average tube length: 473.7 ± 179.5 nm.

SWCNTs display carboxylic acid groups, generated by ·H atoms and ·OH radicals formed *via* sonication to form H_2, H_2O_2 and water or attack solute molecules.[159] Carboxylic acid groups are formed following oxidation of these functional groups. The presence of carboxylic terminations have been further supported by the immobilisation of activated nanotubes on amine-functionalised nanopatterns.[120] Double amidation reactions with diamine linkers facilitates the bridging of SWCNTs in 1-D configurations, as shown in Figure 17, *via* carboxylic terminations. Previous studies have shown non-conjugated linkers bridge activated nanotubes.[120] For this study, we employed conjugated diamines to ensure molecular junction formation that can facilitate charge transport through a single molecule. Conjugated diamines require organic solvents for their solubilisation, so these solvents will be utilised in molecular junction formation. Furthermore, it should be noted that amide bonds possess a partial double bond character, ensuring a reliable contact between the molecule and the carbon nanoelectrode. Previous studies as far back as 2006 demonstrate conductance measurements through conjugated molecules covalently linked *via* amide bonds between CNT electrodes.[115,116,160]

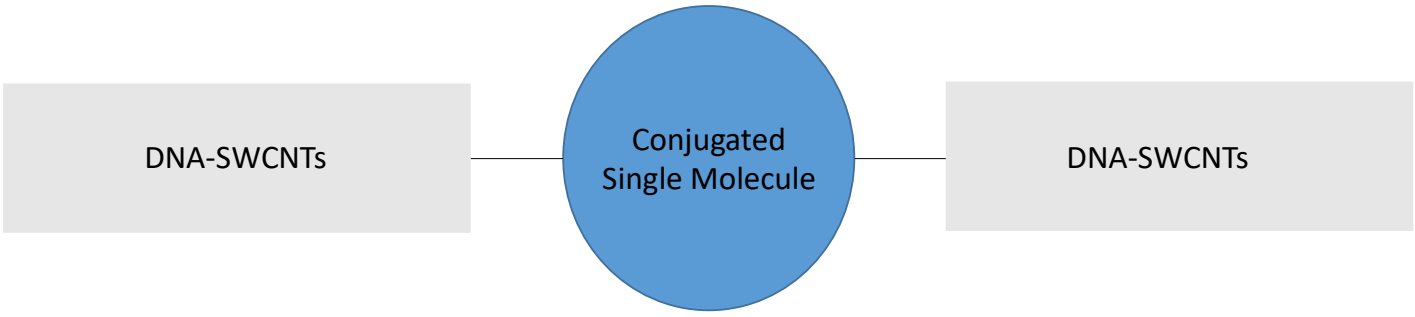

Figure 17. Schematic of the overall molecular junction in a one-dimensional configuration.

3.3. Solubility of Diamine Conjugated Linkers

One of the goals of this study was to establish a methodology to form molecular junctions in solution. Molecular linkers must, therefore, be soluble to bridge terminal SWCNTs. Solubility tests on each molecule were necessary to investigate which solvents would be appropriate for

junction formation. Organic solvents were validated by observing if the resulting solution was uniform and fully solubilised following a vortex with each molecular linker.

3.3.1. Conjugated Diamine Molecular Linkers

Figure 18 displays each selected molecular linker to bridge SWCNTs *via* double amidation reactions with terminal carboxylic defects. Note, all linkers are diamines and a series of oligophenyls, to verify how the molecular conductance varies with phenyl rings (molecular length) as an intrinsic control experiment.

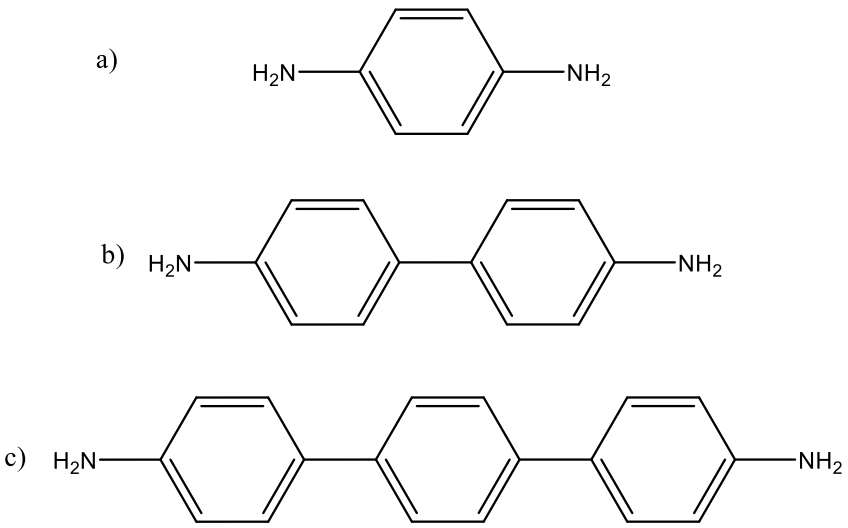

Figure 18. Conjugated diamine structures: a) p-Phenylenediamine (PPD) b) benzidine c) 4,4”-diamino-p-terphenyl (Terphenyl).

1 mg of each diamine was added to 500 µL of solvent and observations were noted in Table 1. Results suggest that polar aprotic solvents possess the appropriate properties to separate the diamine oligophenyls by interfering with pi-pi stacking forces between molecules.

Table 1. Solubility results of conjugated diamines with organic solvents and water.

Solvent	PPD	Benzidine	Terphenyl
Dichloromethane (DCM)	Soluble	Soluble	Soluble
Tetrahydrofuran (THF)	Soluble	Insoluble	Soluble
Ethyl acetate (EtOAc)	Soluble	Soluble	Soluble
Acetone	Soluble	Soluble	Soluble
Dimethylformamide (DMF)	Soluble	Insoluble	Soluble
Acetonitrile (MeCN)	Soluble	Insoluble	Soluble
Dimethyl sulfoxide (DMSO)	Soluble	Insoluble	Soluble
Water (H_2O)	Insoluble	Insoluble	Insoluble

Surprisingly, Benzidine is insoluble in THF, DMF, MeCN and DMSO, while PPD and Terphenyl show sufficient solubilisation. This is unexpected as Benzidine has a similar molecular structure to PPD and Terphenyl. However, it could be suggested that doubling the number of phenyl rings will increase the difficulty in overcoming pi-pi stacking. Therefore, it is reasonable to suggest that a more polar solvent is required to solubilise Benzidine compared to PPD. The molecular structure of Terphenyl indicates an increase in bond rotation (due to the

presence of a third phenyl ring) compared to Benzidine. Subsequently, greater bond rotation will reduce the number of pi-pi interactions for the solvent to overcome.

Table 1 shows dichloromethane (DCM), ethyl acetate and acetone as appropriate solvents for all molecular linkers. We also wanted to observe the behaviour of SWCNTs in these solvents. Therefore, DCM, ethyl acetate and acetone were all added to DNA-SWCNT solutions in a 1:1 ratio respectively and cast onto hydrophobic silicon surfaces (please see section 2.2 Experimental Procedures for details on hydrophobic surface formation). AFM images were taken of each sample and were analysed.

In DCM, nanotubes appear to aggregate, as shown in Figure 19. AFM images also show large aggregations of impurities throughout the surface. It could be suggested that DCM could be altering the structure of wrapped DNA *via* intercalation and causing mild stripping of nanotubes.

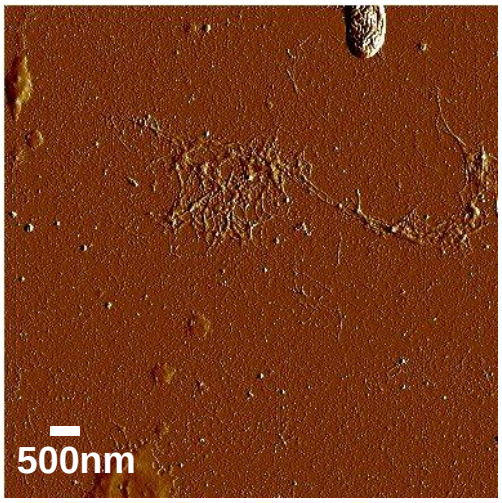

Figure 19. AFM image of DNA-SWCNTs in DCM solvent.

Conversely, as shown in Figure 20, DNA-SWCNTs with ethyl acetate show good dispersion of tubes with very few instances of impurities or aggregations.

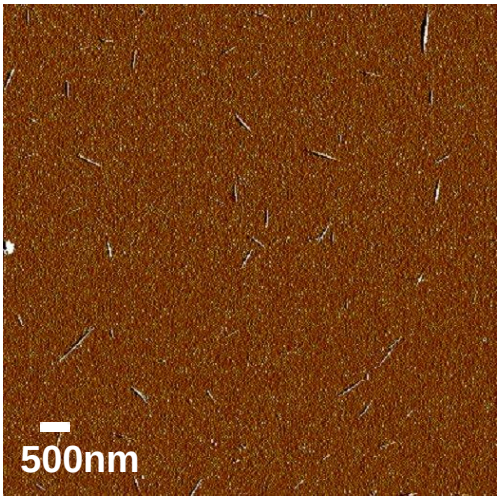

Figure 20. AFM image of DNA-SWCNTs in Ethyl Acetate solvent.

Figure 21 shows that DNA-SWCNTs with acetone show good tube dispersion with very few instances of impurities or aggregation.

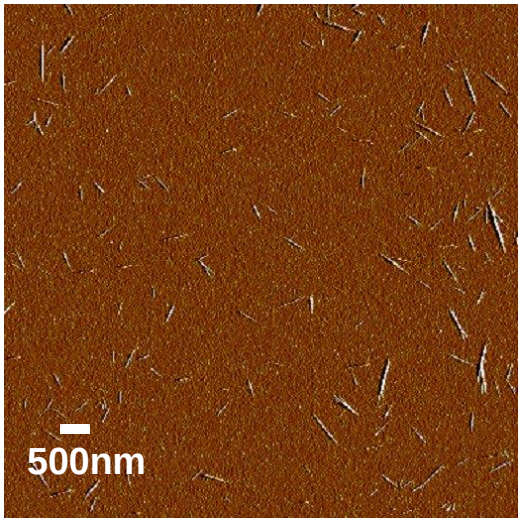

Figure 21. AFM image of DNA-SWCNTs in Acetone solvent.

From the results shown, ethyl acetate and acetone were found to be ideal solvents to potentially be employed in the solubilisation of molecular linkers as they both displayed appropriate solubility of all molecular linkers and did not interfere with nanotubes or form aggregates with impurities.

3.4. Molecular Junction Formation

To fabricate molecular junctions, a carbodiimide and NHS strategy was undertaken as reported in published procedures.[120] As an initial proof of principle, Matteo Palma *et al.* demonstrated molecular junction formation using this strategy in aqueous conditions with aliphatic (non-conjugated) molecular linkers. An EDC/NHS strategy is typically used in protein synthesis and is a simple methodology that results in a high yielding amide bond formation, with a high degree of control *via* buffer solutions. Exploiting the SWCNT terminal carboxylic functional groups, nanotubes are susceptible to nucleophilic attack from amino groups, as shown in Figure 22. Conjugated diamines would then bridge terminal DNA-SWCNTs to form molecular junctions *via* a double amidation reaction.

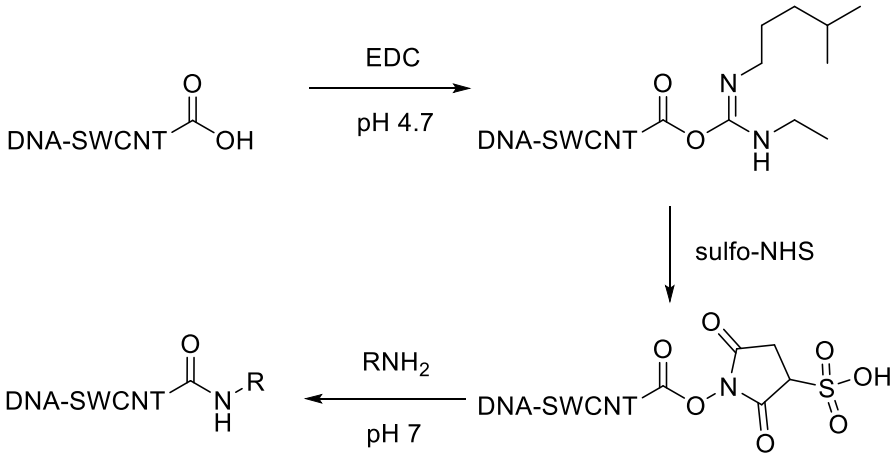

Figure 22. Synthetic pathway of an amidation reaction to form molecular junctions.

Molecular junctions were formed (as explained in section 2.2) and the solutions were cast onto silicon surfaces with hydrophobic coating (see experimental procedures, section 2.2) and imaged *via* AFM. AFM images were all analysed by measuring the lengths of each DNA-SWCNT and SWCNT-based junctions. Pristine semiconducting/metallic mix DNA-wrapped SWCNTs had an average tube length of 429 ± 177 nm (see Figure 15), and molecular junction formation would be confirmed if the lengths of tubes were over 750 nm. Pristine metallic DNA-

SWCNTs had an average length of 473.7 ± 179.5 nm (see Figure 16), and similarly, molecular junction formation would be confirmed if the length of tubes were over 750 nm. The molecular linkers employed as molecular junctions are as follows: *p*-phenylediamine (PPD), benzidine, 4,4”-diamino-p-terphenyl (terphenyl), diaminofluorene (DAF), 4,4'-(ethyne-1,2-diyl)dianiline (dianiline), hexamethylenediamine (HMMD) and 4-toluenesulfonyl chloride.

3.4.1. *p*-Phenylenediamine (PPD) Molecular Linker with Semiconducting/Metallic Mixture DNA-SWCNTs

As previously described, double amidation reaction with semiconducting/metallic mixture DNA-SWCNTs and PPD linker was performed to form molecular junctions as shown in Figure 23. Solutions of molecular junctions were cast onto hydrophobic silicon surfaces and imaged *via* AFM. Analysing AFM images and performing a statistical analysis, it was found that a significant increase in average nanotube length (mean: 890 ± 593 nm, max: 3200 nm) and standard deviation from the control measurement (429.7 ± 177 nm) indicating molecular junction formation.

Statistical analyses of molecular junctions reveal the linker characteristics of PPD. Contrasting the average nanotube length measured with the control nanotube length, there is a clear demonstration of predominantly single junctions forming. However, from the maximum nanotube length measured, it can also be deduced that multiple junctions have been formed by sequential linkages of DNA-SWCNTs with PPD.

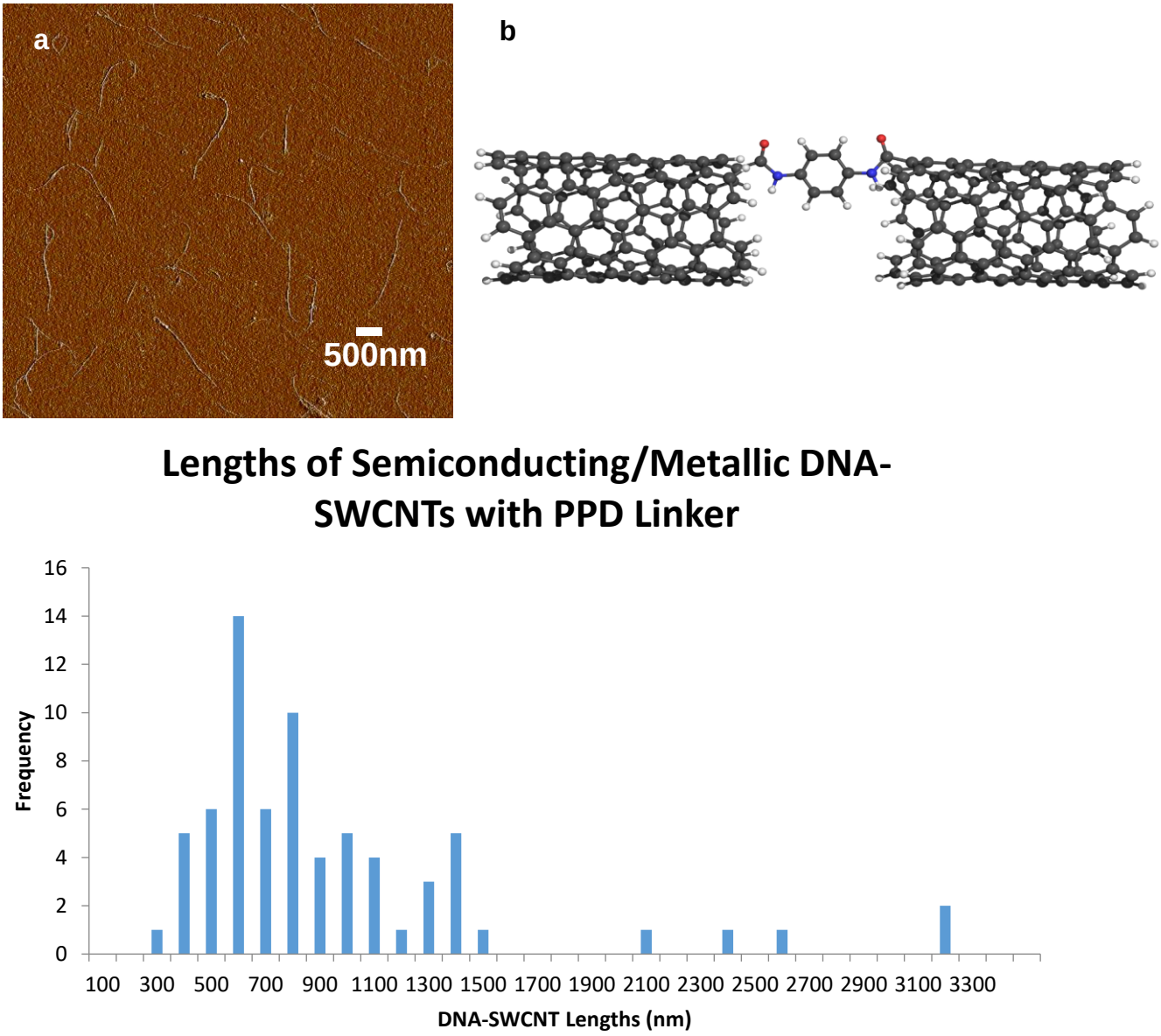

Figure 23. a) AFM topographical image displaying pristine semiconducting/metallic mix DNA-wrapped SWCNTs. b) Schematic of pristine DNA-wrapped SWCNT. c) Histogram of pristine semiconducting/metallic mix DNA-wrapped SWCNTs measured. Average tube length: 890 ± 593 nm.

It is worth noting that it is difficult to attain quantised lengths considering the relatively broad distribution of measurements of the pristine nanotubes. Indeed, these tubes were not sorted by length following junction formation.

3.4.2. *p*-Phenylenediamine (PPD) Molecular Linker with Metallic DNA-SWCNTs

To perform electrical measurements at the single-molecule level, we need to employ metallic nanotubes. Therefore, as similarly discussed in section 3.2, we employed a double amidation reaction with metallic DNA-SWCNTs and PPD linkers in order to form molecular junctions, as shown in Figure 24. Solutions of molecular junctions were cast onto hydrophobic silicon surfaces and imaged *via* AFM. Analysing AFM images and performing a statistical analysis, it was found that a significant increase in average nanotube length (mean: 838.3 ± 470.4 nm, max: 2400 nm) and standard deviation from the control measurement (473.7 ± 179.5 nm) indicating molecular junction formation.

As shown previously with semiconducting/metallic mixture SWCNTs, metallic DNA-SWCNTs show similar nanotube lengths after molecular junction formation. As described in section 3.2, the average nanotube length demonstrates predominantly single junctions formed between two SWCNTs, when compared to pristine nanotube lengths. The maximum length demonstrates multiple junctions formed – this indicates that irrespective of SWCNT electrical properties (or chirality), DNA-SWCNTs will behave in a similar manner regarding single-molecule junction formation when PPD is present as a linker.

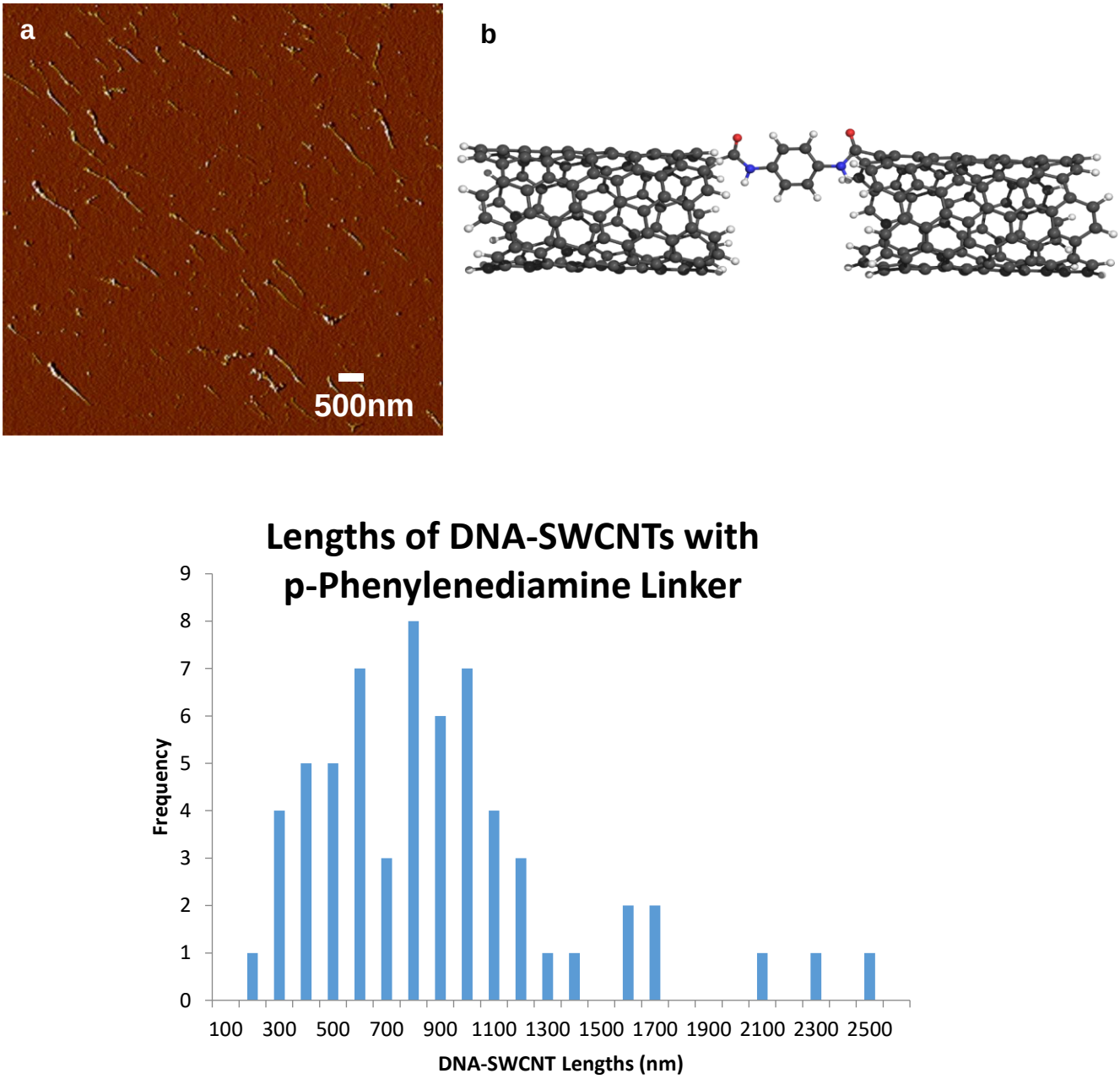

Figure 24. a) AFM topographical image displaying metallic pristine DNA-wrapped SWCNTs. b) Schematic of pristine DNA-wrapped SWCNT. c) Histogram of metallic DNA-wrapped SWCNTs measured. Average tube length: 838.3 ± 470.4 nm.

3.4.3. Benzidine Molecular Linker with Semiconducting/Metallic Mixture DNA-SWCNTs

We also verified junction formation with a benzidine molecular linker by performing a double amidation reaction with semiconducting/metallic mixture DNA-SWCNTs as shown in Figure 25. Employing a molecular linker with an increased molecular length, *i.e.* an additional benzene ring, will establish a trend of molecular conductance versus length. Solutions of molecular junctions were cast onto hydrophobic silicon surfaces and imaged *via* AFM. Analysing AFM images and performing a statistical analysis, it was found that a significant increase in average nanotube length (mean: 849 ± 543 nm, max: 2800 nm) and standard deviation from the control measurement (429.7 ± 177 nm) had occurred, indicating molecular junction formation.

Similar to PPD, benzidine demonstrates predominant single junction formation as indicated by the average nanotube length. Once more, the maximum nanotube length measured indicates that DNA-SWCNTs linkages occur through multiple junction formation. From the lengths measured, benzidine has shown the same linker properties as PPD.

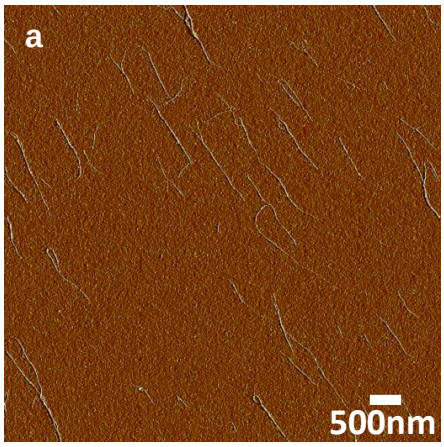

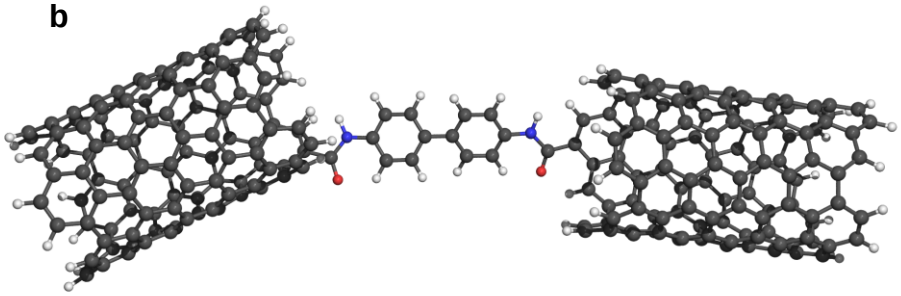

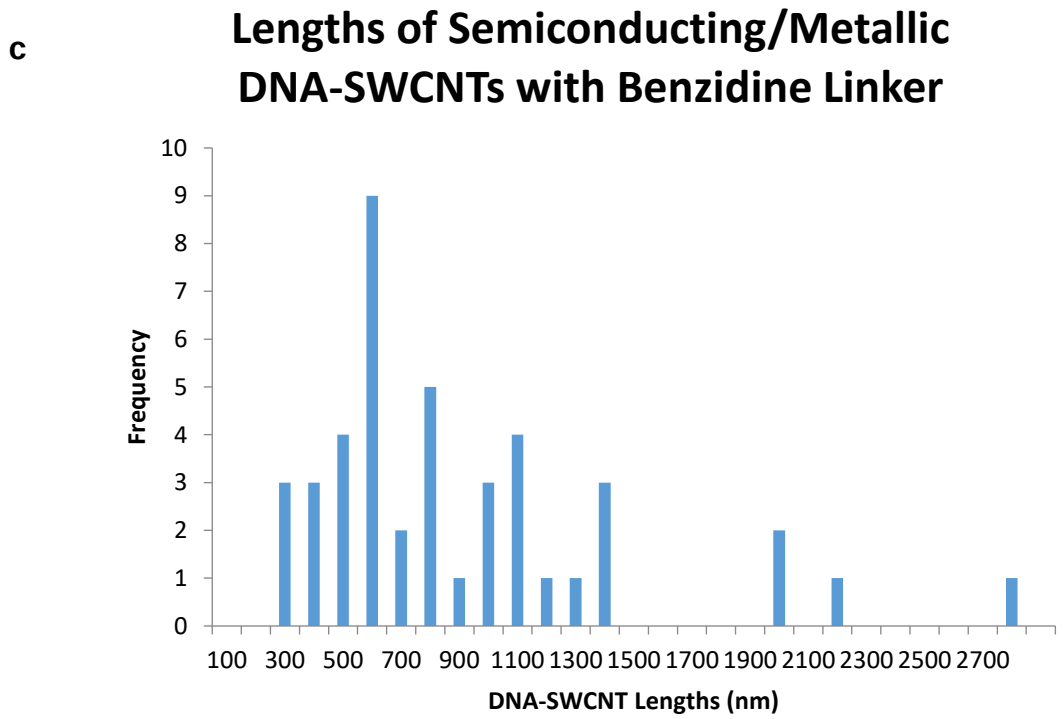

Figure 25. a) AFM topographical image displaying benzidine linked semiconducting/metallic mix DNA-wrapped SWCNTs. b) Schematic of benzidine linked molecular junction. c) Histogram of semiconducting/metallic mix DNA-wrapped SWCNTs measured. Average tube length: 849 ± 543 nm.

3.4.4. Benzidine Molecular Linker with Metallic DNA-SWCNTs

As expected, we could form benzidine-based SWCNT junctions by also employing metallic nanotubes. Figure 26 shows the typical trend as seen with previous linkers, suggesting

increasing molecular length by a single benzene ring will not impede molecular junction formation. By analysing AFM images of casts and performing a statistical analysis, it was found that a significant increase in average nanotube length (mean: 1109.9 ± 546.6 nm, max: 2500 nm) and standard deviation from the control measurement (473.7 ± 179.5 nm) had occurred, indicating successful molecular junction formation.

In this instance, benzidine displays an increased nanotube average length after junction formation compared to previous linkers and nanotube types. With metallic SWCNTs, the significant increase in nanotube length demonstrates that multiple junctions are more frequent with a benzidine molecular linker. One possible explanation of improved junction formation with metallic tubes could be driven by the orientation of pi orbitals. Therefore, it could be suggested that metallic tubes show a greater electron withdrawing effect, which improves the nucleophilicity of carboxylic terminations. However, further investigations must be performed before validating this hypothesis.

Average nanotube length indicates that up to three tubes would link *via* molecular junctions at a higher yield than previous linkers. The maximum nanotube length also demonstrates multiple junctions formed at the same length as previous linkers, demonstrating that the overall maximum nanotube length did not increase but the yield of multiple junction formation did.

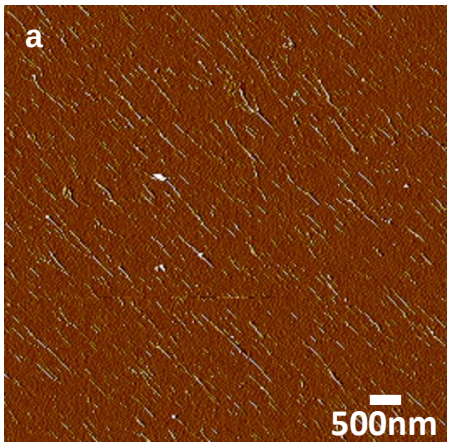

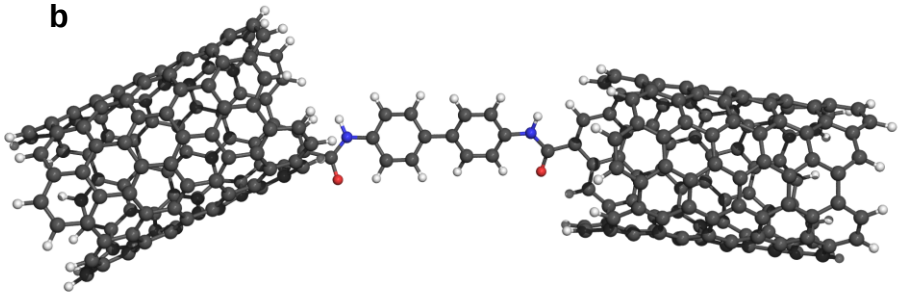

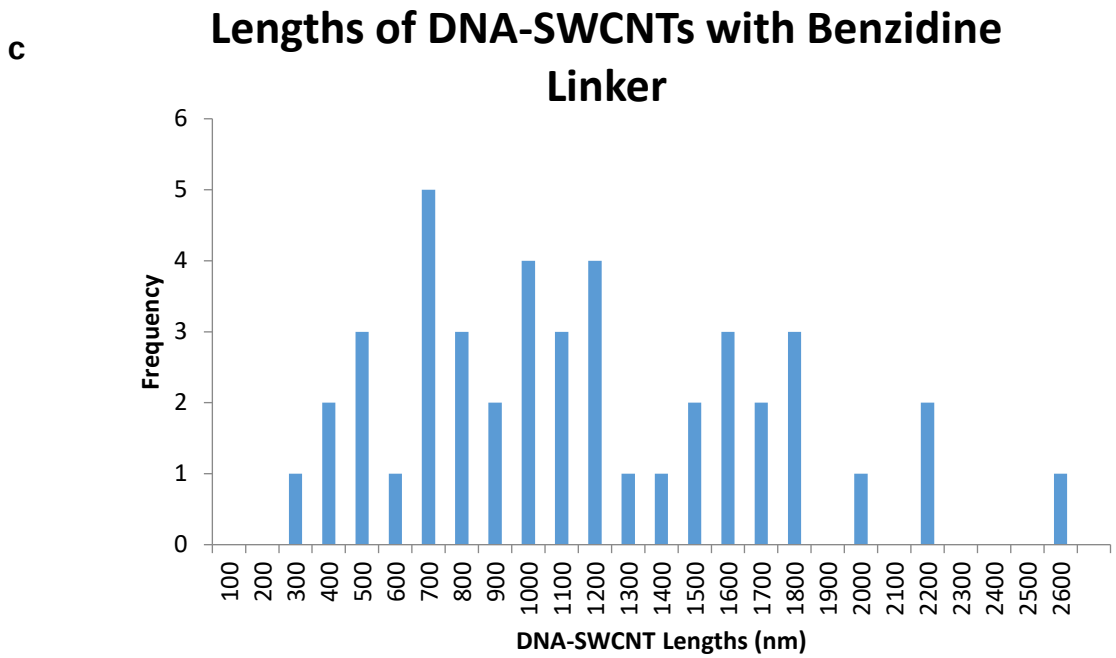

Figure 26. a) AFM topographical image displaying benzidine linked metallic DNA-wrapped SWCNTs. b) Schematic of Benzidine linked molecular junction. c) Histogram of metallic DNA-wrapped SWCNTs measured. Average tube length: 1109.9 ± 546.6 nm.

3.4.5. Terphenyl Molecular Linker with Semiconducting/Metallic Mixture DNA-SWCNTs

Completing the series of oligophenyl molecular linkers to be employed for molecular conductance measurements, a three-benzene system was utilised in a double amidation reaction. Figure 27 shows molecular junctions were formed with Terphenyl linker and DNA-SWCNTs. Analysing AFM images and performing a statistical analysis, it was found that a significant increase in average nanotube length (mean: 933 ± 452 nm, max: 2000 nm) and standard deviation from the control measurement (429.7 ± 177 nm) had occurred, indicating molecular junction formation.

Consistent to the trend observed with previous linkers, terphenyl displays the typical behaviour of conjugated diamines. Compared to previous average nanotube lengths, the average length measured with terphenyl linkers demonstrates single junctions were predominantly formed with few instances of multiple junction formation. The maximum nanotube length measured shows that multiple junctions occur with terphenyl linkers much in same way previous linkers do.

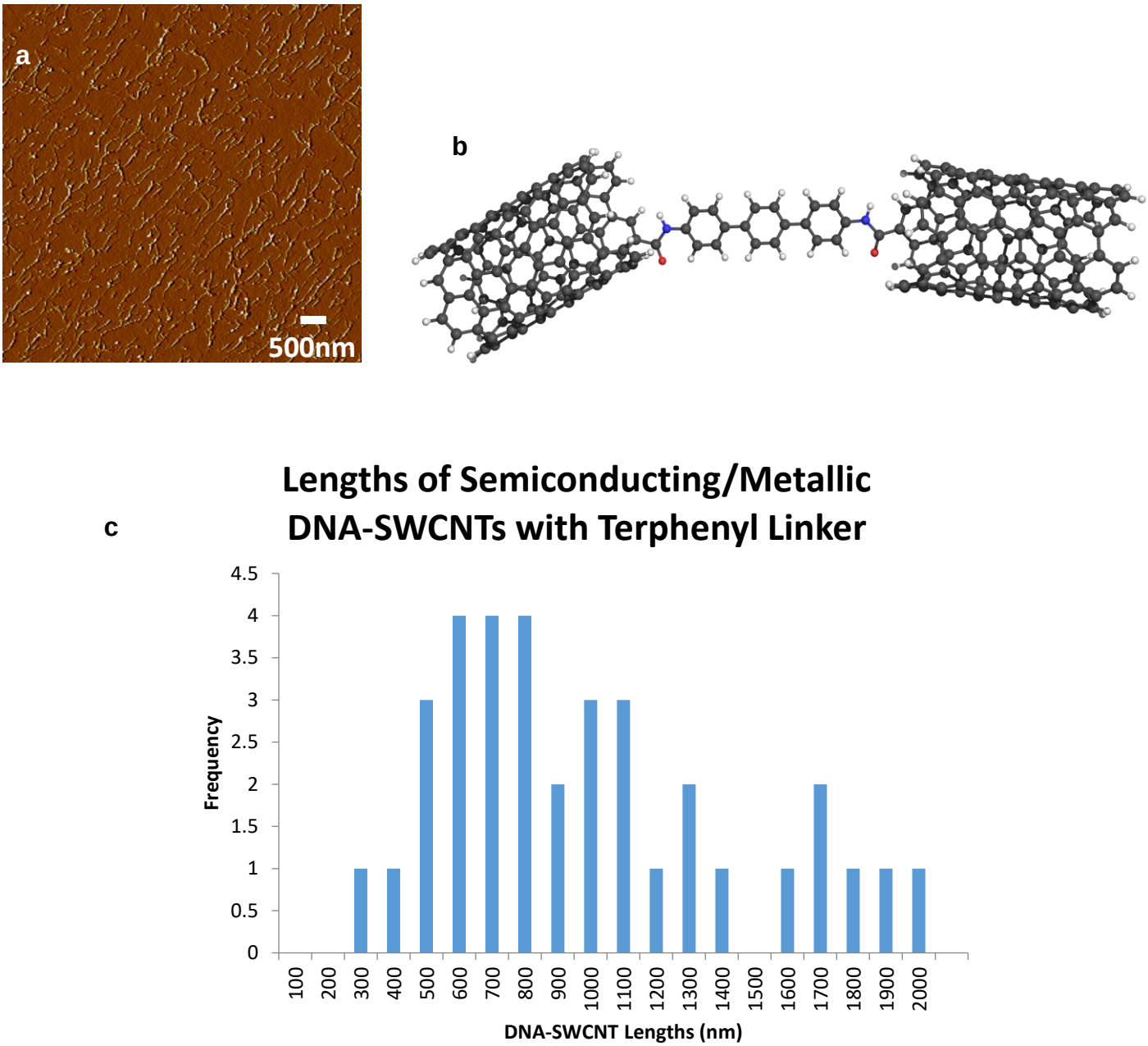

Figure 27. a) AFM topographical image displaying Terphenyl linked semiconducting/metallic mix DNA-wrapped SWCNTs. b) Schematic of Terphenyl linked molecular junction. c) Histogram of semiconducting/metallic mix DNA-wrapped SWCNTs measured. Average tube length: 933 ± 452 nm.

3.4.6. Terphenyl Molecular Linker with Metallic DNA-SWCNTs

Replicating the reaction conditions with pristine metallic nanotubes saw terphenyl linkers, as expected, form molecular junctions, as shown in Figure 28. Completing the series of molecular linkers employed to bridge SWCNTs in 1D assemblies enabled us to undertake a full investigation of the molecular conductance across both mixed semiconducting/metallic and metallic nanotubes. The formation of molecular junctions across all linkers enabled a full investigation into the trends of the electrical properties of single molecules. Through analysing AFM images of these junctions and performing a statistical analysis, a significant increase in the average nanotube length (mean: 1105.3 ± 569.1 nm, max: 2800 nm) and standard deviation from the control measurement (473.7 ± 179.5 nm) was found, consistent with molecular junction formation.

Similar to benzidine, the terphenyl linker with metallic DNA-SWCNTs displays an increased average nanotube length, demonstrating a higher yield of multiple junctions. Also, the maximum nanotube length demonstrates a similar measurement to previous linkers – indicating that the maximum lengths do not significantly change but, according to the average length, the yield of multiple junctions does increase.

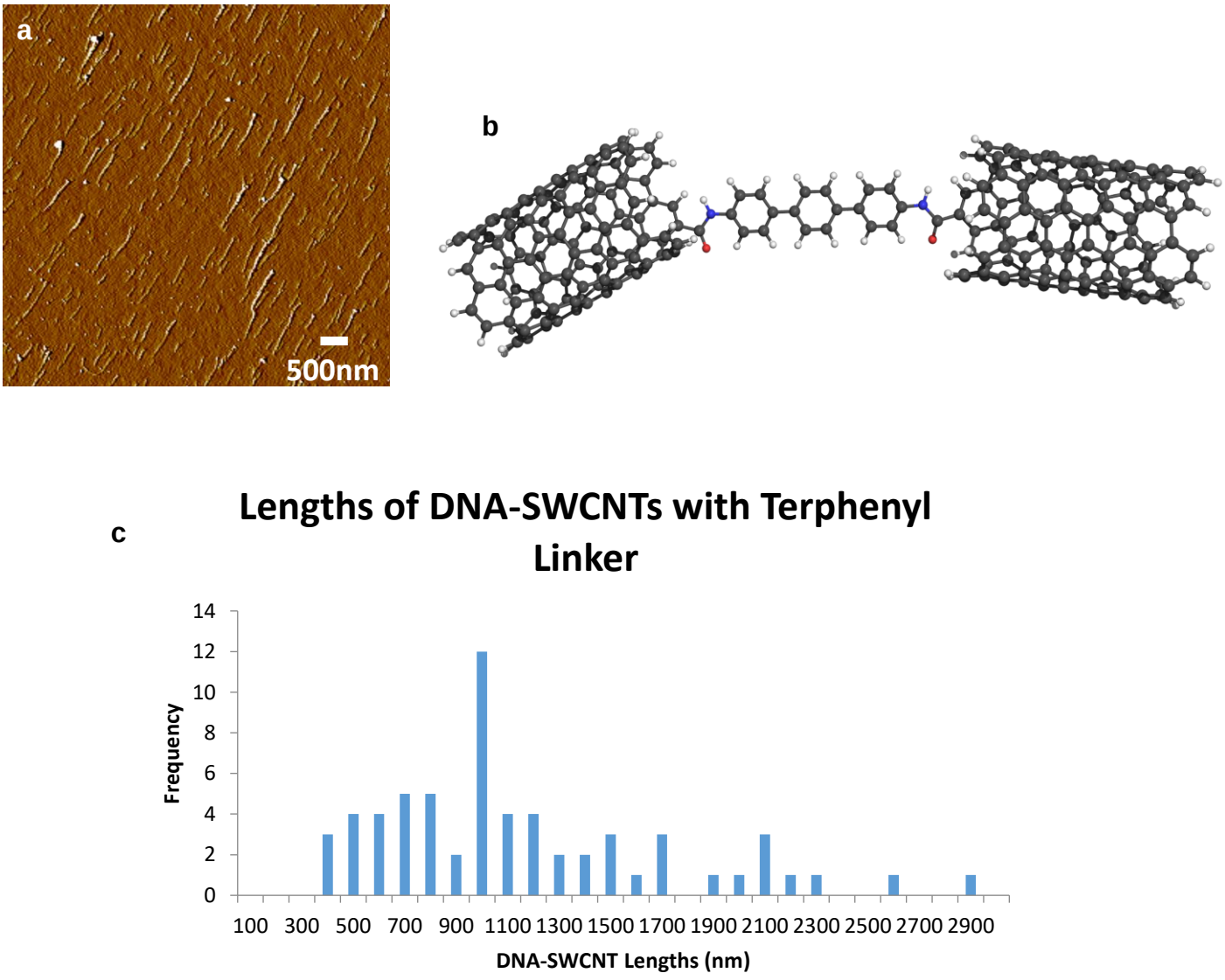

Figure 28. a) AFM topographical image displaying Terphenyl linked metallic DNA-wrapped SWCNTs. b) Schematic of Terphenyl linked molecular junction. c) Histogram of metallic DNA-wrapped SWCNTs measured. Average tube length: 1105.3 ± 569.1 nm.

3.4.7. Diaminofluorene (DAF) Molecular Linker with Semiconducting/Metallic Mixture DNA-SWCNTs

We further investigated the capability of forming junctions with different types of molecular linkers. Diaminofluorene (DAF) has a very rigid molecular structure due to an additional connecting C-C bond between benzene rings. It has been reported that linkers with freely rotating benzene rings will exhibit a reduced conductivity.[161] Therefore, forming molecular junctions with a linker with restricted bond rotation could be investigated and compared to benzidine and terphenyl systems. As previously described, double amidation reaction with semiconducting/metallic mixture DNA-SWCNTs and DAF linker was performed to form molecular junctions as shown in Figure 29. Solutions of molecular junctions were cast onto hydrophobic silicon surfaces and imaged *via* AFM. Analysing AFM images and performing a statistical analysis, it was found that a significant increase in average nanotube length (mean: 754 ± 394 nm, max: 2100 nm) and standard deviation from the control measurement (429.7 ± 177 nm) indicating molecular junction formation.

DAF linker exhibits the lowest average nanotube length out of all linkers employed in junction formation reactions indicating a lower yield, estimated 55%. However, the maximum nanotube measurement shows a length comparable to previous linkers, demonstrating the ability to form multiple junctions.

Molecular junction yield was estimated by calculating the percentage of nanotubes with a length of 800 nm and above (i.e. minimum lengths of molecular junctions) out of the total number of nanotubes measured (i.e. both pristine tubes and molecular junctions).

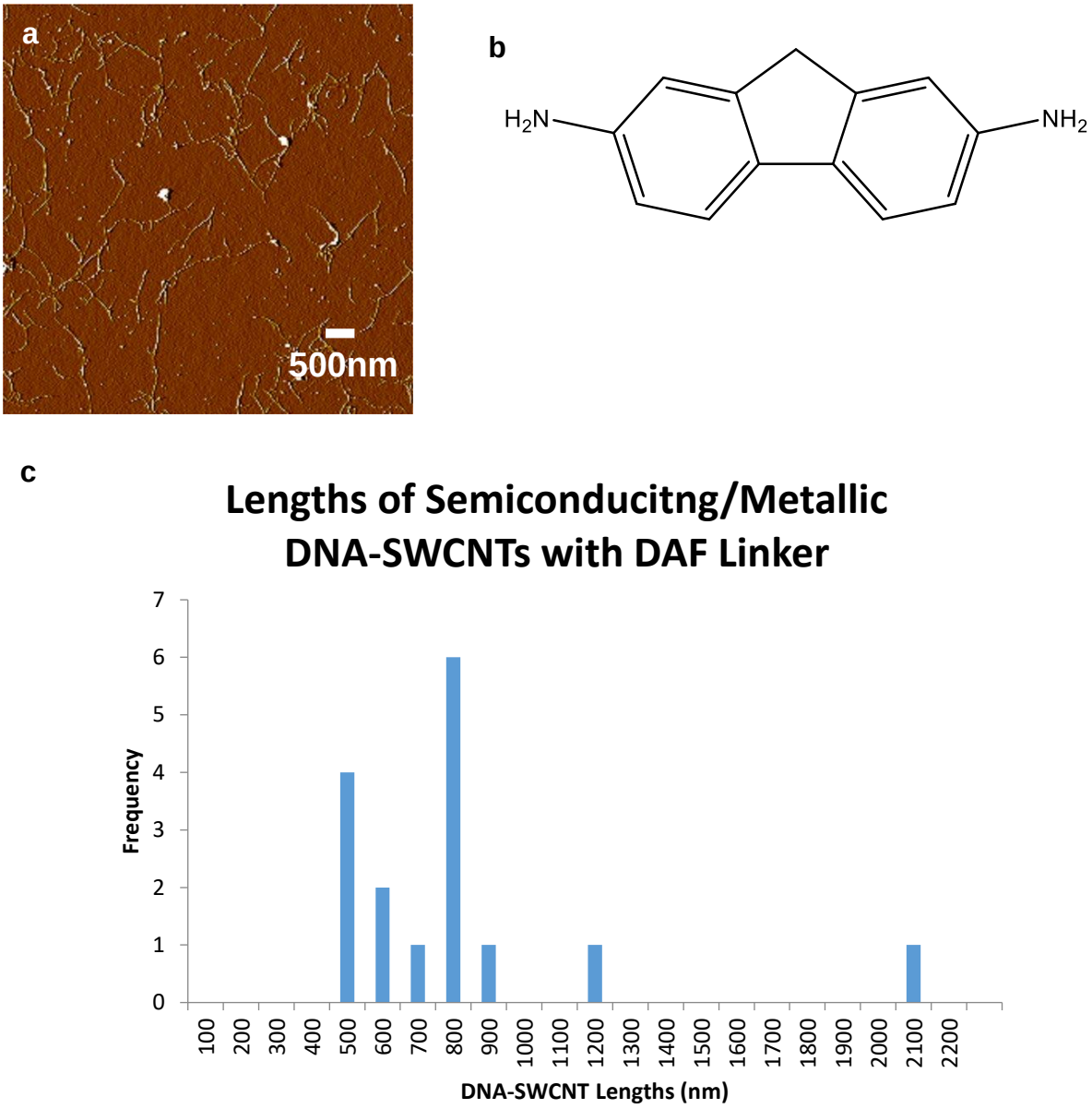

Figure 29. a) AFM topographical image displaying semiconducting/metallic mix DNA-wrapped SWCNTs with activation solution with DAF linker present. b) Structure of DAF. c) Histogram of metallic semiconducting/metallic mix DNA-wrapped SWCNTs measured. Average tube length: 754 ± 394 nm.

3.4.8. Diaminofluorene (DAF) Molecular Linker with Metallic DNA-SWCNTs

Pristine metallic nanotubes were employed to form molecular junctions with DAF to verify the formation of 1D assemblies. As shown in Figure 30, DAF displays the consistent trend (as seen with all previous molecular linkers) of forming junctions irrespective of nanotube type. Solutions of molecular junctions were cast onto hydrophobic silicon surfaces and imaged *via* AFM. Analysing AFM images and performing a statistical analysis, a significant increase in length and standard deviation was found (mean: 838 ± 470 nm, max: 2500 nm), therefore indicating an increase in average nanotube length and standard deviation from the control measurement (473.7 ± 179.5 nm) had occurred, indicating molecular junction formation.

Metallic DNA-SWCNTs with DAF linker displays an overall increase in the average nanotube length – one that is comparable to previous linkers. The average length indicates that single junctions are predominant but, similarly to previous linkers, the maximum length measured demonstrates multiple junctions do occur (estimated yield: 56% molecular junction formation; 12.5% multiple molecular junctions). Results on DAF linker with both types of SWCNTs illustrate the performance of the linker is weaker than the previous examples but still displays statistically significant results.

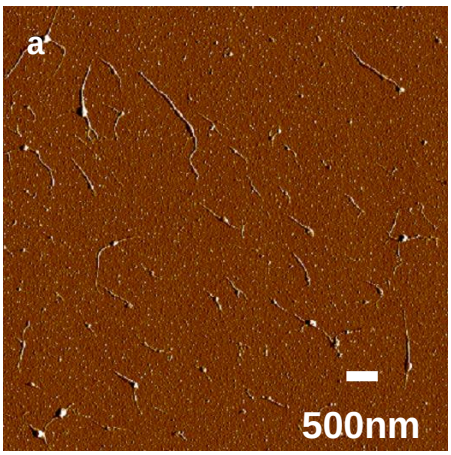

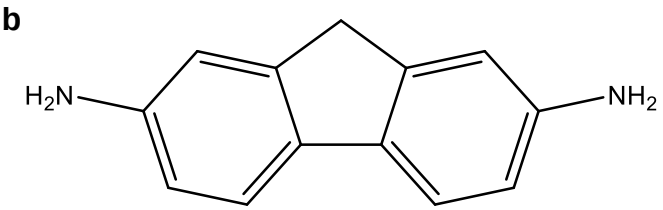

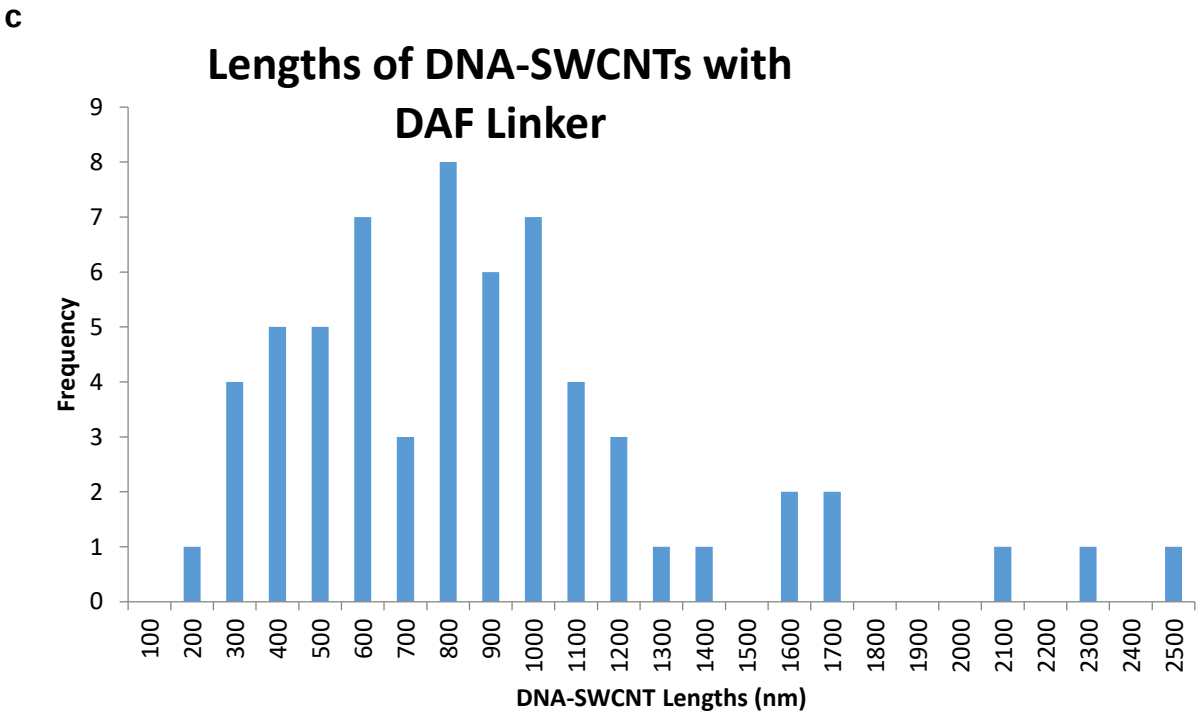

Figure 30. a) AFM topographical image displaying DNA-wrapped SWCNTs with activation solution with DAF linker present. b) structure of DAF. c) Histogram of metallic DNA-wrapped SWCNTs measured. Average tube length: 838 ± 470 nm.

3.4.9. 4,4'-(ethyne-1,2-diyl)dianiline (Dianiline) Molecular Linker with Semiconducting/Metallic Mixture DNA-SWCNTs

Differently to DAF, the dianiline linker has restrictive bond rotation due to its alkyne functionality. Exploring alternative linkers with restrictive bond rotations could lead to expanding the oligophenyl series and comparisons made between junction formation performance versus types of restrictive bonding. As shown in Figure 31, dianiline shows molecular junction formation with a linker that displays both restrictive bond rotation and an increased molecular length compared to DAF. Analysing AFM images and performing a statistical analysis, it was found that a significant increase in average nanotube length (mean: 924 ± 443 nm, max: 2500 nm) and standard deviation from the control measurement (429.7 ± 177 nm) indicating molecular junction formation.

The dianiline linkers displays an average nanotube length comparable to the terphenyl linkers and could indicate a higher yield of multiple junctions than typical linkers. Maximum nanotube lengths also indicate multiple junction formation. Both factors demonstrate dianiline performs as well as previous linkers despite the inclusion of a central alkyne group.

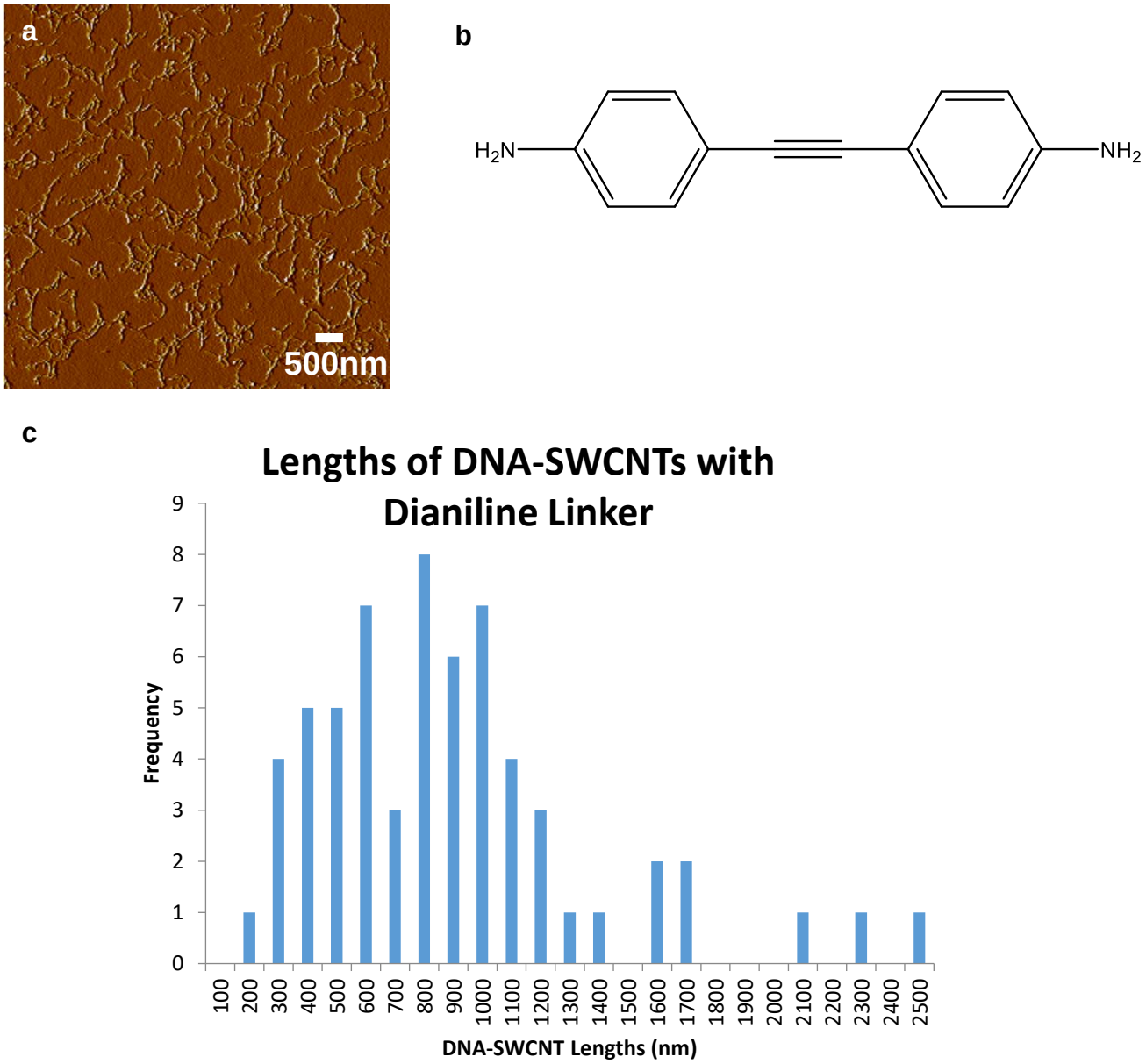

Figure 31. a) AFM topographical image displaying DNA-wrapped SWCNTs with activation solution with Dianiline linker present. b) structure of Dianiline. c) Histogram of metallic DNA-wrapped SWCNTs measured. Average tube length: 924 ± 443 nm.

3.4.10. 4,4'-(ethyne-1,2-diyl)dianiline (Dianiline) Molecular Linker with Metallic DNA-SWCNTs

As shown in Figure 32, dianiline forms molecular junctions *via* double amidation reaction in the expected way, continuing the trend of all diamine conjugated oligophenyls used in this study. Solutions of molecular junctions were cast onto hydrophobic silicon surfaces and imaged *via* AFM. Analysing AFM images and performing a statistical analysis, it was found that a significant increase in average nanotube length (mean: 1015 ± 507 nm, max: 2300 nm) and standard deviation from the control measurement (473.7 ± 179.5 nm) and therefore indicates molecular junction formation.

Average nanotube length indicates that multiple junctions form at a higher rate than a typical conjugated linker but not as high a benzidine. Metallic SWCNTs with dianiline linkers show an increased average nanotube length compared to semiconducting/metallic mixture nanotubes, in keeping with the trend observed with previous linkers. Additionally, the maximum nanotube length is comparable to previous results, demonstrating multiple junctions formed with dianiline linkers.

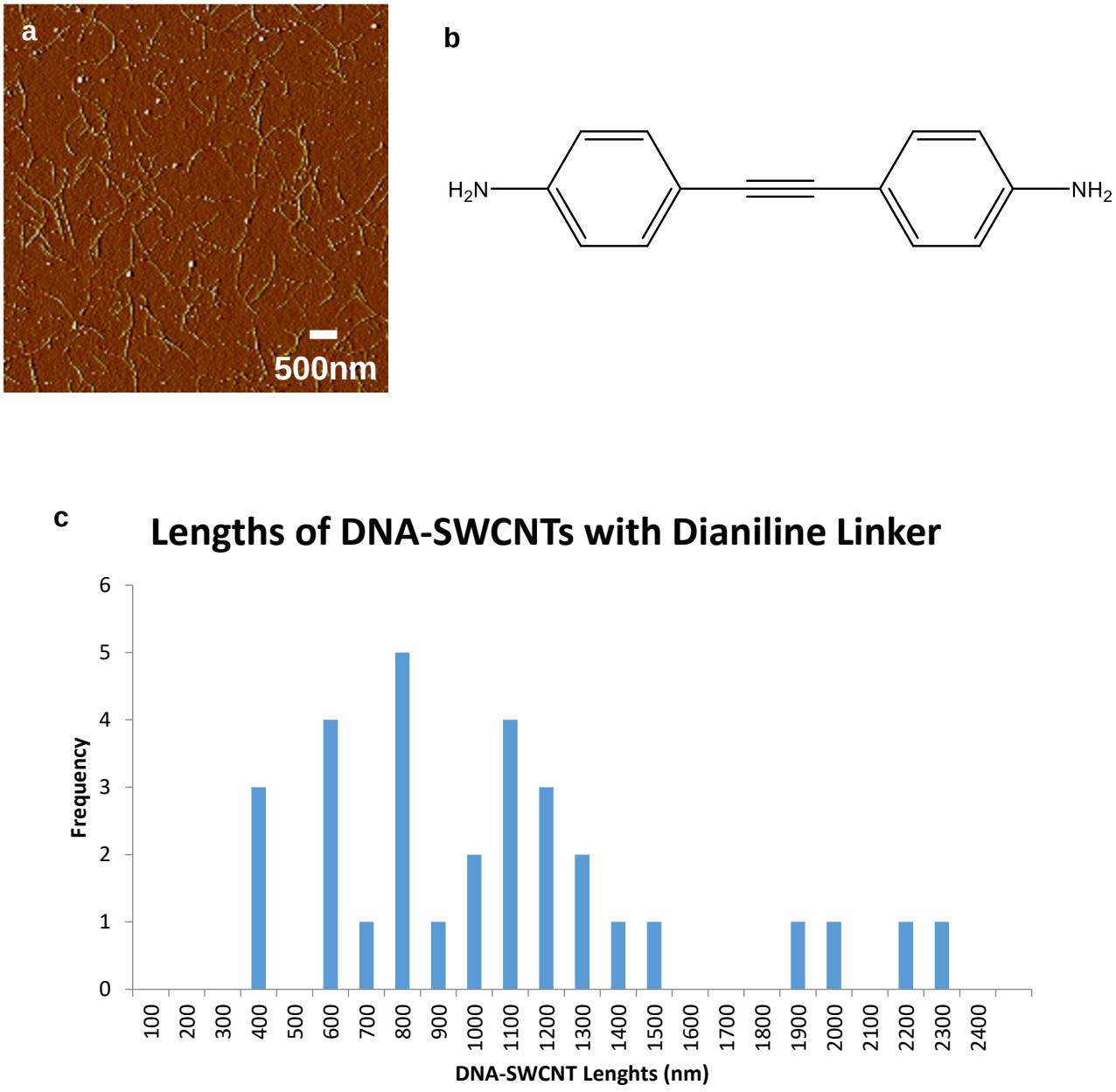

Figure 32. a) AFM topographical image displaying DNA-wrapped SWCNTs with activation solution with Dianiline linker present. b) Structure of Dianiline. c) Histogram of metallic DNA-wrapped SWCNTs measured. Average tube length: 1015 ± 507 nm.

All results of molecular junction formation procedures are tabulated in Table 2 and shown in Figure 33. The average lengths with standard deviations of both pristine and molecular junctions of semiconducting/metallic mixture and metallic SWCNTs were all recorded.

Table 2. Average length of each SWCNT and molecular junction.

Conjugated Diamine Linker	**SWCNT Electrical Type**	**Average Nanotube Length (nm)**	**Maximum Nanotube Length (nm)**
None – pristine SWCNTs	Semiconducting/Metallic	**429 ± 177**	1200
None – pristine SWCNTs	Metallic	**473 ± 179**	1000
PPD	Semiconducting/Metallic	**890 ± 593**	3200
PPD	Metallic	**838 ± 470**	2400
Benzidine	Semiconducting/Metallic	**849 ± 543**	2800
Benzidine	Metallic	**1110 ± 547**	2500
Terphenyl	Semiconducting/Metallic	**933 ± 452**	2000
Terphenyl	Metallic	**1105 ± 569**	2800
DAF	Semiconducting/Metallic	**754 ± 394**	2100
DAF	Metallic	**838 ± 470**	2500
Dianiline	Semiconducting/Metallic	**924 ± 443**	2500
Dianiline	Metallic	**1015 ± 507**	2300

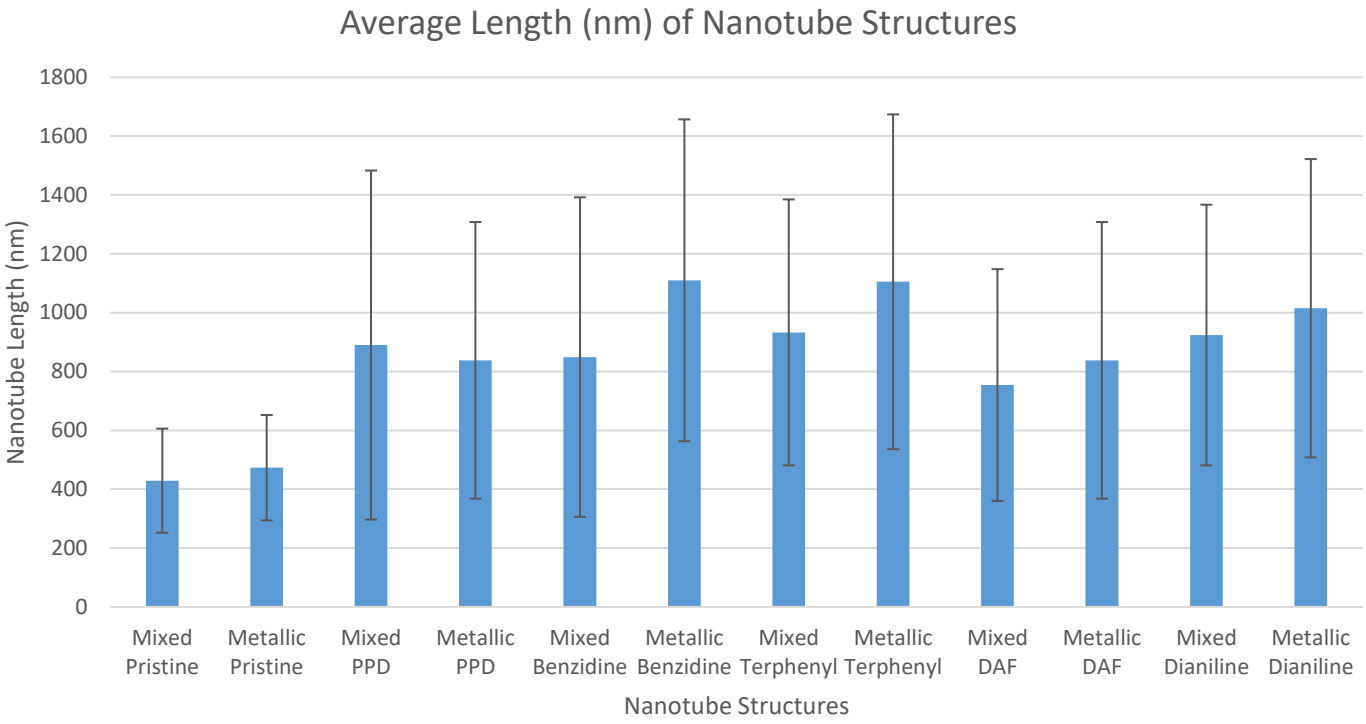

Figure 33. Graph showing the average length of the different types of nanotube structures.

All results with conjugated diamines show average lengths greater than 750 nm, indicating molecular junctions were formed with a range of diamine molecular linkers with SWCNTs that display both metallic and semiconducting electronic properties.

Control experiments were performed to ensure single molecule junctions were synthesised between terminal SWCNTs. If the lengths of nanotubes were similar to those of pristine SWCNTs, then it is reasonable to suggest that no junction formation was taking place. The results of control experiments are summarised in Table 3. All control experiments were performed with metallic SWCNTs and each experiment was designed to specify the efficacy of a single variable.

Table 3. Average SWCNT lengths in control experiments.

Control Experiment	Average Length of SWCNTs (nm)
No Molecular Linker Present	**467.5 ± 149.8**
No Activation Solution Present	**452.7 ± 134.5**
Molecular Linker without Amine Functional Groups	**433.3 ± 132.2**

3.4.11. No Molecular Linker Present – Control Experiment

As previously described, a typical junction formation experiment was performed without any molecular linker added to observe the efficacy of a diamine linker. Solutions were cast onto hydrophobic surfaces and imaged *via* AFM. Figure 34 shows the AFM image and histogram of nanotube lengths measured. Statistical analysis was performed on the lengths measured (mean: 467.5 ± 149.8 nm, maximum: 800 nm) and compared to pristine metallic SWCNT lengths (473 ± 179 nm). Pristine lengths and average measured lengths are comparable, demonstrating that no molecular junctions had formed and therefore underlining the necessity in including a molecular linker in junction formation experiments.

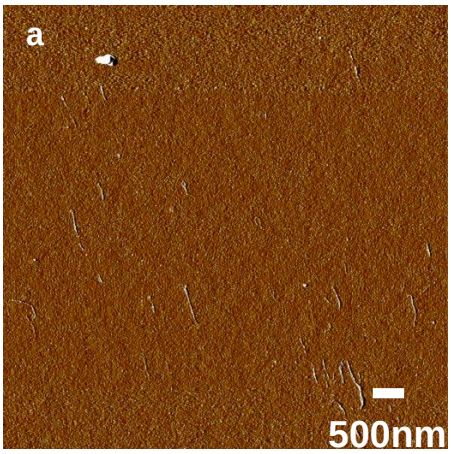

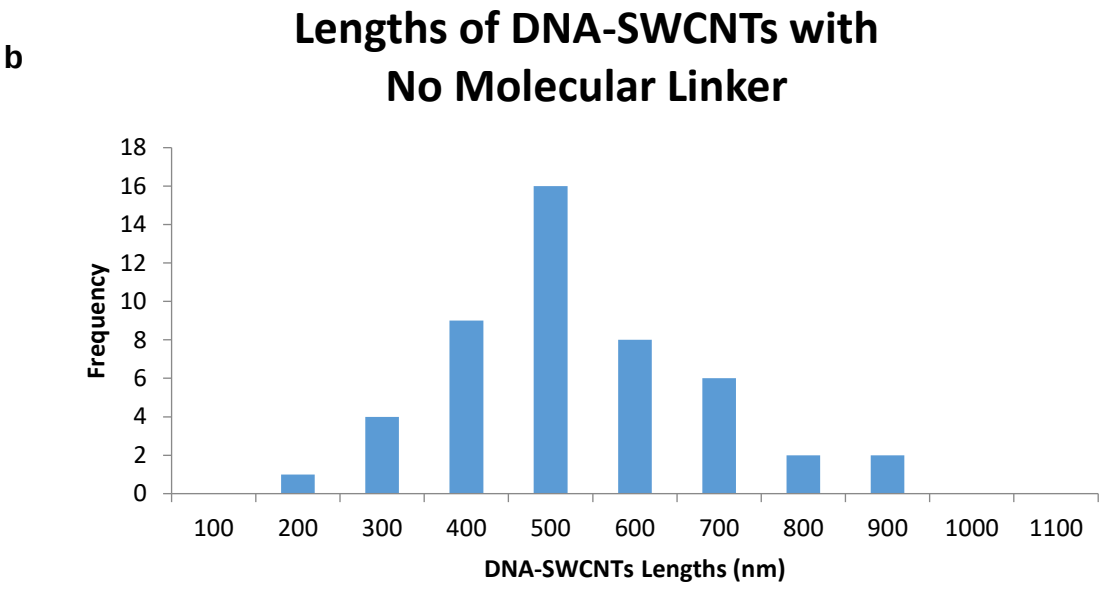

Figure 34. a) AFM topographical image displaying DNA-wrapped SWCNTs with activation solution with no linker present. b) Histogram of metallic DNA-wrapped SWCNTs measured. Average tube length: 467.5 ± 149.8 nm. This control experiment shows that no molecular junctions are formed when the molecular linker is not present.

3.4.12. *p*-Phenylenediamine (PPD) Molecular Linker without Activation Solution – Control Experiment

Typical junction formation reaction was performed with PPD molecular linker but with DI water replacing activation solution to underline the need to activate DNA-SWCNTs. Solutions were cast onto hydrophobic surfaces and imaged *via* AFM. Figure 35 displays the AFM image and histogram of lengths measured. Statistical analysis on lengths were performed (mean:

452.7 ± 134.5 nm, maximum: 800 nm) and compared to pristine metallic DNA-SWCNTs (473 ± 179 nm). Average nanotube lengths and pristine nanotube lengths are comparable, indicating that no molecular junctions had formed and therefore highlighting the need to include an activation solution to form molecular junctions.

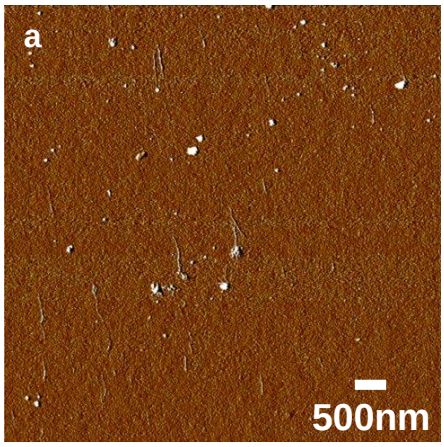

b

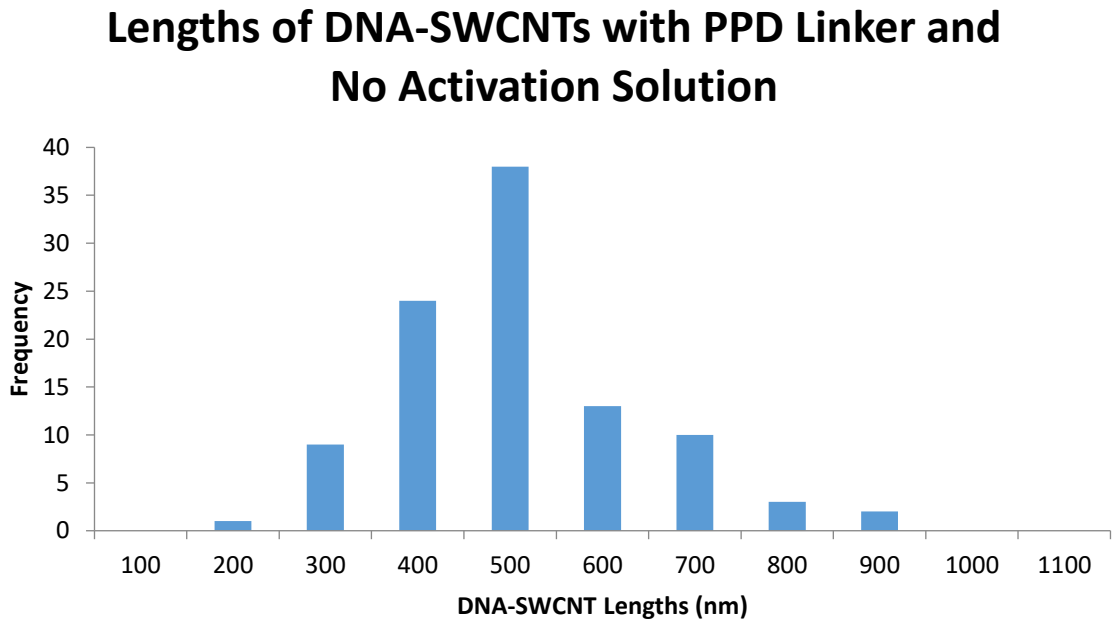

Figure 35. a) AFM topographical image displaying DNA-wrapped SWCNTs and PPD linker with no activation solution present. b) Histogram of metallic DNA-wrapped SWCNTs measured. Average tube length: 452.7 ± 134.5 nm. This control experiment shows that no junctions are formed when the activation solution is not present.

3.4.13. 4-Toluenesulfonyl Chloride Molecular Linker – Control Experiment

Typical junction formation reaction was performed with 4-toluenesulfonyl chloride acting as molecular linker to underline the necessity of diamine molecular linkers. Solutions were cast onto hydrophobic silicon surfaces and imaged *via* AFM. Figure 36 displays an AFM image and histogram of lengths measured of nanotubes. Statistical analysis was performed on lengths measured (mean: 433.3 ± 132.2 nm, maximum: 900 nm) and compared to pristine metallic DNA-SWCNTs (473 ± 179 nm). Average nanotube lengths and pristine metallic SWCNTs lengths were comparable, indicating no molecular junctions had formed and therefore underlining the necessity the presence of diamine molecular linkers.

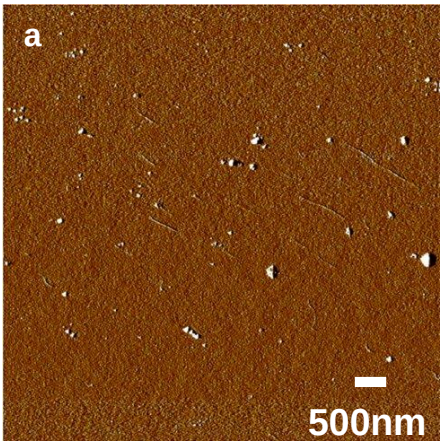

b

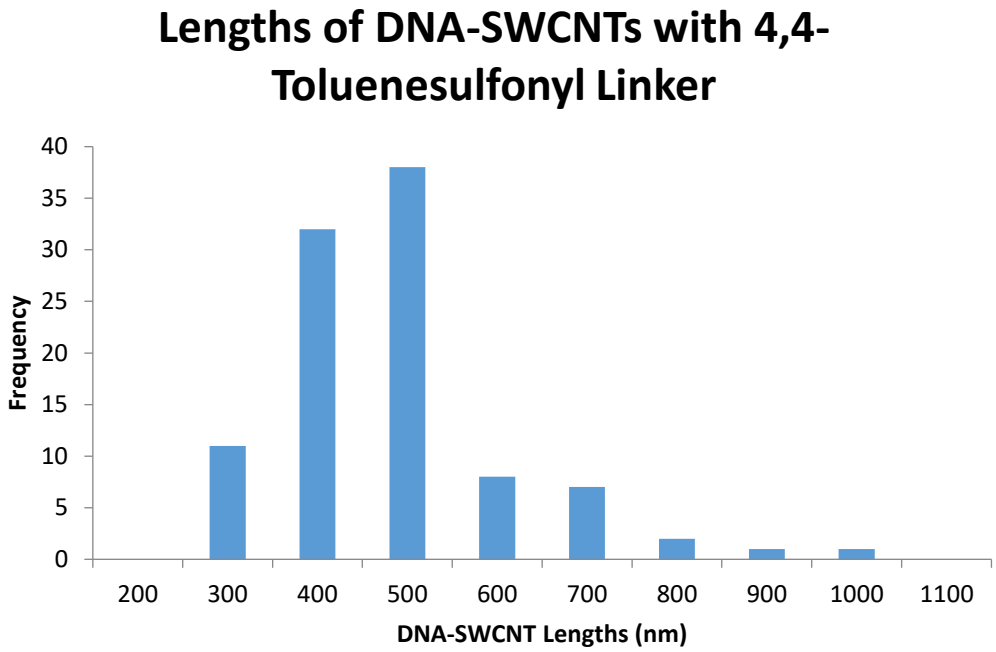

Figure 36. a) AFM topographical image displaying DNA-wrapped SWCNTs with 4-Toluenesulfonyl (Sigma Aldrich) molecular linker and activation solution. b) Histogram of metallic DNA-wrapped SWCNTs measured. Average tube length: 433.3 ± 132.2 nm. This control experiment shows that no junctions are formed when oligophenyl molecular linkers do not contain amine functional groups.

Standard deviations have been calculated based on the range of nanotube lengths measured.

3.5. DNA-SWCNT Width Analysis

The widths of SWCNTs were also measured to ensure only terminal junctions were being formed. If any side-by-side junctions (two-dimensional) junctions were formed, the widths of tubes would be at least twice the average width of pristine SWCNTs.

Using NanoScope Analysis software, heights of all SWCNTs were measured. Structures measured were pristine DNA-SWCNTs, DNA-SWCNTs with EDC and sulfo-NHS with no linker, molecular junctions formed using PPD, benzidine, and terphenyl molecular linkers.

Once height profiles were obtained, widths of tubes were measured. The radius of the AFM tip used was also taken into consideration: TESPA tips (Bruker, spring constant 40 N/m) with a radius of 12 nm.

Widths of structures were determined by utilising obtained values and applying the equations[162]:

$2\Delta = 2\sqrt{h(2R-h)}$

$W_E = W_m - 2\Delta$

Where:

h = height of DNA-SWCNT (nm)

R = radius of AFM tip (nm)

W_E = width effective (nm)

W_m = width measured (nm)

2Δ = tip broadening coefficient

Width effective values were calculated for 100 DNA-SWCNTs for each structure type in which average values and standard deviations were obtained and shown in Table 4.

Table 4. Average width effective of DNA-SWCNT Structures.

DNA-SWCNT Structures	**Average Width Effective (nm)**
Pristine DNA-SWCNT	**4.16 ± 0.68**
DNA-SWCNT with EDC and Sulfo-NHS (no linker present)	**4.53 ± 0.86**
DNA-SWCNTs with PPD	**4.73 ± 0.90**
DNA-SWCNTs with Benzidine	**4.79 ± 0.75**
DNA-SWCNTs with Terphenyl	**4.81 ± 0.76**

Our results show that widths of all DNA-SWCNT structures are in concordance with each other. Pristine DNA-SWCNTs display a narrower width on average compared to molecular junctions. This may be attributed to the use of EDC, sulfo-NHS, MES, TPBS buffers and molecular linkers in the formation of molecular junctions. We hypothesise that each reagent binds or aggregates onto DNA strands wrapped around tubes, giving the appearance of wider structures. This is further supported by the presence of EDC and sulfo-NHS in the 'no linker' control experiment.

If tubes were bundled together, height profiles of tubes would demonstrate multiple peaks and broader standard deviation values. DNA-SWCNTs used have diameters between 2-5 nm, therefore if tubes were bundled together, widths of up to 10 nm would have been measured. However, as table 4 shows, this was not the case and it is reasonable to assume that no tube bundling has occurred and all increased values arise from the presence of experimental reagents.

3.6. Density Functional Theory (DFT) Calculations

Without DNA present, diameters of SWCNTs are approximately 1 nm. Because of the small diameter of the SWCNTs employed in this study and due to steric hindrance effects, it is expected that only one molecule can bridge nanotubes in end-to-end assemblies. Furthermore, the presence of predominantly linear junctions, rather branched (or Y-shaped) configurations, from all successful linkers employed strongly indicates the presence of a single bridging molecule. Two or more molecules would present multiple binding sites that might induce the formation of branched junctions.

To support our observations of predominantly one molecule between SWCNTs, Dr. Rachel Crespo-Otero performed density functional theory (DFT) calculations at PBE0-D3/SV(P) level of theory considering water as the solvent (COSMO level).[163–166] Calculations show the formation of linear junctions where two molecules bridge two nanotubes is energetically less favourable than junctions with one bridging molecule, as shown in Figure 37. A second molecule in the junction induces a significant strain, increasing the energy of formation of SWCNT junctions linked by two molecules is unlikely to occur. These findings allow us to reasonably assume that we are assembling predominantly single-molecule junctions.

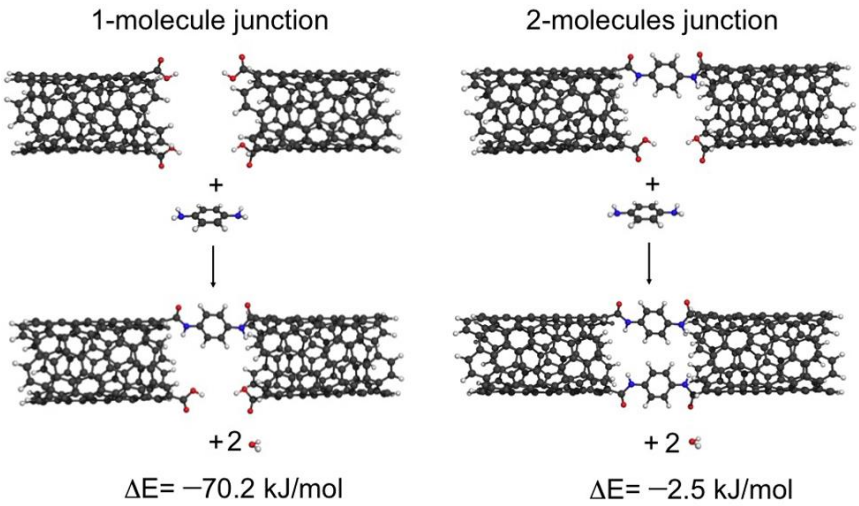

Figure 37. Reactions of formation for linear junctions with one and two bridging molecules. The energies were obtained at PBE0-D3/SV(P) level of theory considering water as the solvent (COSMO model). Reprinted with permission from J Am Chem Soc. 2016;138(9):2905-2908. Copyright 2016 American Chemical Society.

3.7. Conductive-AFM Investigations

As part of the collaboration across the Palma research group, investigations *via* conductive-AFM were carried out on our CNT-based molecular junctions. Led by PhD candidate Jingyuan Zhu, we investigated the electrical properties of molecular junctions formed in this study. The current-voltage (*I-V)* characteristics were measured as a function of the distance between a metallic AFM tip used as a mobile electrode and a fixed macroscopic metal electrode, as shown in Figure 38. As reported in literature, the technique of utilising a metallic AFM tip as a mobile electrode is well established.[125,157,167] Exploiting the mobile electrode, measurements of force controlled *I-V* responses (AFM PeakForce TUNA mode, Bruker) were taken at different locations along individual molecular junctions.

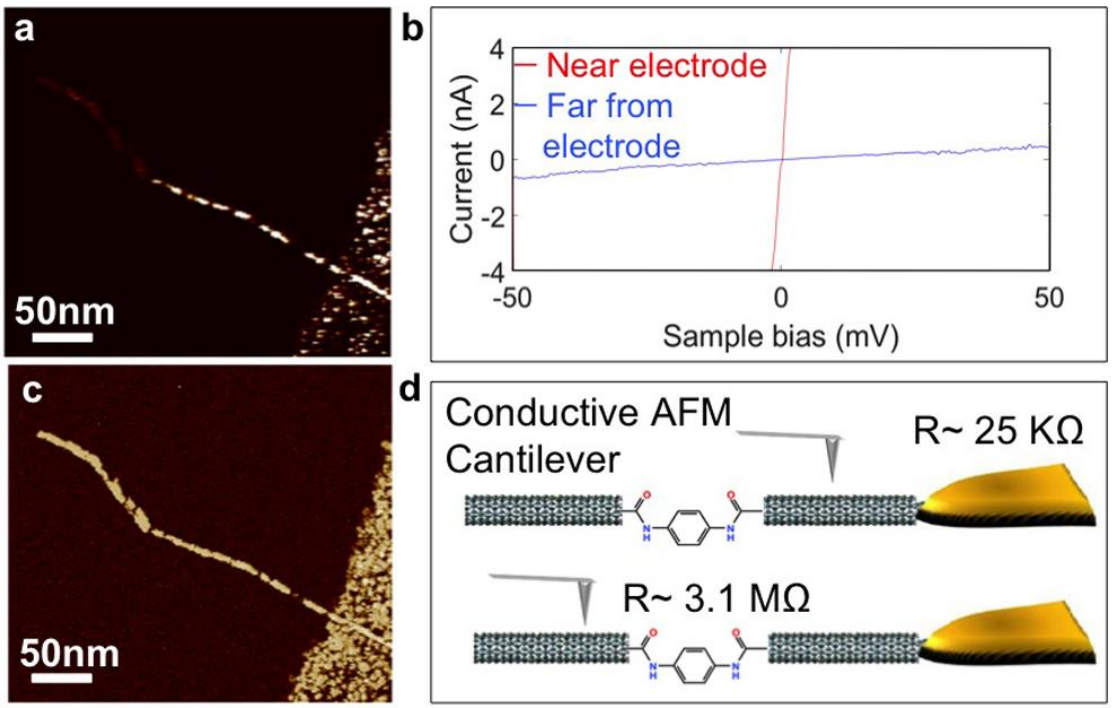

Figure 38. a) Representative Conductive AFM image of a MTJ formed using PPD as the molecular linker, and interfaced to a macroscopic metal electrode. b) Representative I-V curves recorded at selected points across the MTJ: red line for measurements near the macroscopic electrode, and blue line for measurements at the far end from the macroscopic electrode. c) Phase AFM image of the MTJ shown in (a). d) Schematic of the conductive AFM measurements on the MTJs. Reprinted with permission from J Am Chem Soc. 2016;138(9):2905-2908. Copyright 2016 American Chemical Society.

3.7.1. Molecular Conductance of PPD linked Molecular Junctions

The resistance values were determined from the inverse-slope of the *I-V* traces, and compiled into histograms, with each count corresponding to a single *I-V* curve. As shown in Figure 39, the histograms were plotted on log axes provided normal distributions. Generally, when plotted on log axes, two peaks were obtained, one corresponding to junction positions near the macroscopic electrode and one corresponding to measurements after the molecular junction. The difference in resistance can be ascribed to the presence of the molecule between SWCNTs forming the MTJs. The peaks were fit to Gaussians and the centre values were then taken as the junction resistances. Uncertainty values are derived from the standard deviation of the measurements from the full width at half maximum in the peak area.

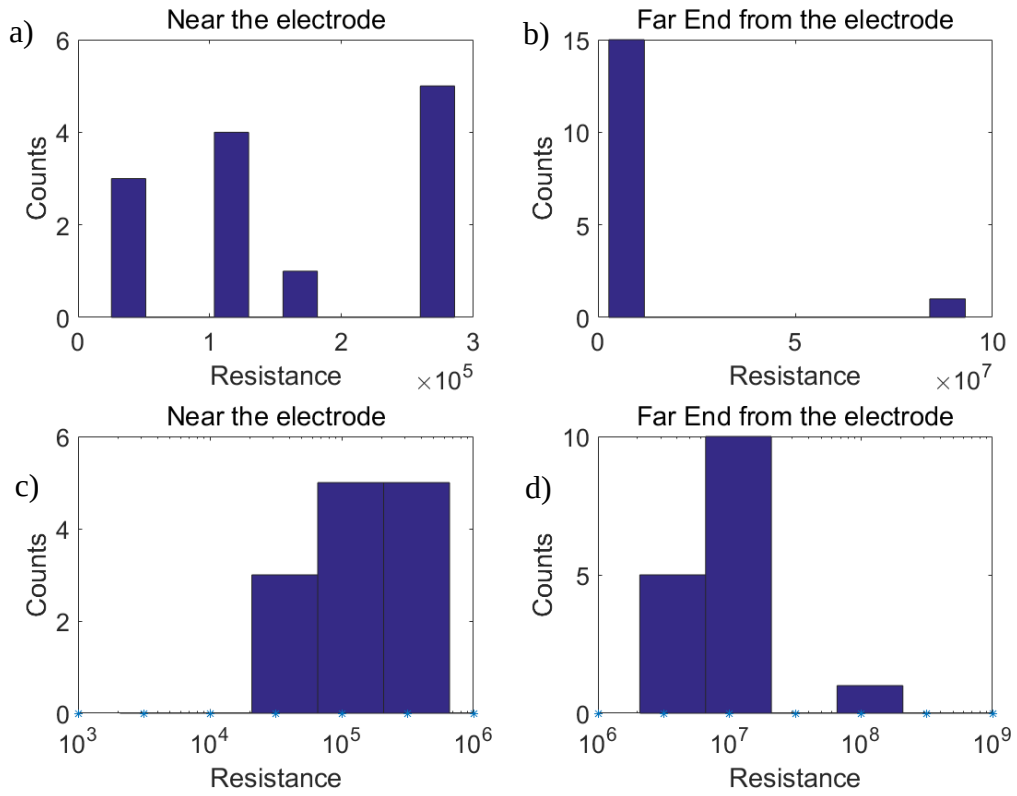

Figure 39. a) Example of representative resistance histogram of MTJs of PPD near the macroscopic electrode. b) Resistance histogram of MTJs of PPD at the far end from the electrode. c) Resistance histogram (log axes) of MTJs of PPD near the electrode. d) Resistance histogram (log axes) of MTJs of PPD at the far end from the electrode. Reprinted with permission from J Am Chem Soc. 2016;138(9):2905-2908. Copyright 2016 American Chemical Society.

The contact resistance of the SWCNT was determined by acquiring $I-V$ curves near the macroscopic electrode (between 30 and 120 nm). The resistance (R) was determined as ~25 KΩ, which is the typical contact resistance for single SWCNTs using metal contacts.[167,168] R was calculated using Equation 3, as shown:

Equation 3. Calculation of resistance (R) of a single molecule

$$R = R_c e^{\beta L}$$

Where:

R_c = contact resistance (KΩ)

β = decay constant ($Å^{-1}$)

L = tunnelling distance taken to be the length of the molecule (Å)

There was not any noticeable increase in resistance along the nanotube within this distance range, as indeed expected for short SWCNTs. On repeating the measurements along the same SWCNT we obtained the same R within a 4% error, indicating that the AFM tip did not damage the SWCNT surface. Table 5 outlines the conductance values (G_0) for each molecular linker employed in each junction.

Table 5. Molecular linkers employed and measured MTJ conductance values.

Molecule	**Conductance (G_0)**
PPD	$8.0 \times 10^{-3} \pm 2.4 \times 10^{-3}$
Benzidine	$1.4 \times 10^{-3} \pm 5.5 \times 10^{-4}$
Terphenyl	$1.8 \times 10^{-4} \pm 4.2 \times 10^{-5}$

Conductance values were calculated by Equation 4, as shown:

Equation 4. Calculation of molecular conductance

$$G = G_c e^{-\beta L}$$

Where:

G = molecular conductance

G_c = contact conductance

Conductance values were plotted against molecular distance, as shown in Figure 40. The plot fits an exponential form with an estimated decay constant (β) of 0.5 $Å^{-1}$, *i.e.* 1.9 per phenyl ring. This result is in reasonable agreement with the values of ~1.8 and ~1.7 per phenyl ring measured in metal-molecule-metal junctions *via* scanning probe based techniques.[161,169,170] Extrapolating the plot fit (for R) to zero length we can further estimate the contact resistance

of the SWCNT/molecule/SWCNT junctions to be ~ 108 KΩ *i.e.* comparable to the contact resistance found for Au/molecule/Au junctions, ~360KΩ.[171] This value indicates that the molecule/SWCNT coupling is rather strong, as expected for amide bonds linkages, which possess a partial double bond character.

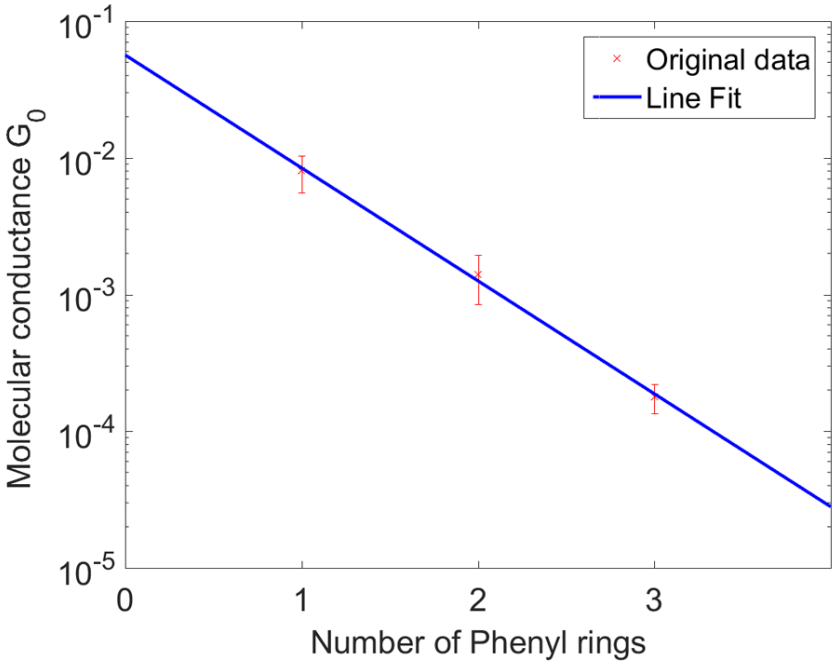

Figure 40. Measured conductances of oligophenyl SWCNT-based MTJs plotted against number of phenyl rings. Reprinted with permission from J Am Chem Soc. 2016;138(9):2905-2908. Copyright 2016 American Chemical Society.

3.7.2. Molecular Conductance of Benzidine and Terphenyl linked Molecular Junctions

As previously described, resistance values from inverse *I-V* traces were compiled into histograms from molecular junctions with benzidine and terphenyl junctions, as shown in Figures 41 and 42.

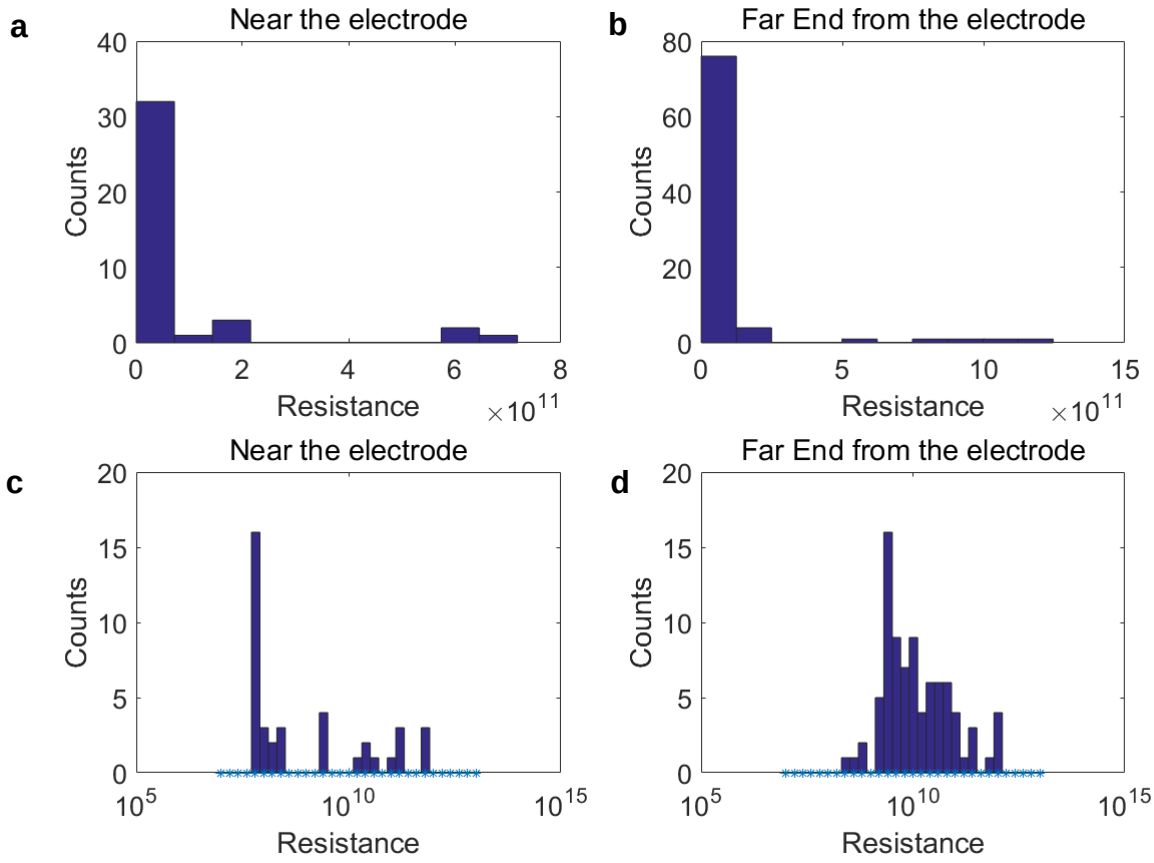

Figure 41. a) Resistance histogram of MTJs of benzidine near the macroscopic electrode. b) Resistance histogram of MTJs of Benzidine at the far end from the macroscopic electrode. c) Resistance histogram (log axes) of MTJs of Benzidine near the electrode. d) Resistance histogram (log axes) of MTJs of Benzidine at the far end from the electrode. Reprinted with permission from J Am Chem Soc. 2016;138(9):2905-2908. Copyright 2016 American Chemical Society.

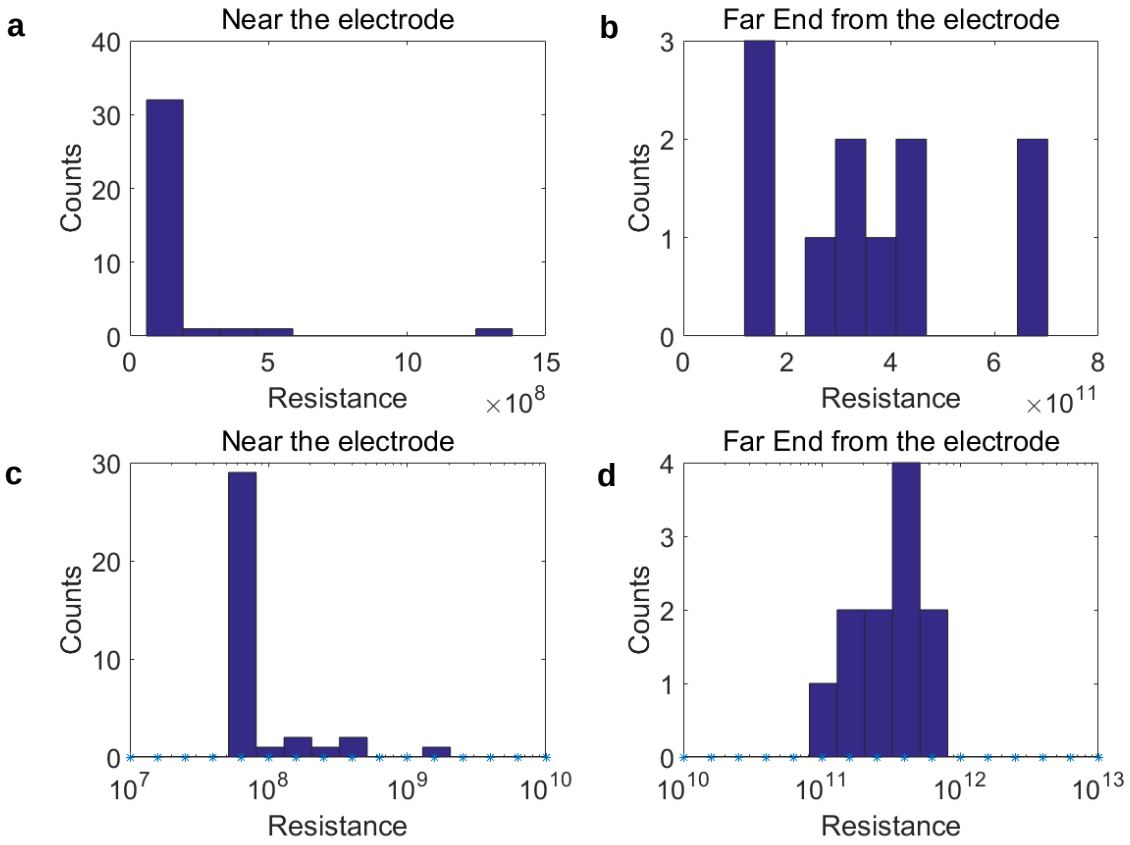

Figure 42. a) Resistance histogram of MTJs of Terphenyl near the macroscopic electrode. b) Resistance histogram of MTJs of Terphenyl at the far end from the electrode. c) Resistance histogram (log axes) of MTJs of Terphenyl near the electrode. d) Resistance histogram (log axes) of MTJs of Terphenyl at far end from the electrode. Reprinted with permission from J Am Chem Soc. 2016;138(9):2905-2908. Copyright 2016 American Chemical Society.

3.7.3. Molecular Conductance of Hexamethylenediamine linked Molecular Junctions

We performed an additional control experiment measuring the molecular resistance of SWCNT junctions formed with hexamethylenediamine (HMMD) as molecular linker, *i.e.* employing a non-conjugated molecule. AFM image and histogram were generated, as shown in Figure 43. The formation of molecular junction with HMMD linker was performed with the same double amidation reaction as shown with previous linkers. The resistance for HMMD-based MTJs was found to be $1.12 \times 10^8\ \Omega \pm 6.16 \times 10^7\ \Omega$. This value is in good agreement with the literature value of ~$10^8\ \Omega$ obtained for hexanethiol monolayers in nanoparticle bridges.[172]

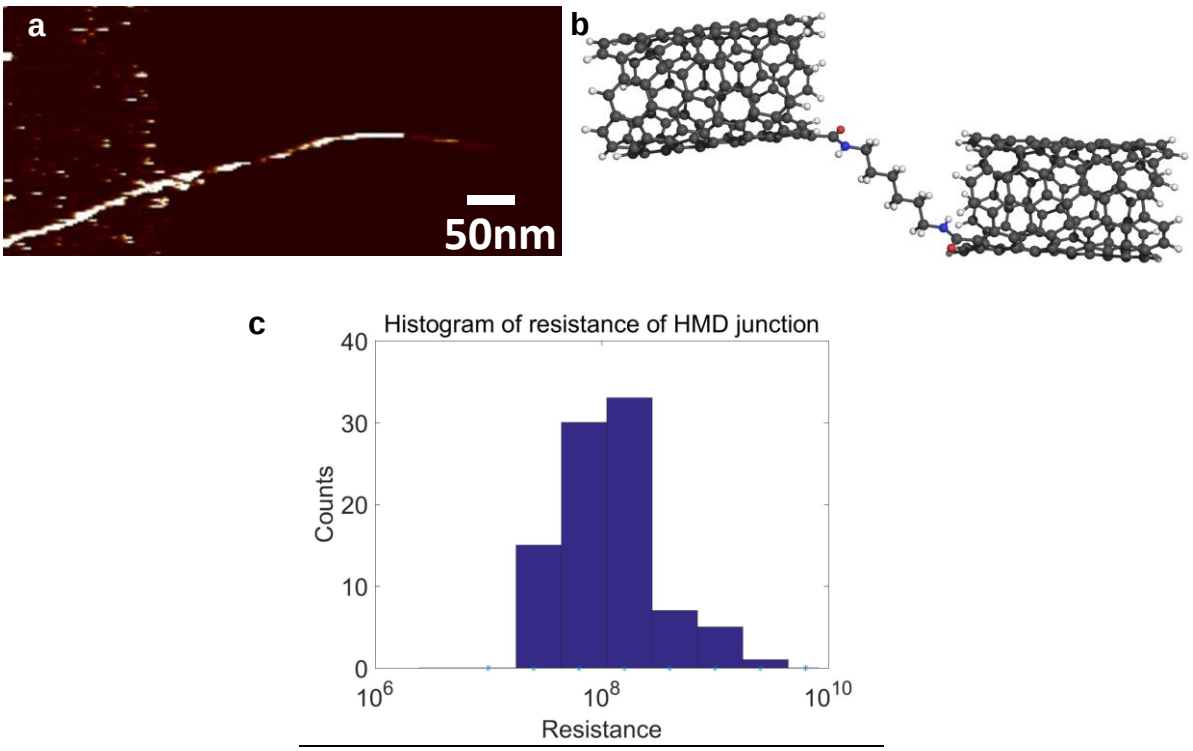

Figure 43. a) Representative C-AFM image of a MTJ formed using HMMD as the molecular linker, and interfaced to a macroscopic metal electrode. b) Schematic of HMMD linked MTJ. c) Resistance histogram of MTJs of HMMD at the far end from the electrode.

3.8. Concluding Remarks

Building upon the work by Palma *et al.* in 2013, the formation of molecular junctions *via* double amidation reactions with conjugated diamine on DNA-wrapped SWCNTs was successful: we demonstrated the ability to form these junctions with conjugated molecules. Overall increases in average tube length and increases in standard deviations with all linkers, except for control experiments, confirmed end-to-end connectivity of SWCNTs. Overcoming the initial challenge of solubility of oligophenyl linkers facilitated the junction formation, as it enabled a solution processable formation of junctions in a bottom-up methodology. Control experiments outlined that the specific reaction conditions must be met to obtain molecular junctions: no increase in average nanotube length heavily implies that no reaction had taken place.

Giving further validation to the double amidation reaction occurring, and thus the formation of molecular junctions, were the molecular conductivity results. The significant increase in resistance and significant decrease in conductivity confirmed the presence of a conjugated system between two nanotubes with metallic character. The increasing number of phenyl rings is also confirmed as Figure 36 clearly describes a trend with a decline in molecular conductance, which is expected and in line with literature values.[161]

PPD, benzidine and terphenyl linkers were the molecular junctions analysed *via* C-AFM to demonstrate an initial proof of concept, *i.e.* junction formation with conjugated diamines and conductivity measurements. Sequentially increasing the number of phenyl rings generates a trend in conductivity, which will be used in future experiments versus other molecular linkers (*e.g.* four phenyl ring systems, three-terminal junctions etc.).

The formation of molecular junctions with a conjugated linker that has been proven to be conductive, has significant implications for future generations of single molecule electronic

devices. It opens the possibility to “wire up” single molecules in a device configuration using a simple, environmentally friendly and inexpensive in-solution procedure. Following on from this area of research, it is important to next consider embedding SWCNTs into more relevant device configurations, *i.e.* an orientation that mimics a transistor. Current work in the Palma laboratory is focusing on the fabrication of solution-processable single-molecule transistors, taking advantage of the single-molecule knowledge developed in the study presented here.

4.0 Three-Terminal Molecular Junctions

4.1. Introduction

One of the ultimate goals in nanotechnology is the formation of single-molecule electronic devices. An important device in electronics is the transistor, which is ubiquitous across all modern integrated circuit systems. As discussed in chapter 1, Moore's Law outlines that the size of transistors in electronic circuits will reduce, while the number increases – this has led to the goal of a transistor operating at the single molecule level.[137,173] Originally patented in 1926 by Julius Lillenfeld, the field-effect transistor (FET) was envisioned but was not constructed until over twenty years later.[174] In 1947, American physicists invented the point-contact transistor and eventually won the Nobel Prize in physics.[175]

FET devices come in two forms: majority-charge-carrier devices or minority-charge-carrier devices, in which the current (charge) is carried predominantly due to a flow of either majority or minority carriers.[176] Charge carriers are either electrons or holes and an FET device consists of an active channel in which the charge carriers flow from the source to the drain. *Via* ohmic contacts, source and drain terminals are connected to the semiconductor. The conductivity of the channel is measured *via* the function of the potential applied across gate and source terminals.

FETs are made of three terminals:[176]

- Source – whereby charge carries enter the channel
- Drain – through which charge carriers leave the channel
- Gate – whereby the conductivity of the channel is modulated

By applying a voltage to the gate terminal, control of the current entering the drain is attained. A schematic of an FET device is shown in Figure 44.

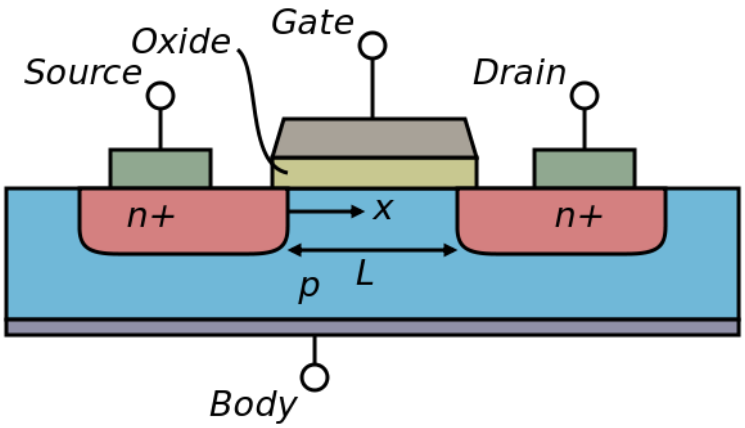

Figure 44. Cross-section of an n-type FET.

Utilising molecules as the active components of devices was proposed a number of years ago by Aviram and Ratner.[97] Since then, recent development has included molecular rectification demonstrated in 1993.[177] Additionally, benzene-1,4-dithiol rings were investigated as possible switching devices in molecular electronics, which exhibited highly reproducible current-voltage (*I*-*V*) characteristics.[86] In 1998, Dekker and co-workers reported transistor-like behaviour in carbon nanotubes.[20] Furthermore, Avouris and co-workers demonstrated similar devices using single and multi-walled carbon nanotubes.[178]

Theoretical calculations have shown single molecules can be used as the active channel in FETs.[95,179–184] However, challenges still remain in demonstrating a reliable three-terminal device, namely (a) bridging a single molecule to source and drain electrodes *via* an established methodology and (b) placing a gate electrode with a high degree of control (within a few nanometres) away from the molecule to achieve the required gate field.[185]

Attempting to overcome these challenges, efforts have included incorporating electrochemical gate electrodes or bottom-gate electrodes into molecular junctions.[185–192] However, the current through the molecule *via* the electrochemical gate can only be operated in electrolytes.[185–187] In this study, utilising amide bond formation techniques (previously defined in chapter 3) with

asymmetric tri-amine molecular linkers can drive the formation of three-terminal molecular junctions. This approach is designed to directly address both challenges outlined previously: to bridge source and drain electrodes *via* a single molecule and to establish a gate field.

Building on the work outlined in chapter 3, we can begin to consider the formation of a single-molecule device that mimics the structure of a typical transistor with a source, drain and gate. By employing the strategy outlined previously, a bottom-up, solution-based and processable technique can form a three-terminal structure *via* self-assembly. Figure 45 outlines the proposed configuration that is to be adopted in forming a three-terminal junction with CNTs employed as nanoelectrodes.

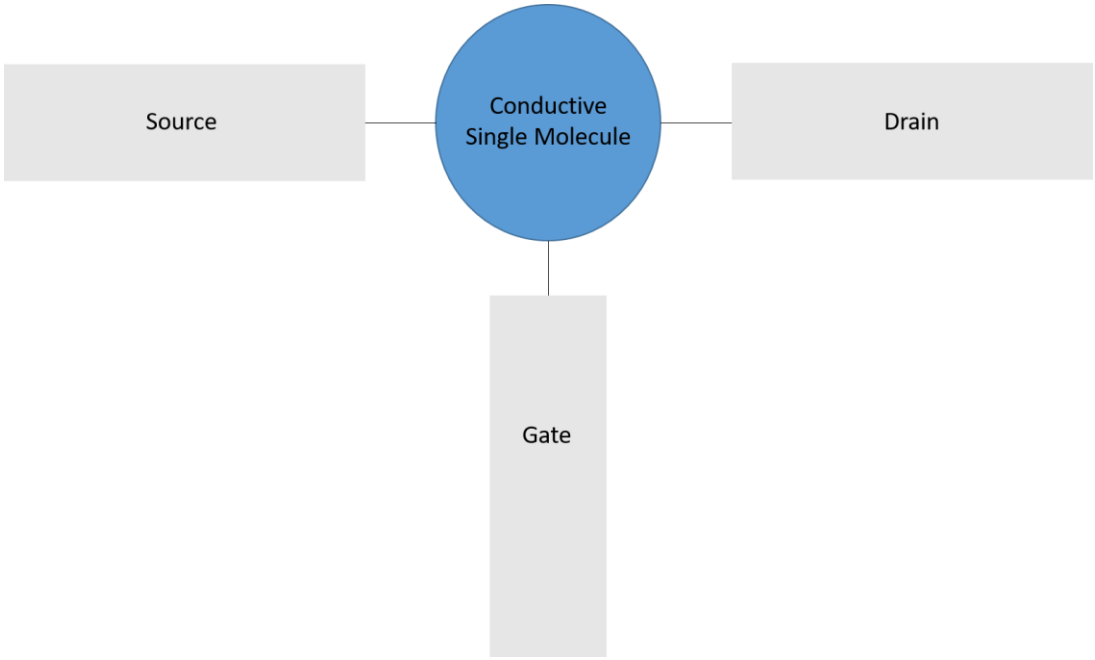

Figure 45. Schematic showing the proposed single-molecule device that mimics an FET configuration utilising CNTs (grey) as nanoelectrodes.

To achieve the structure proposed in Figure 45, a molecular linker must be designed that fulfils specific criteria. The device must carry a charge from source to drain terminals but can also modulate the conductivity of the channel *via* the gate terminal. The gate terminal can modulate conductivity *via* matching and mismatching molecule energy levels (work functions) versus

source and drain energy levels. By modifying the molecular linker *p*-phenylenediamine to include an alkyl chain and third amine group in the ortho position, as shown in Figure 46, there is an active carrier channel and a terminal that can modulate the channel conductivity. Applying a voltage to source terminal will produce an active channel to the drain terminal, however an application of voltage to the gate terminal will modulate the channel conductivity. The described configuration will demonstrate a similar application to that of an FET transistor as a proof of principle. In Figure 45, the pathway highlighted in red displays a conjugation while the pathway in blue does not. Therefore, the proposed model has two pathways: one that carries an electrical charge and another does not, thus mimicking the on/off response shown in a typical FET transistor.

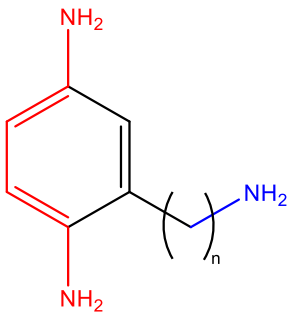

Figure 46. Proposed structure of asymmetric tri-amine molecular linker to mimic an FET device. Source terminal to drain terminal via active channel highlighted in red. Gate terminal to modulate conductivity highlighted in blue.

In chapter 3, it was outlined that forming molecular junctions with a PPD linker would facilitate an electrical current when a voltage is applied. A control experiment with HMMD linked SWCNT junctions demonstrated that a linker made of just an alkyl chain would not establish a current. By combining these two elements into a single molecule, it can be proposed to form molecular junctions with a linker that shows a dual functionality, *i.e.* a molecule that can establish an electrical current through a pair of nanoelectrodes with an insulating spacer *via* a

third terminal. The electrical current is facilitated *via* a conjugated system while the aliphatic alkyl chain displays non-conductive properties and acts as an insulating spacer.

4.2. Synthetic Pathway

The proposed structure is not commercially available and therefore should be synthesised to form molecular junctions. Therefore, it is important to select a synthetic pathway that efficiently forms the final product in sufficient yields. One synthetic pathway that was considered was the utilisation of copper azide-alkyne cycloaddition (CuAAC, or "click") chemistry, in which the final product is illustrated in Figure 47.

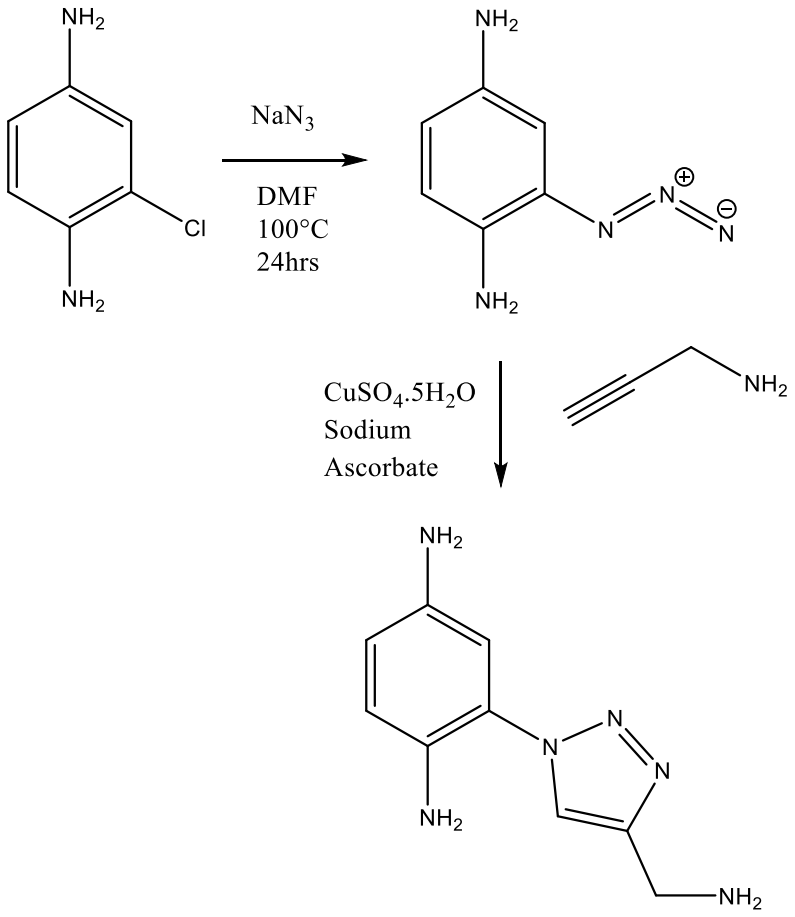

Figure 47. Proposed synthetic pathway of three terminal molecular linker *via* CuAAC.

CuAAC was chosen as part of the synthetic pathway as it well-known for producing end products in high yields, short reaction times and mild reaction conditions.[193] However, it was the initial azidation step that proved to be problematic. In a typical azidation reaction, bromine is utilised as a sufficient leaving group. The synthetic pathway proved problematic due to chlorine lacking the sufficient leaving group activity, possibly due to a lower electronegativity versus bromine. Therefore, it is proposed that any synthetic pathway must include a step that facilitates chlorine to be sufficient as a leaving group.

Considering previously failed attempts at synthesising the tri-amine molecular linker, it was then decided to perform a nucleophilic substitution directly upon the halogen. We found the Sonogashira reaction would cross-couple terminal alkynes with aryl halides with a palladium and copper catalysts and amine base, as shown in Figure 48.[194] The cross-coupling reaction was first derived in 1975 and is an extension of Heck reactions, which generates the same final products but under harsh conditions.[195] In 2010, Richard F. Heck, Ei-ichi Negishi and Akira Suzuki won the Nobel Prize in Chemistry for palladium-catalysed cross couplings in organic synthesis. Both Heck and Sonogashira reactions utilise palladium catalysts, however the latter uses both palladium and copper catalysts simultaneously. This enables the reaction to be carried out at room temperature as reagents experience an increase in reactivity.[195,196]

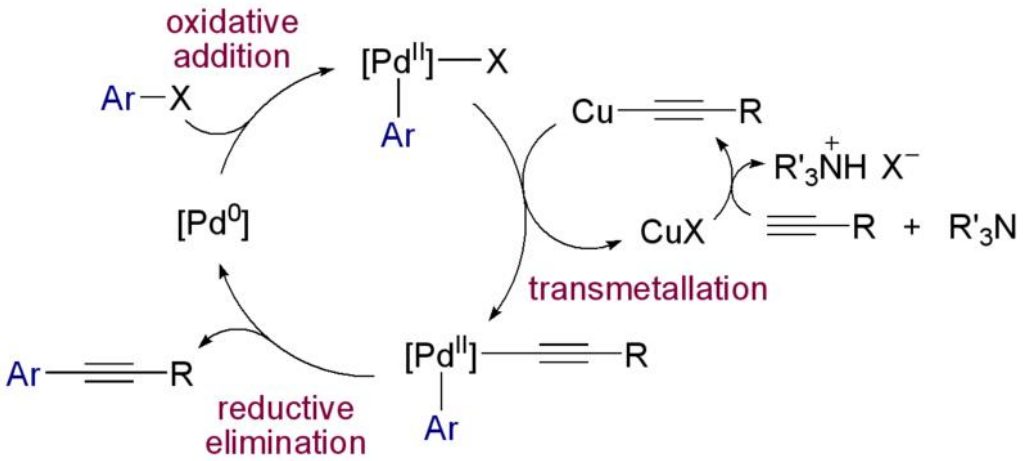

Figure 48. Schematic of Pd-catalysed Sonogashira cross-coupling with Cu co-catalyst. Reprinted with permission from Wikimedia Commons (2006). Copyright 2006 Wikimedia Commons.

Cross-coupling has been employed in a wide range of areas due to the reliability and broad scope of substrates that can be utilised. Reactions can be carried out under mild conditions and has applications that include pharmaceuticals, natural products, organic materials and nanomaterials.[194] Specific examples include the synthesis of drugs used as treatments for psoriasis, Alzheimer's disease and Parkinson's disease.[197,198]

The reaction is performed under mild conditions, however hydrogen halide by-products form because of the coupling reaction, therefore triethylamine is often used as a solvent. DMF and ethers can also be used as a solvent and other bases (including potassium carbonate) are occasionally used. It is also worth noting that the reaction conditions have varying results depending on the sp^2-carbon halide as shown in Figure 49. This has important implications as it suggests that the reaction scheme being proposed could be improved upon if a bromine aryl halide is used instead of a chloro halide.

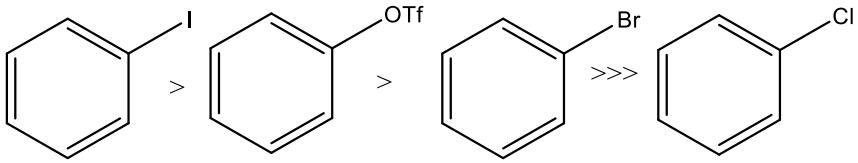

Figure 49. Reaction rates according to sp2-carbon halides in Sonogashira Cross-Couplings.

Aryl iodides and bromides are both excellent coupling partners with terminal alkynes in a Sonogashira cross-coupling.[199–205] However, it is more challenging to utilise aryl chlorides in cross-couplings, which are often more practical and accessible as starting materials. In a typical Sonogashira cross-coupling, Cu(I) co-catalyst is used for efficient coupling. However, if Cu(I) oxidises to Cu(II), the copper salt can also facilitate the homo-coupling (Glaser-type coupling) of terminal alkynes as a side reaction, which has led to considerable effort directed to the development of effective copper-free processes.[206–208] Furthermore, reducing catalyst loading and the recycling of palladium metal are also important implications in this area of study.

Therefore, a Sonogashira cross-coupling that utilises aryl chlorides under copper-free conditions with reduced loading of palladium catalyst would mean efficient synthesis of an ideal compound for a tri-amine molecular linker. One procedure, outlined by Anna Komaromi, utilises a range of palladium catalysts in a copper-free Sonogashira cross-coupling that will be utilised in this study.[209]

The 2008 study shows $Pd(dba)_3$ generating a yield of 85% and is relatively affordable and easily accessible.[209] A range of ligands were also explored, in which XPhos was highlighted as the most effective.[209] Additionally, K_2CO_3 was outlined as the most sufficient base.[209] Each of these reagents was employed in the overall synthesis of tri-amine molecular linkers. Before proceeding with the Sonogashira cross-coupling, it is important to establish protecting groups on all amines, as amino groups have shown to co-ordinate to palladium catalysts and would, therefore, disrupt the cross-coupling.[210] Thus it is important to protect all amine groups with tert-Butyloxycarbonyl (Boc) protecting groups before conducting the copper-free cross-coupling. The overall synthetic pathway is outlined in Figure 50.

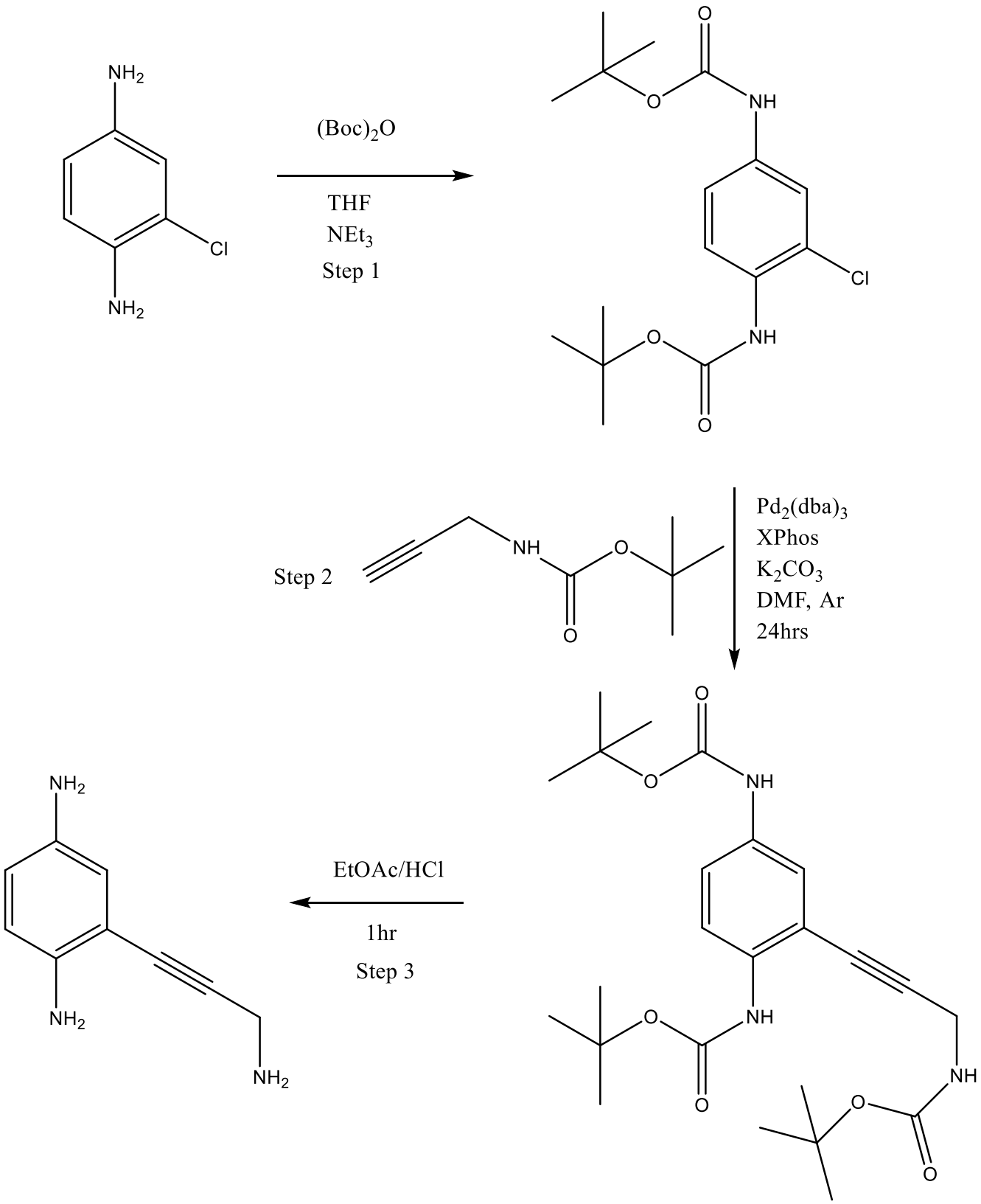

Figure 50. Proposed synthetic pathway of an asymmetric, tri-amine molecular linker.

The first step in the proposed synthesis was to Boc protect both amine groups using a well-established methodology. The product was characterised with NMR, IR and mass spec.

4.2.1. Boc Protection of 2-chlorobenzene-1,4-diamine

Modifying the standard Boc protection synthesis by doubling di-tert-butyl dicarbonate equivalence to perform a double amine protection step is shown in Step 1 (Figure 50).

Addition of two Boc protection groups was clearly observed in the NMR spectra when comparing the starting material to the final product, as shown in Figure 51.

NMR of 2-chlorobenzene-1,4-diamine displays two distinct regions that reflects the number of proton environments. Protons within the aromatic region are found in the spectra between 6.50 – 6.75 ppm and protons within amine functional groups were located on the NMR spectra between 3.25 – 3.75 ppm. The spectra of Boc-protected starting material show amine protons shifted toward the aromatic region and an integration of one, compared to an integration of two in the starting material. The NMR spectrum also displays a strong peak at ~1.50 ppm that displayed a higher integration due to the presence of two Boc protection groups – these elements suggest that Boc protection had been successful.

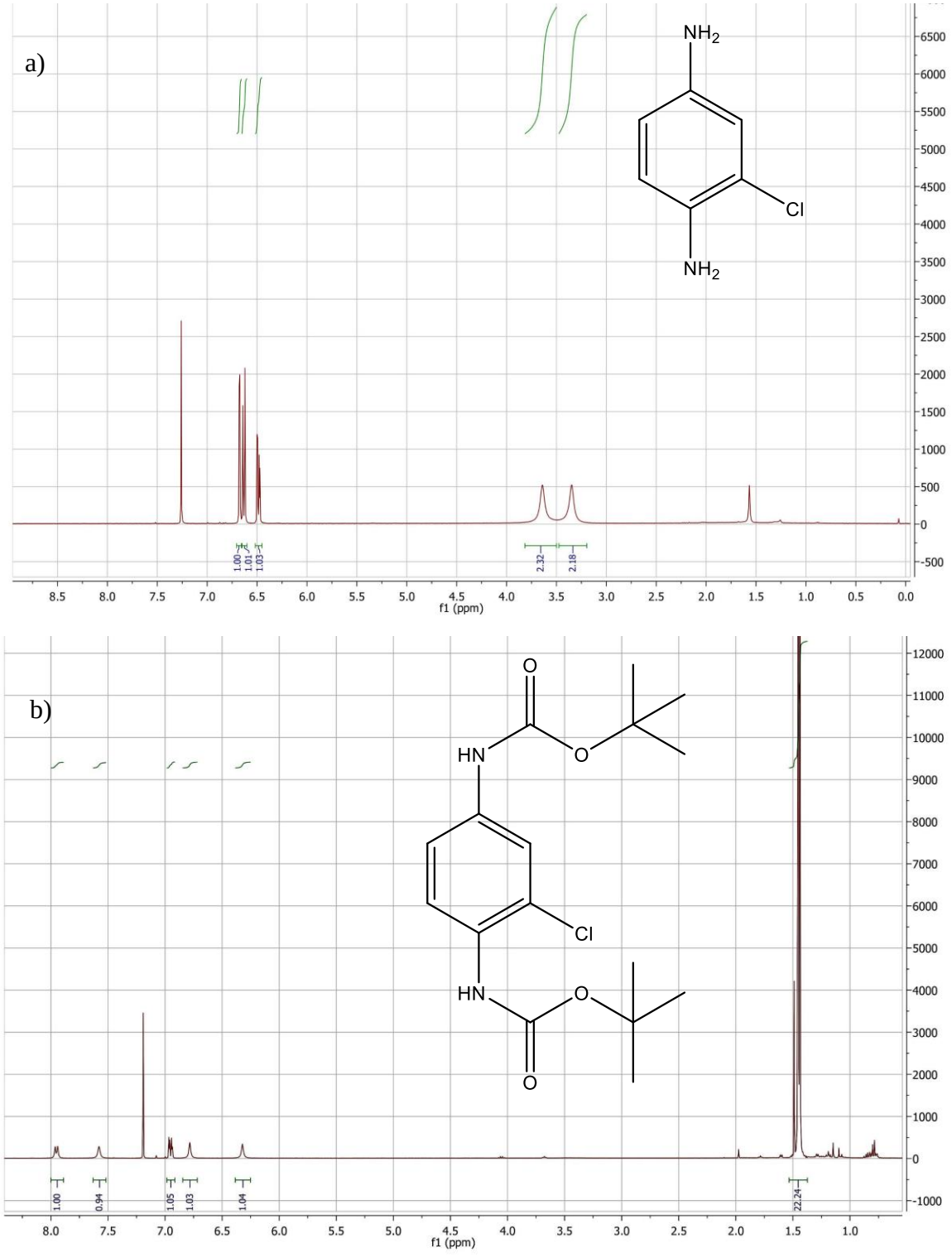

Figure 51. NMR spectra of a) 2-chlorobenzene-1,4-diamine and b) Boc-protected 2-chlorobenzene-1,4-diamine.

4.2.2. Pd-catalysed Sonogashira coupling

As shown in Step 2, the proposed synthetic pathway outlines that following a double Boc protection of the starting material, Pd-catalysed, copper-free Sonogashira coupling was performed utilising commercially available Boc-protected propagylamine. NMR spectra of Boc-protected propagylamine indicates aliphatic protons that are distinct from the aromatic and amine protons found in the starting material.

The final product will incorporate signals form aliphatic protons as well as a third Boc functional group. Both NMR spectra of Boc-protected propagylamine and Sonogashira coupling product are shown in Figure 52.

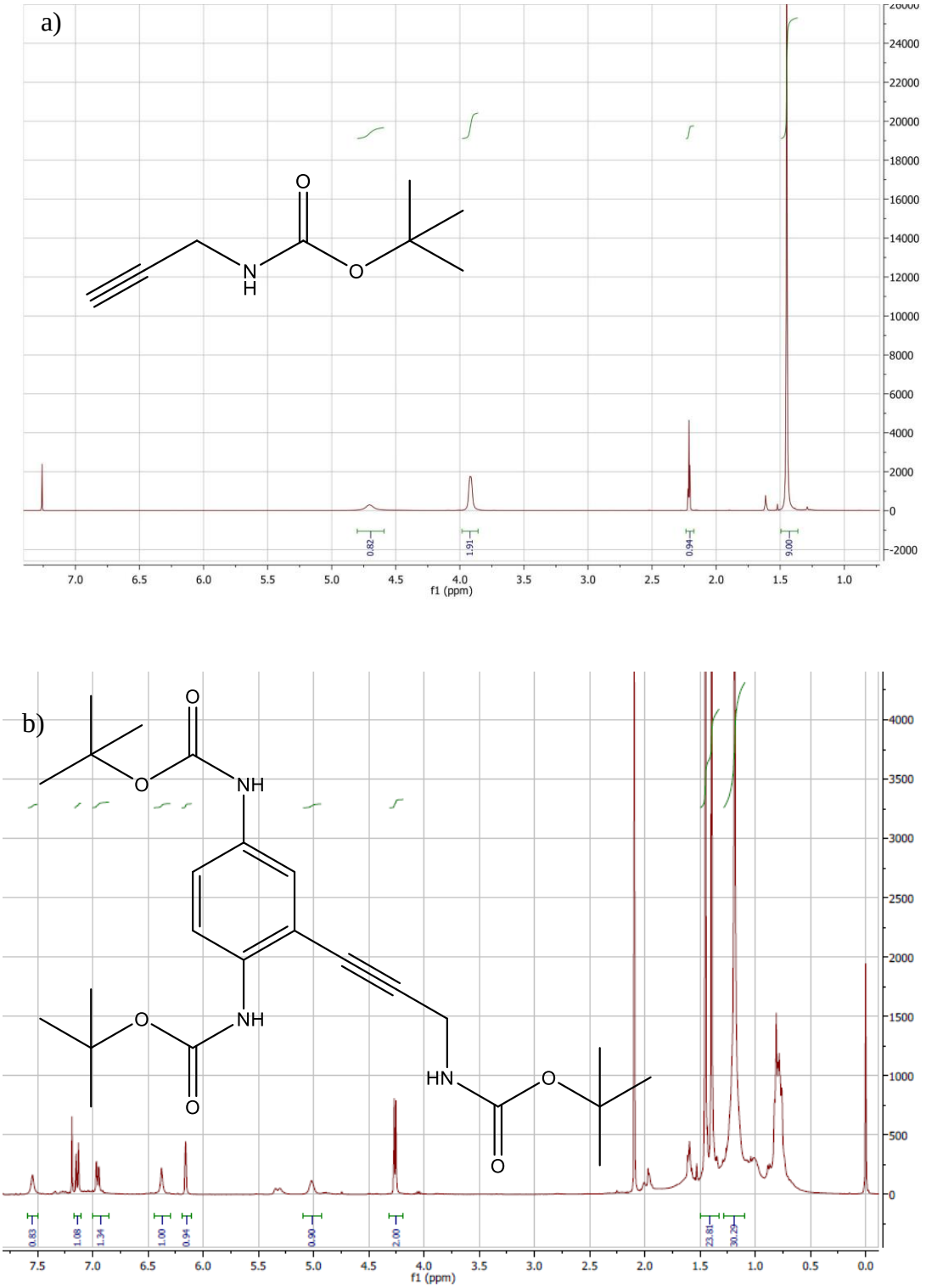

Figure 52. NMR spectra of a) Boc-protected propagylamine and b) di-tert-butyl (2-(3-((tert-butoxycarbonyl)amino)prop-1-yn-1-yl)-1,4-phenylene)dicarbamate

Boc-protected propagylamine displays four distinct proton environments that are clearly observed in the NMR spectra, as shown in Figure 52 a). The strong peak at 1.50 ppm, which is also observed in other Boc-protected structures, is present due to the Boc protection group. A singlet peak observed at 4.75 ppm is typical of an amine proton and a singlet with an integration of 1.98 at 3.80 ppm is due to the aliphatic protons. Furthermore, the sharp peak at 2.25 ppm with an integration of 0.94 is due to the presence of the terminal alkyne proton.

Following the Pd-catalysed Sonogashira coupling, the NMR, as shown in Figure 52 b), displays the peaks shown in the spectra of Boc-protected 2-chlorobenzene-1,4-diamine but also the peaks observed in the spectra of Boc-protected propagylamine with one noticeable exception. Sonogashira couplings will result in a new C-C bond formation with a terminal alkyne that substitutes the terminal proton. Therefore, Sonogashira products will not have a signal from the terminal alkyne proton in the NMR spectra. The sharp peak observed at 2.25 ppm in the Boc-protected propagylamine is not present in the NMR spectra following the Sonogashira coupling, this indicates the formation of a new C-C bond formed between alkyne and aromatic species. The sharp peak at 2.15 ppm is due to excess toluene solvent within the product that was difficult to remove.

4.2.3. Boc-Deprotection

The final step (Step 3) in the synthetic pathway is the Boc deprotection. Utilising typical deprotection conditions with hydrochloric acid, the final NMR spectra, shown in Figure 53, outlines the loss of Boc protection groups and amine protons with integrations of ~2. Other signals in the NMR spectra can be accounted by the presence of residual solvent.

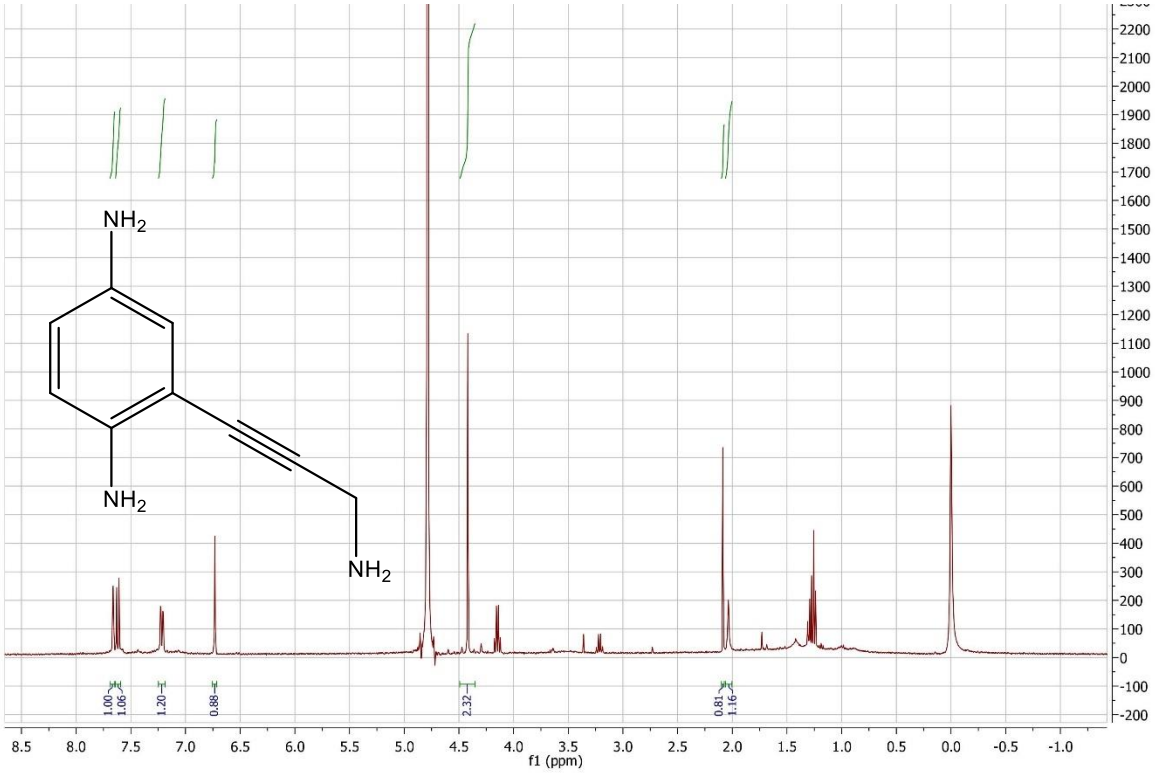

Figure 53. NMR spectra of 2-(3-aminoprop-1-yn-1-yl)benzene-1,4-diamine – tri-amine molecular linker.

Figure 54 shows the COSY spectra displaying coupling between aromatic protons, which is expected. It also shows that protons from amine groups will not couple with any other protons and aliphatic protons couple with impurities but only in relatively low amounts.

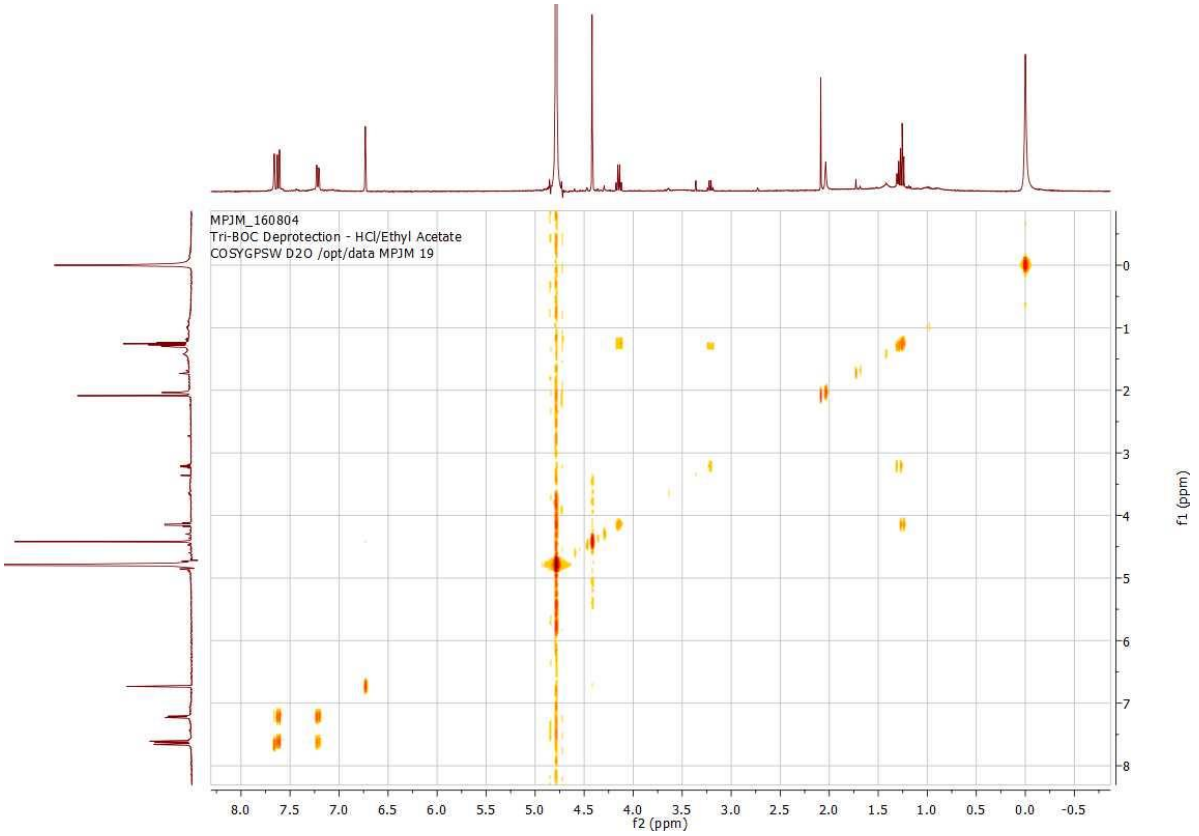

Figure 54. COSY spectra of 2-(3-aminoprop-1-yn-1-yl)benzene-1,4-diamine – tri-amine molecular linker.

At all points in the synthetic pathway each individual reaction was justified *via* proton NMR characterisation. Therefore, it is reasonable to have confidence that the proposed synthetic pathway proposed was a successful one and the final product of a tri-amine molecular linker was formed. Further characterisations of infrared (IR) spectroscopy, melting point analysis and mass spectrometry were performed at each step to confirm each product was formed.

Confirming the synthesis of the tri-amine, the molecular linker was utilised to form molecular junctions in the same methodology outlined in chapter 3. Crucially, with three amine groups

available, the purpose of this linker is to form molecular junctions that terminally connect three SWCNTs, mimicking the structure of a single FET.

Despite forming molecular junctions in the same manner, assessing the junctions was done in a different way, *i.e.* Y-shaped configurations will be analysed. Y-shape configurations give a clear indication of the formation of a three-terminal molecular junction. Height profiles of tubes were also measured to ensure Y-shape configurations were not a result of overlapping nanotubes but from junction formation. Two-terminal molecular linkers (outlined in chapter 3) will be used to provide a control in Y-shape configuration measurement, *i.e.* how does the number of Y-shape configurations with three-terminal linkers compare to two-terminal linkers.

4.3 Results

Utilising the established methodologies explained in chapter 3, tri-amine molecular linkers were employed to link SWCNTs end-to-end into Y-shape configurations. Solutions were cast onto surfaces and imaged *via* AFM. Differently to 1-dimensional assemblies, three-terminal junctions would be indicated with Y-shape configurations. Figure 55 shows a representative AFM image of a surface with a schematic of SWCNT-tri-amine assembly. Additionally, nanotube lengths were measured to compare versus pristine nanotubes – each branch of Y-shaped configurations were measured to ensure junction formation had occurred for each amine functional group.

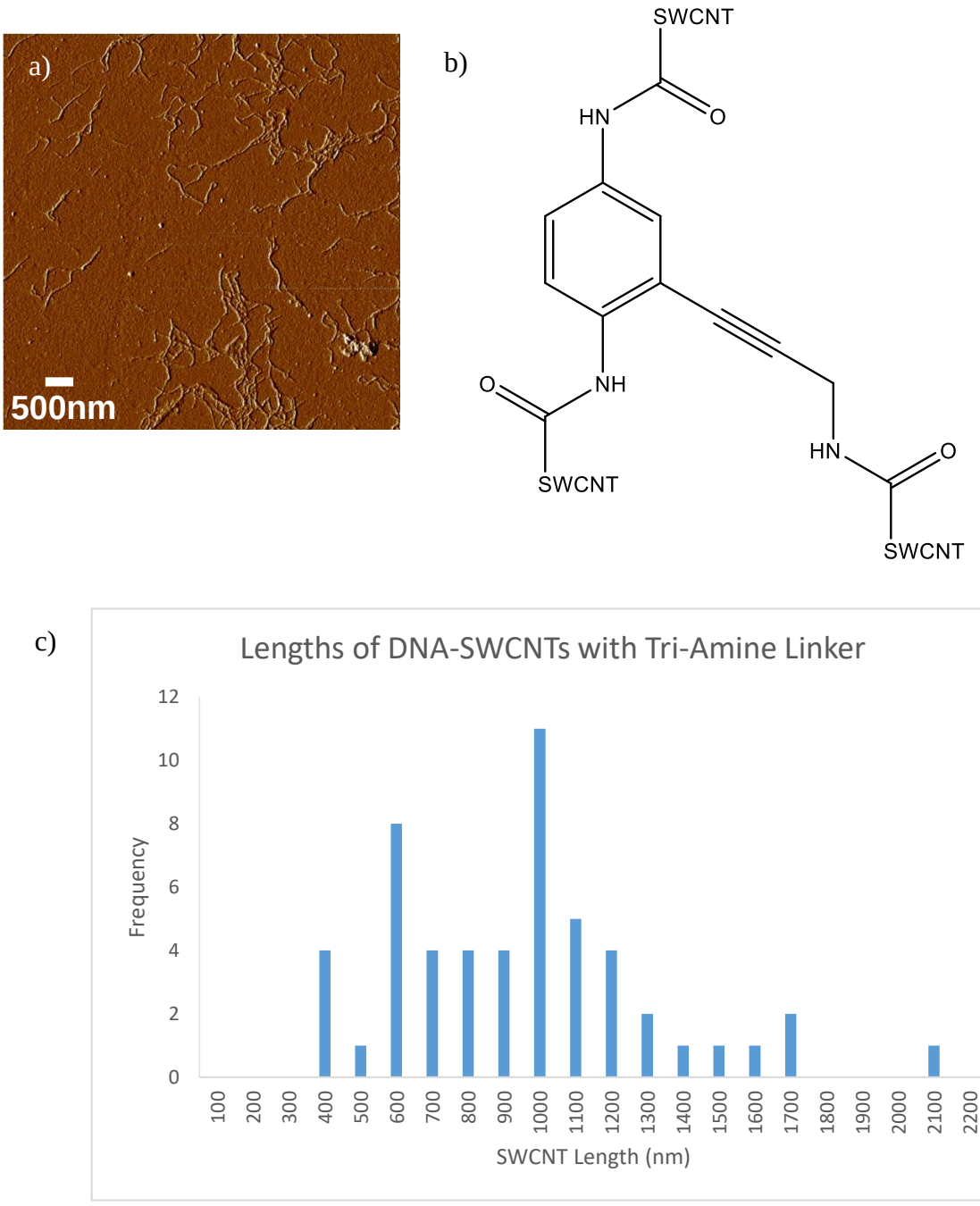

Figure 55.a) AFM image of Y-shape configuration from three SWCNTs and tri-amine molecular linker. b) Structure of molecular junction with tri-amine molecular junction. c) Histogram of metallic DNA-wrapped SWCNTs measured. Average tube length: 897.78 ± 359 nm.

AFM images show nanotubes to be significant longer than pristine SWCNTs. An overall increased average tube length and increased standard deviation indicate that molecular junctions were formed successfully. Focusing on a single junction, a Y-shape configuration is clearly observed as shown in Figure 56.

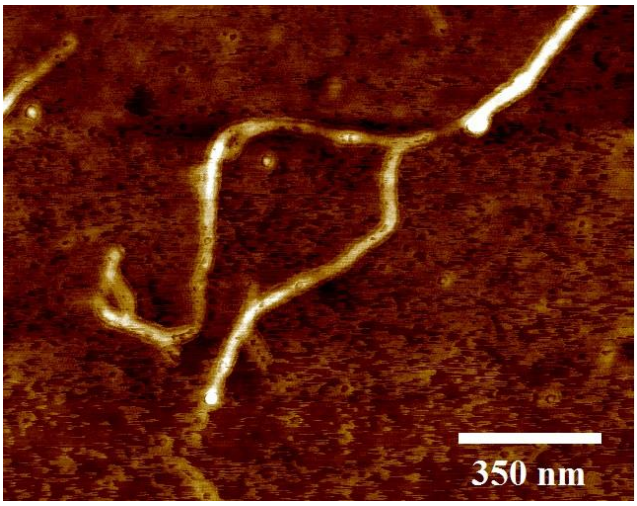

Figure 56. Zoomed-in AFM image of tri-amine (three terminal) linked molecular junction.

To confirm three-terminal junction formation, height profiles can prove nanotubes are connected end-to-end rather than overlapping. Utilising NanoScope Analysis software, cross-sections were drawn at various points along the Y-shape molecular junction to measure the height of the nanotube, as shown in Figure 57. Heights were calculated with the same equation used in chapter 3 to calculate nanotube heights.

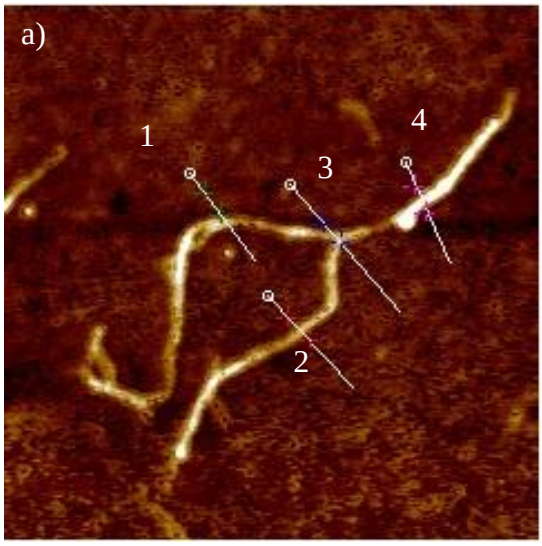

b)

Cross Section	Height (nm)
1	**4.63**
2	**4.84**
3	**4.65**
4	**4.70**

Figure 57. a) AFM image of Y-Shape configuration form tri-amine linked molecular junction with cross-section areas labelled 1-4. b) Table of heights measured at each cross-section.

All heights measured at each cross-section are within tolerance of one another. Cross-section 3 would be the area where overlapping would be observed and would therefore expect heights of ~8 nm or greater. However, it is shown that heights are not significantly different to that heights measured at other cross-sections and to the heights calculated in chapter 3. It is also worth noting that the distance between two adjacent nanotubes (i.e. cross section points 1 and 2) is approximately 350nm. The number of Y-shaped junctions were compared with the number of linear junctions of tri-amine linked nanotubes and PPD-linked nanotubes as shown in Table 6. In both examples, DNA-SWCNTs with metallic character were utilised.

Molecular Linker	% of Linear Junctions	% of Y-Shaped Junctions	Total No. of Molecular Junctions
PPD	93.7%	6.4%	63
Tri-Amine	77.4%	22.6%	53

Table 6. Y-Shaped configurations and linear junction comparison with PPD and Tri-Amine molecular linkers.

PPD molecular linker displays 6.4% Y-shaped junctions, suggesting the level of error approximately 6%. However, further investigation and is required to confirm this value as other factors must be identified.

Y-shaped configurations observed in PPD-linked molecular junctions could be due to two PPD linkers forming amide bonds on the same nanotube end. As shown by the work of Dr. Rachel Crespo-Otero in section 3.4, junctions with two molecule systems, are thermodynamically unfavourable, therefore it is reasonable to assume that these molecular junctions predominantly form with single molecules, *i.e.* Y-shape configurations are predominantly formed with single tri-amine molecules and not two molecule systems, which would be energetically unfavourable.[134] However, the number of Y-shaped configurations observed with tri-amine linkers display a significant increase over PPD linkers. When taking into consideration the increase in average nanotube length and standard deviation, the height profiles of Y-shaped configurations and the significant increase in the number of three-terminal junctions, it is therefore reasonable to suggest that a tri-amine molecular linker forms three-terminal molecular junctions with a single molecule only. The nature of the linker employed facilitates the formation of a nanotube-based structure that mimics the structure of an FET device, the next step is to analyse if the device performs in a similar manner electrically.

4.4. Future Work of Tri-Amine Linkers

One of the key areas that needs to be conducted from this area of study is to establish a methodology for the confirmation of three-way junctions in Y-shape configurations. It is possible for two molecular linkers to attach in the terminal positions that would display Y-shape orientations. It could be useful, therefore, to utilise DFT calculations with Y-shape configurations to understand the thermodynamically favourable orientations. Subsequently, future work will focus on measuring the conductivity of the tri-amine linker and observe if the device can mimic the performance of an FET, *i.e.* sweep the gate to align energy levels. It is also worth developing other linkers with an increased number of alkyl groups in insulating segment of the linker – an increase in carbon chain length could increase the likelihood of amide bond formation with SWCNTs and thus increase the yield of molecular junctions.

4.5. Porphyrin Ring Molecular Linkers

One possible reason why the yield of Y-shaped junctions is not higher than 22% (as shown in the previous section), is that steric hindrance from SWCNTs may reduce the amount of amide bond formation. Therefore, increasing the size of the molecular linker may improve the possibility of three-terminal junction formations. One way to increase the size of the linker would be to increase alkyl groups as previously mentioned; another alternative is to employ porphyrin linkers that have the possibility of further modification.

Porphyrin rings have the potential to be modified with four amine groups to link with SWCNTs. This facilitates the formation of four SWCNTs connecting terminally to a single molecule. Forming a molecular junction with four SWCNTs connected terminally can allow a diverse range of electrical devices due to the variety of modifications available to porphyrin rings. In this study, three porphyrin rings, as shown in Figure 58, will be employed as molecular linkers in the same manner as linkers in chapter 3. Linear molecular junctions will be expected

to form, as will Y-shape configurations and possibly X-shape (four-way connectivity) configurations. Steric hindrance will play a crucial role in this reaction as the majority of junctions formed will be linear as it is most energetically favourable.

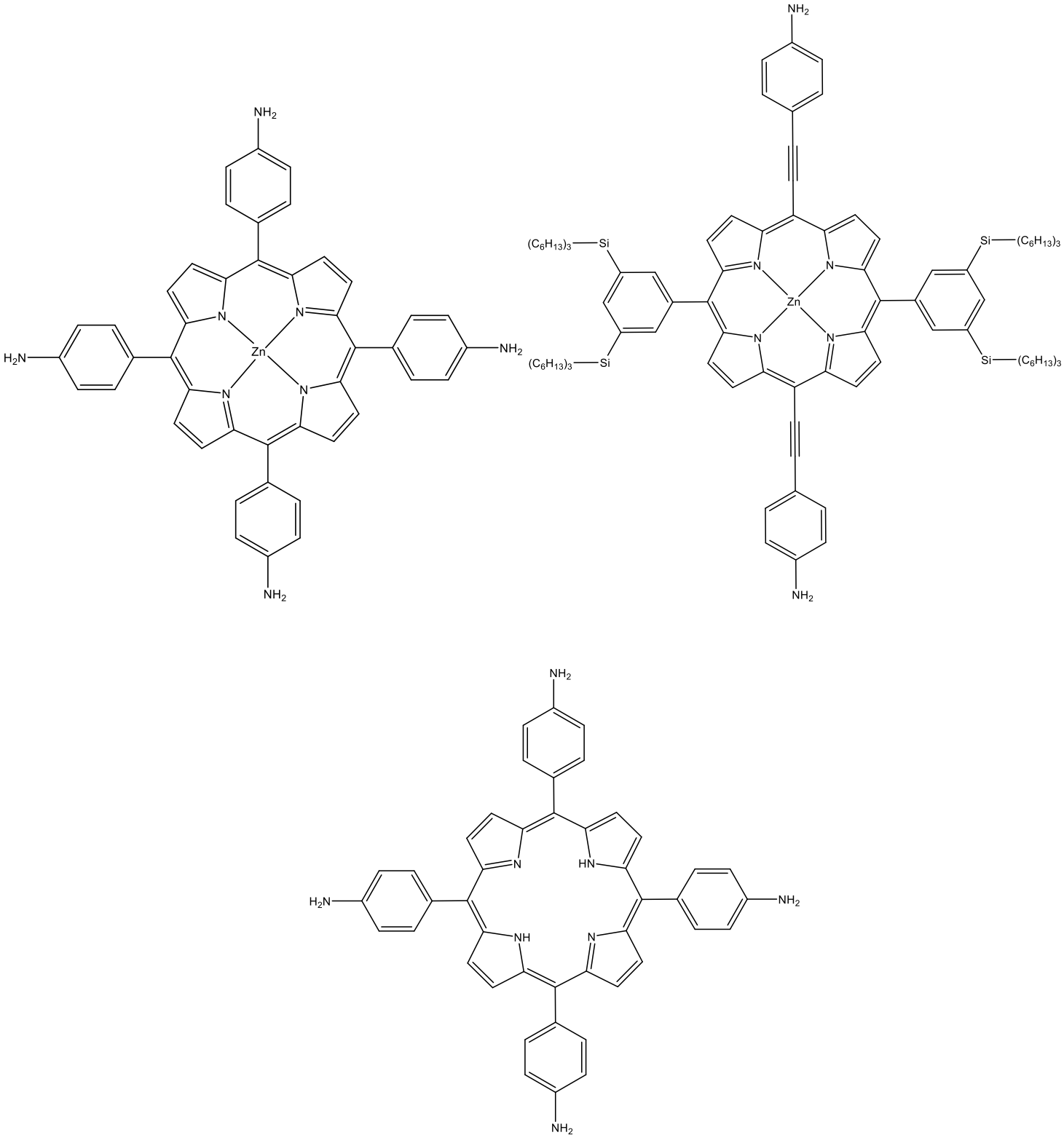

Figure 58. a) Structure of Porphyrin Ring 1 with two amine functional groups to produce linear molecular junctions. Structures b) and c) are Porphyrin Ring 2 and 3, respectively, which have four amine functional groups to produce linear, Y-shape and X-shape junctions.

Nanotubes were measured to determine whether molecular junctions were formed. Once molecular junctions were confirmed then Y-shape and X-shape configurations were counted and a yield calculated. This process was performed for each porphyrin ring and results, shown in Figure 59, 60 and 61 outline average tube lengths with standard deviations, yields of Y-shape and X-shape configurations.

a)

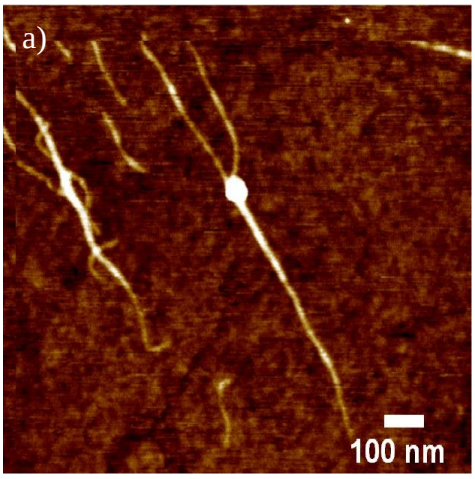

b)

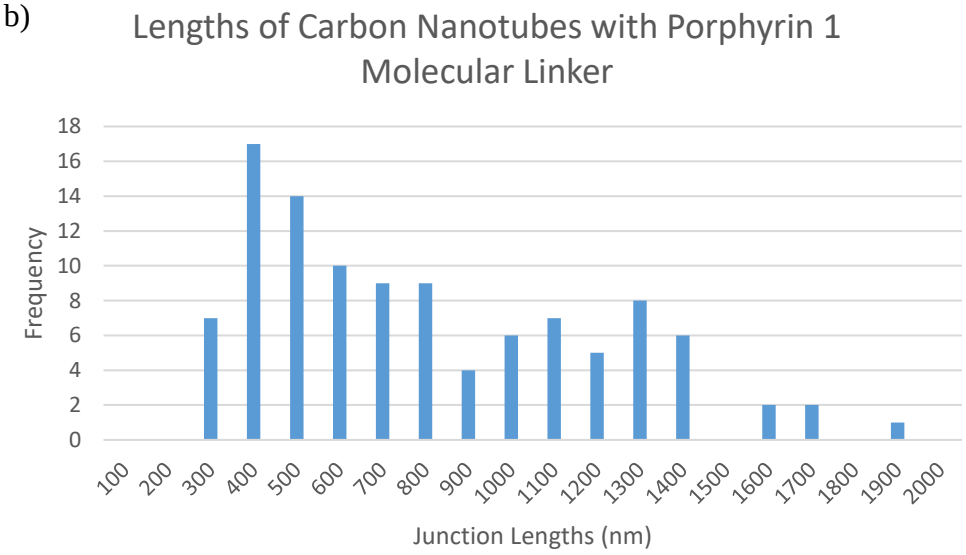

c)

Porphyrin Ring 1	
Average Nanotube Length (nm)	881 ± 419.8
Y-Shape Configurations (%)	0.9
X-Shape Configurations (%)	0

Figure 59. Statistical results of Porphyrin Ring 1 linked molecular junctions. a) Zoomed-in AFM image of linear molecular junctions. b) Histogram of nanotube lengths measured. Average molecular length 881 ± 419.8 nm. c) Table of statistical data.

Porphyrin Ring 1 has two amine functional groups that create linear junctions. Therefore, it is expected that no X-shape and very few Y-shape configurations are observed. Nanotube length was measured at an increased average (from 473 nm) and confirmed to have formed molecular junctions – the overwhelming majority of which are linear.

a)

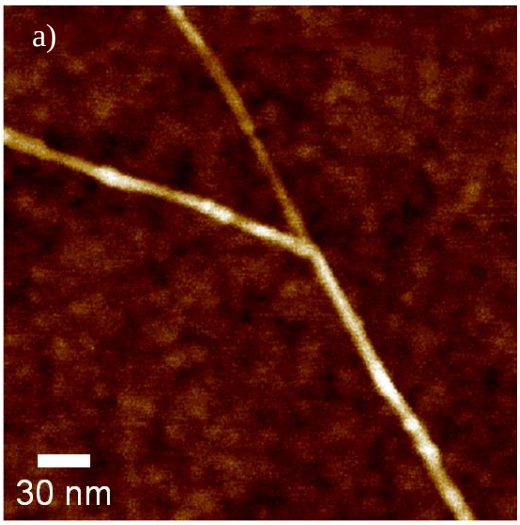

b)

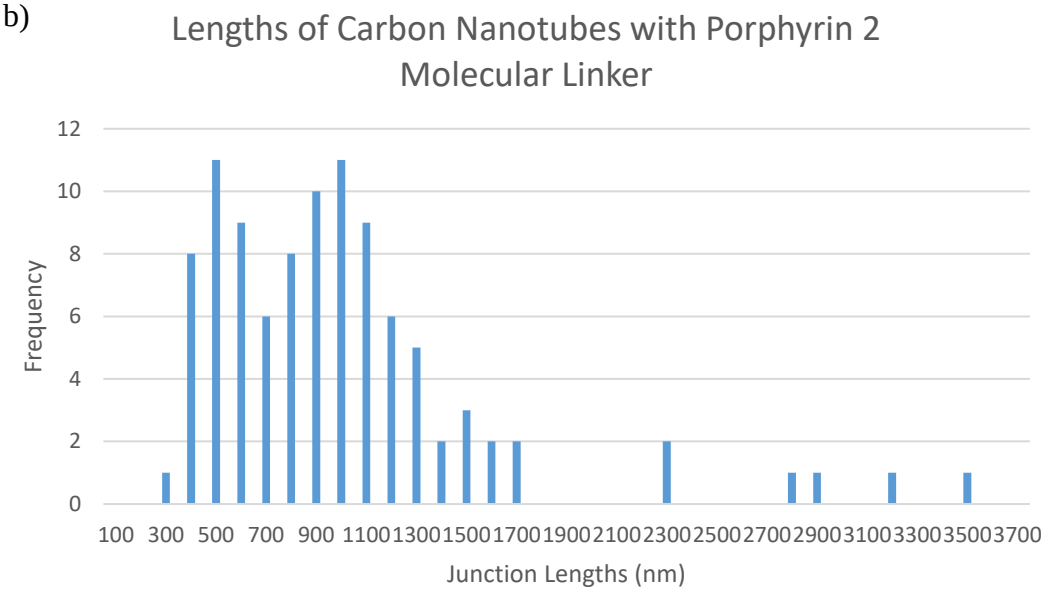

c)

Porphyrin Ring 2	
Average Nanotube Length (nm)	950.8 ± 579.5
Y-Shape Configurations (%)	22.4
X-Shape Configurations (%)	0

Figure 60. Statistical results of Porphyrin Ring 2 linked molecular junctions. a) Zoomed-in AFM image of Y-shape molecular junction. b) Histogram of nanotube lengths measured. Average molecular length 950.8 ± 579.5 nm. c) Table of statistical data.

The increased average nanotube length confirms molecular junction formation with Porphyrin Ring 2 linker. Y-shape configurations are also observed at a similar level to tri-amine molecular linkers. No X-shape configurations are observed, which suggests steric hindrance is preventing the formation of four-terminal junctions.

a)

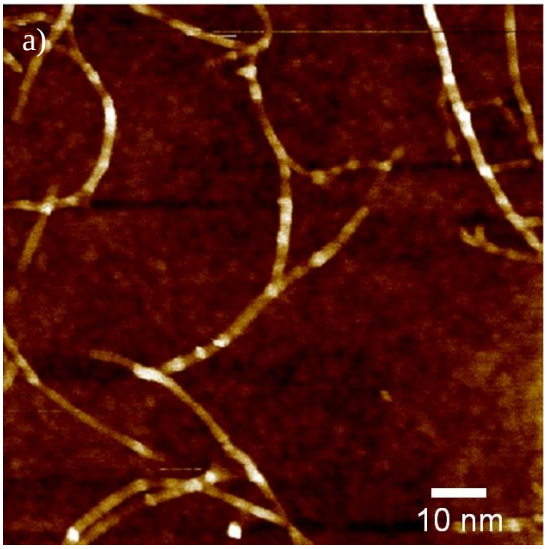

b)

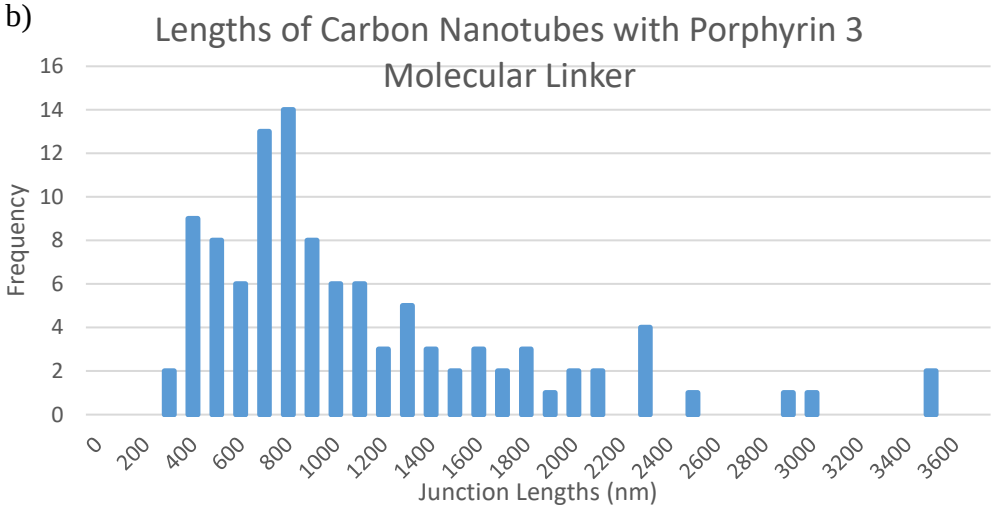

c)

Porphyrin Ring 3	
Average Nanotube Length (nm)	1048.5 ± 672.6
Y-Shape Configurations (%)	25.5
X-Shape Configurations (%)	0

Figure 61. Statistical results of Porphyrin Ring 3 linked molecular junctions. a) Zoomed-in AFM image of Y-shape molecular junction. b) Histogram of nanotube lengths measured. Average molecular length 1048.5 ± 672.6 nm. c) Table of statistical data

Porphyrin Ring 3 shows strong similarities to Porphyrin Ring 2 – suggesting the central zinc cation will not change the performance of the molecular linker. Molecular junctions are confirmed with increased average nanotube length and Y-shape configurations are observed at a satisfactory level. Again, no X-shaped junctions are shown, further increasing the hypothesis that three-terminal junctions are the maximum number per steric hindrance limitations.

4.6. Concluding Remarks

In this area of study, we have investigated the use of three-terminal asymmetric and porphyrin ring linkers to form single-molecule junctions. Formation of three terminal systems opens the possibility of forming CNT-based electrical devices that can mimic the function of transistors. Characterisation of each step of the tri-amine molecular linker has confirmed the structure of each product of the synthetic pathway and thus confirms the tri-amine product. Utilising the tri-amine molecular linker to form junctions with SWCNTs facilitated the formation of three-terminal junctions. AFM analysis of the Y-shaped configurations confirms SWCNTs are connected terminally – structures that are predominantly more abundant with tri-amine linkers than with linkers with two amine functional groups. Tri-amine linkers have shown Y-shape configurations but the next step would be to improve this yield and break past the 25% mark. The synthetic pathway outlined, also facilitates the employment of terminal alkynes with larger alkyl chains to improve insulating properties – one future area of research could investigate the impact of increasing carbon length on the electrical properties of the device. It is also worth investigating other tri-amines with different properties, as the properties of molecular linkers are fundamental to the properties of the transistor device.

Further work into the field of multiple terminal junctions was investigated with a group of three porphyrin rings, which drove the hypothesis that three-terminal junctions is the maximum number when implementing SWCNTs terminally. Utilising four-terminal linkers opens the

possibility for more elaborate electrical devices as there is wide-reaching potential to functionalise porphyrin rings. Similarly, for tri-amine linked SWCNTs, C-AFM would be an effective technique when analysing the electrical properties of a single porphyrin ring molecule.

Building three-terminal molecular junctions enables the mimicry of an FET device, in a single-molecule system. In order to observe device performance, in the future, C-AFM should be used to measure the conductivity of the single molecule in the same way described in chapter 3. This technique would also assess the on/off properties of the three-terminal junction, which is present in FET devices. This work has highlighted that molecular junction formation is only the beginning and utilising more complex single molecules can open new pathways in the fabrication of nanotube-based single-molecule devices.

Molecular junction formation with asymmetric tri-amines and porphyrin rings, have both stemmed from the work outlined in chapter 3. This chapter has described how versatile the amide formation reaction truly is. Modifying molecular linkers has led to stark changes in the overall structure of molecular junctions. Following the same logic, it could be suggested that by making modifications to the DNA wrapping the SWCNTs then molecular junctions would also form new structures. Utilising the versatility of DNA sequences, one could modify side-by-side (*i.e.* two-dimensional) interactions. Two-dimensional junctions could facilitate the formation of a single-molecule device network and is the foundation to chapter 5.

Product Characterisation Breakdown

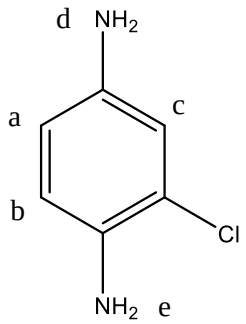

2-chlorobenzene-1,4-diamine

^{1}H NMR (400 MHz, $CDCl_3$) δ_H 6.68 (d, *J* = 4, 1H, Ha), 6.63 (d, *J* = 8, 1H, Hb), 6.48 (dd, *J* = 8, 1H, Hc), 3.64 (s, 2H, Hd), 3.35 (s, 2H, He).

IR: 3321.57 cm^{-1}, 1601.16 cm^{-1}, 1500.18 cm^{-1}, 1234.25cm^{-1}, 710cm^{-1}.

Melting Point: 64.1-65.8°C

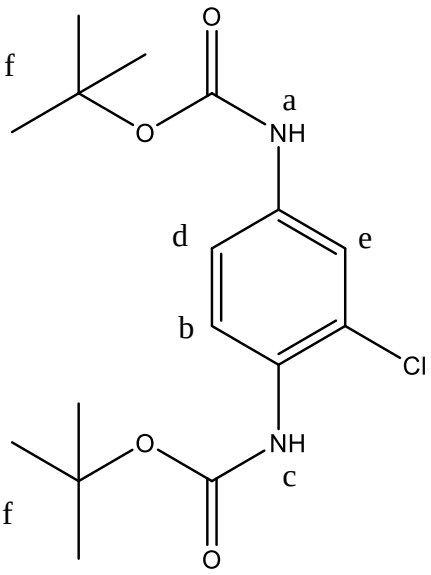

di-tert-butyl (2-chloro-1,4-phenylene)dicarbamate

^{1}H NMR (400 MHz, $CDCl_3$) δ_H 7.95 (d, J = 8, 1H, Ha), 7.57 (s, 1H, Hb), 6.95 (dd, J = 8, 1H, Hc), 6.78 (s, 1H, Hd), 6.32 (s, 1H, He) 1.45 (m, J = 8, 18H, Hf).

IR: 3313.17 cm^{-1}, 2980.02 cm^{-1}, 1695.47 cm^{-1}, 1535.84 cm^{-1}, 1152.42 cm^{-1}, 630.44 cm^{-1}.

Mass Spec: MS (ESI+) m/z: Found 360.1686 $[M+NH_4]^+$ (calc. for $C_{16}H_{27}ClN_3O_4$: 360.1685).

Melting Point: 52.1-54.2°C

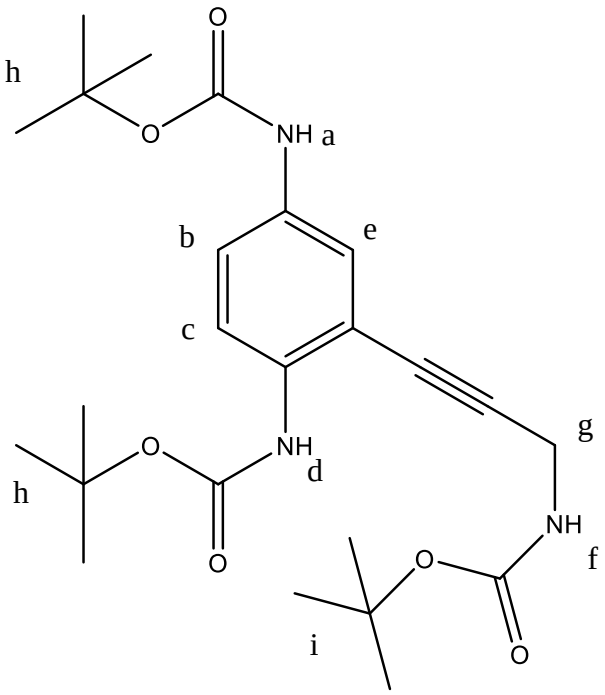

di-tert-butyl (2-(3-((tert-butoxycarbonyl)amino)prop-1-yn-1-yl)-1,4-phenylene)dicarbamate

^{1}H NMR (400 MHz, $CDCl_3$) δ_H 7.54 (s, 1H, Ha), 7.14 (d, *J* = 8, 1H, Hb), 6.95 (d, *J* = 8, 1H, Hc), 6.37 (s, 1H, Hd), 6.15 (s, 1H, He), 5.02 (s, 1H, Hf), 4.26 (d, *J* = 8, 2H, Hg), 1.43 (m, *J* = 24, 18H, Hh), 1.19 (s, 9H, Hi).

IR: 3309.90 cm^{-1}, 2942.75 cm^{-1}, 2977.20 cm^{-1}, 2831.10 cm^{-1}, 1446.9 cm^{-1}, 1024.35 cm^{-1}.

Mass Spec: MS (ESI+) m/z: Found 479.2858 $[M+NH_4]^+$ (calc. for $C_{24}H_{39}N_4O_6$: 479.2851)

Melting Point: 58.2-60.1°C

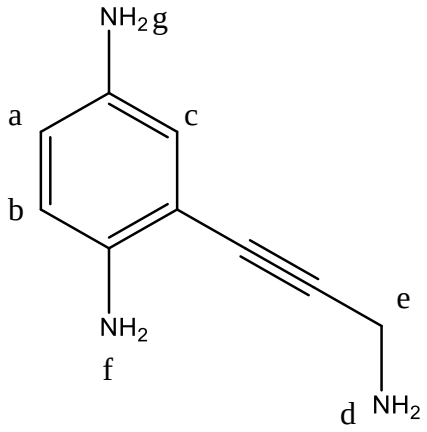

2-(3-aminoprop-1-yn-1-yl)benzene-1,4-diamine

^{1}H NMR (400 MHz, D_2O) δ_H 7.66 (s, 1H, Ha), 7.62 (d, *J* = 12, 1H, Hb), 7.22 (d, *J* = 12, 1H, Hc), 6.73 (s, 2H, Hd), 4.41 (s, 2H, He), 2.09 (s, 2H, Hf), 2.03 (s, 2H, Hg).

IR: 3320.10 cm^{-1}, 2956 cm^{-1}, 2924.97 cm^{-1}, 1693.92 cm^{-1}, 1516.28 cm^{-1}, 1364.85 cm^{-1}.

Mass Spec: HRMS (ESI+) m/z: Found 162.1022 $[M+H]^+$ (Calc for $C_9H_{12}N_3$: 162.1026).

Melting Point: 98.6-100.1°C

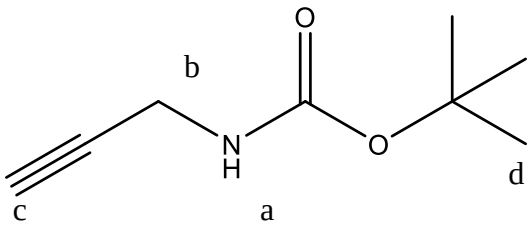

N-Boc-propagylamine

^{1}H NMR (400 MHz, $CDCl_3$) δ_H 4.70 (s, 1H, Ha), 3.91 (s, 2H, Hb), 2.21 (t, J = 12, 1H, Hc), 1.44 (s, 9H, Hd).

Only ^{1}H NMR spectra characterisation needed of *N*-Boc-propargylamine to confirm the structure of synthetic products.

5.0 Two-Dimensional Control and Assembly of Molecular Junctions

5.1. Introduction

Due to their unique mechanical and electrical properties, single-walled carbon nanotubes (SWCNTs) have been the focus of substantial research since their discovery in 1991.[8] Controlling the positioning of carbon nanotubes into junctions, assemblies, and superstructures has been a goal towards the development of novel applications.[211,212] In this regard, the controlled fabrication of junctions formed among different nanotubes as well as between SWCNTs and functional molecules, has gathered significant interest.[213] SWCNT junctions have been produced with different techniques, such as chemical vapor deposition (CVD), arc discharge, laser ablation, and electrical welding, as well as with in-solution strategies.[120,214–222]

Moreover, the development of novel SWCNT-assemblies is an ambition for a new generation of materials that can complement and exhibit enhanced physical properties with respect to the current forms of nanotube-based structures. Various interactions have been exploited towards this end, including hydration forces, electrostatics, and by cooperative assembly with block copolymers or micellar systems.[223–227]

In this regard, DNA has been employed to guide the assembly of SWCNTs *via* its molecular recognition capability.[57,228,229] SWCNTs can be dispersed with DNA *via* non-covalent wrapping without the disruption of nanotubes' desirable electrical properties that can potentially arise when employing covalent strategies (due to acid treatments).[41,158,230,231] DNA-wrapped SWCNTs have been employed in the formation of end-to-end junctions and for the fabrication of carbon-based molecular transport junctions.[120,134] Additionally, the DNA wrapped around the nanotubes can be used to control SWCNT aggregation *via* DNA hybridization, as interactions between DNA linkers wrapped on neighbouring nanotubes can cooperatively guide the assembly of SWNTs into junctions and assemblies.[229,232] It is also

worth noting the importance of the controlled assembly of functionalised DNA-SWCNTs when considering the growing field of stimuli-responsive assembly of SWCNTs.[233–235]

The focus of this study was the assembly of DNA-wrapped SWCNTs into two-dimensional (2D) structures in aqueous solution. The employed SWCNT were wrapped with DNA sequences exhibiting specific chemical functionalities that allowed for metal coordination and cycloaddition reactions to take place. This was exploited to drive the assembly of SWCNTs in 2D structures *via* side-to-side interactions: we found that changes in the reaction conditions led to changes in the structures obtained. Moreover, by dispersing our SWCNT-based assemblies into a polymer matrix, the mechanical properties of thin films can be modified in relation to the kind of SWCNT assemblies employed. In this chapter, we discuss the formation of 2D SWCNT networks in 2-dimensional configurations. Furthermore, it was found that changes in reaction conditions lead to a range of different structures that could open up possible applications outside the field of molecular electronics. Controlling the positioning of tubes into well-defined orientations has been a goal in nanotechnology as it may produce structures with novel physical properties.[222] Drawing on already published forms of SWCNT-based structures, including aligned carbon nanotube films, fibers, buckypapers and aerogels, the development of novel assemblies is a well-held ambition in the field.[236–239]

Combining two established techniques of wrapping functionalised ss-DNA onto SWCNTs (as described in chapter 3) with bridging ss-DNA moieties by the CuAAC reaction, novel side-by-side SWCNT configurations can be achieved by assembly in solution. CuAAC (or “click” chemistry) is a term introduced by K. B. Sharpless in 2001to describe reactions that are high yielding, wide in scope and create by-products that can be removed without chromatography. Furthermore, the reactions are stereospecific, simple to perform and conducted in solvents that are easy to remove or benign.

Previously, nanotubes have reportedly required to be dispersed *via* acidification prior to interconnecting two-dimensionally.[222] This approach can often lead to disrupting the overall structure, and therefore the physical and electrical properties, of the SWCNTs.[231] Additionally, this approach cannot control the formation of 1-dimensional systems (*i.e.* bridging) as discussed in chapter 3. Employing modified DNA sequences to wrap SWCNTs will maintain the integrity of the nanotube and facilitate the formation of molecular junctions in 2D orientations.[120]

5.2. Results and Discussion

The SWCNTs employed in this study were sonicated and dispersed in water *via* side-wall interactions with functionalised ss-DNA.[41,43] The ss-DNA sequences employed are based on a GT_{20} template, where functional group modifications are established *via* uracil nucleotides. DNA sequences modified with alkyne and azide functional groups were employed in order to subsequently induce the assembly of DNA wrapped SWCNTs into two-dimensional structures *via* metal coordination and CuAAC reactions among the DNA wrapped around the tubes' side-walls. To monitor the assembly of structures, nanotube solutions were cast onto silicon substrates and imaged them with AFM and TEM. Figure 62 shows an AFM image of DNA wrapped SWCNTs, our starting material before any assemblies are formed. It is worth noting that the starting material is not sorted by length (as done in previous chapters) as the focus of this study is the formation of structures in side-by-side configurations rather than end-to-end interactions. Therefore, the lengths of nanotubes in the starting material will vary, however the widths will remain consistent to those in previous chapters.

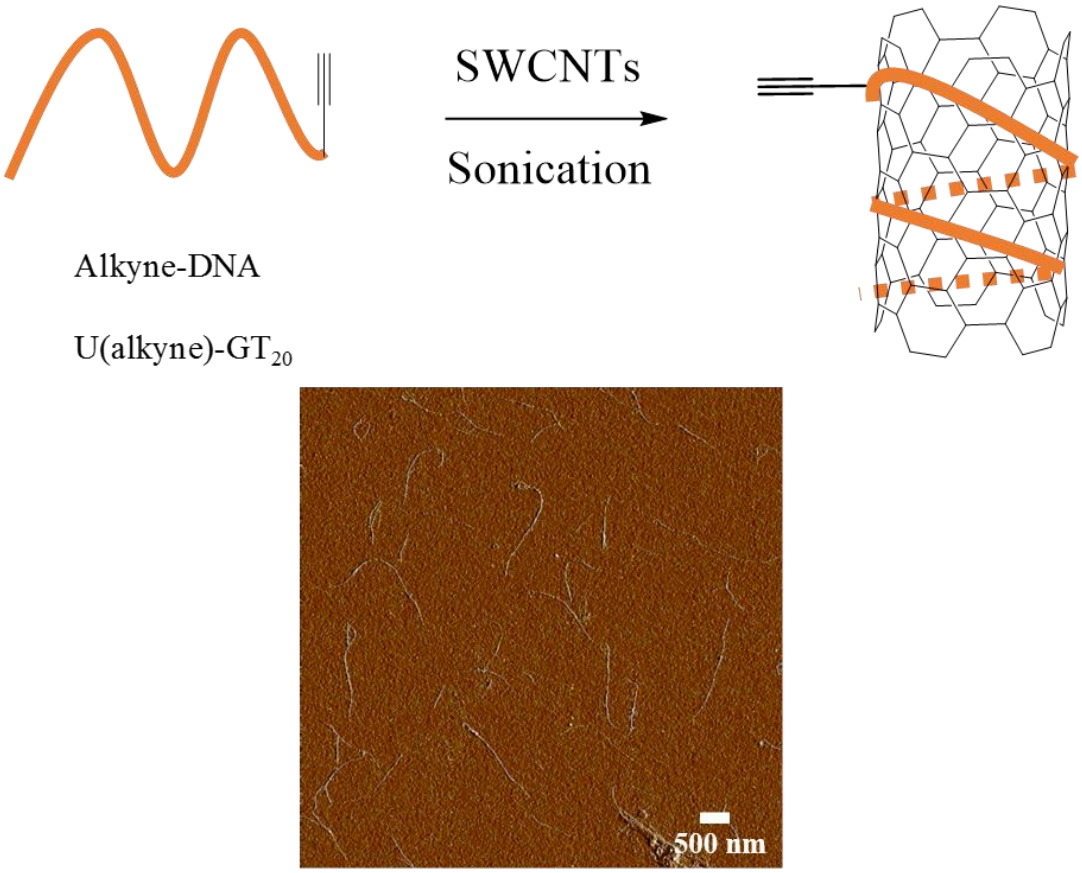

Figure 62. Schematic of ss-DNA with alkyne-modified sequence wrapping around SWCNT. AFM image of DNA-SWCNTs on silicon dioxide (SiO_2) substrate.

Figure 63 shows the contrast between a DNA-SWCNT solution and SWCNTs in an aqueous solution without dispersing agent. With dispersing agent (ss-DNA, GT_{20}) present, nanotubes are clearly visible with AFM and samples appear as homogenous black solutions. Carbon nanotubes without a supporting dispersing agent display a solution with black aggregates suspended in a transparent solution.

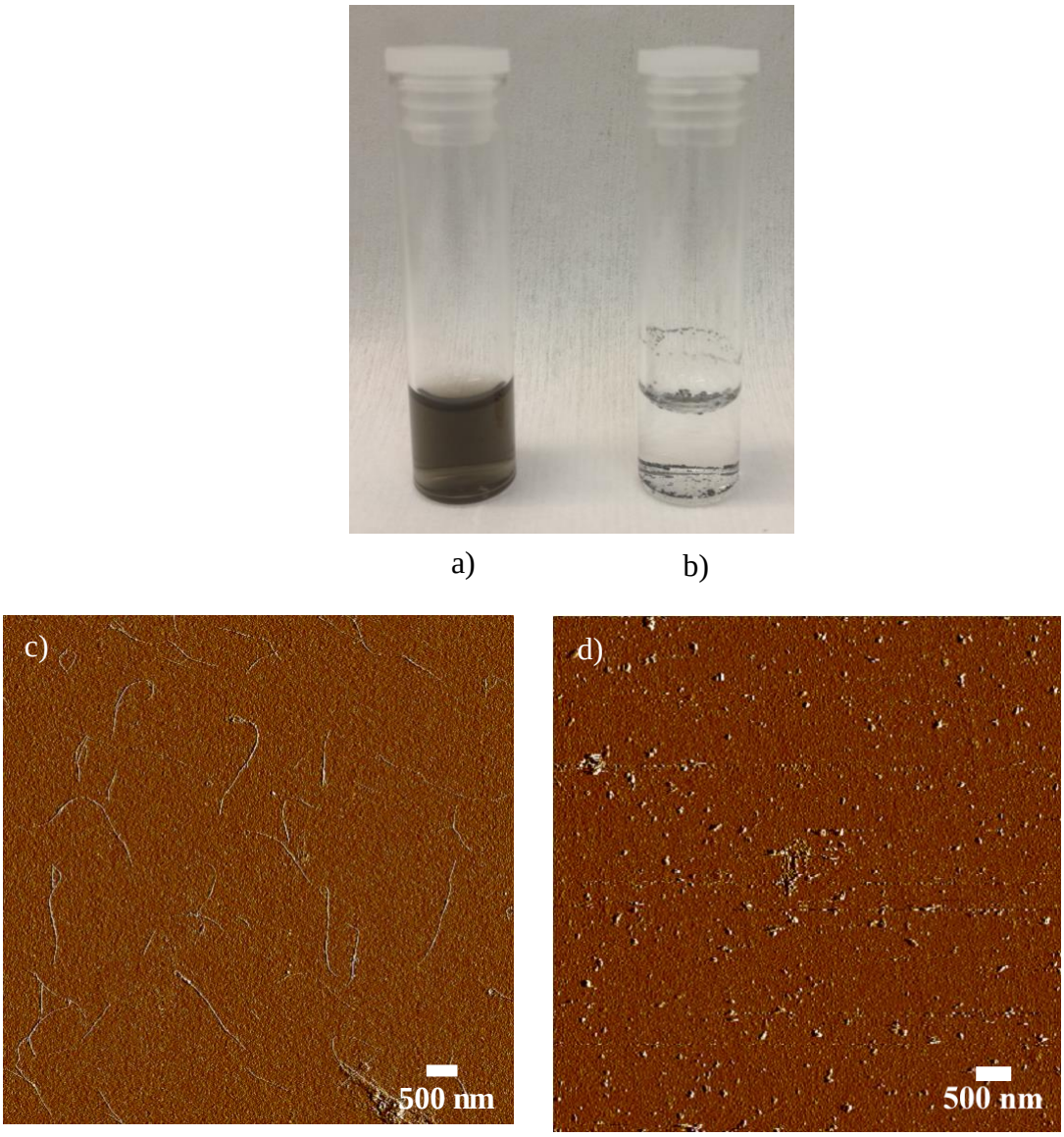

Figure 63. a) Photograph of DNA-SWCNT solution. b) Photograph of SWCNTs in aqueous conditions (without dispersing agent). c) AFM image of DNA-SWCNTs. d) AFM image of SWCNTs in aqueous conditions.

5.2.1. Cu(II) Induced Alkyne-SWCNT Assembly

Cu(II) can coordinate to alkyne and azide groups.[240–242] As shown in the mechanism of CuAAC, copper species can co-ordinate azide-alkyne and azide-azide configurations.[243] The presence of terminal alkynes, copper species and azides, can result in the formation of a copper

acetylide. In order to exploit this, we dispersed SWCNTs in aqueous solution using alkyne-modified DNA (alkyne-SWCNTs), and induced the formation of SWCNTs assemblies by the addition of Cu(II)-based species ($Cu(OAc)_2$ or $CuSO_4$, each at a concentration of 0.4 M). A complimentary bis-linker, 1,12-diazidododecane, was employed, leading to the formation of the nanotube-based structures shown in Figure 65.

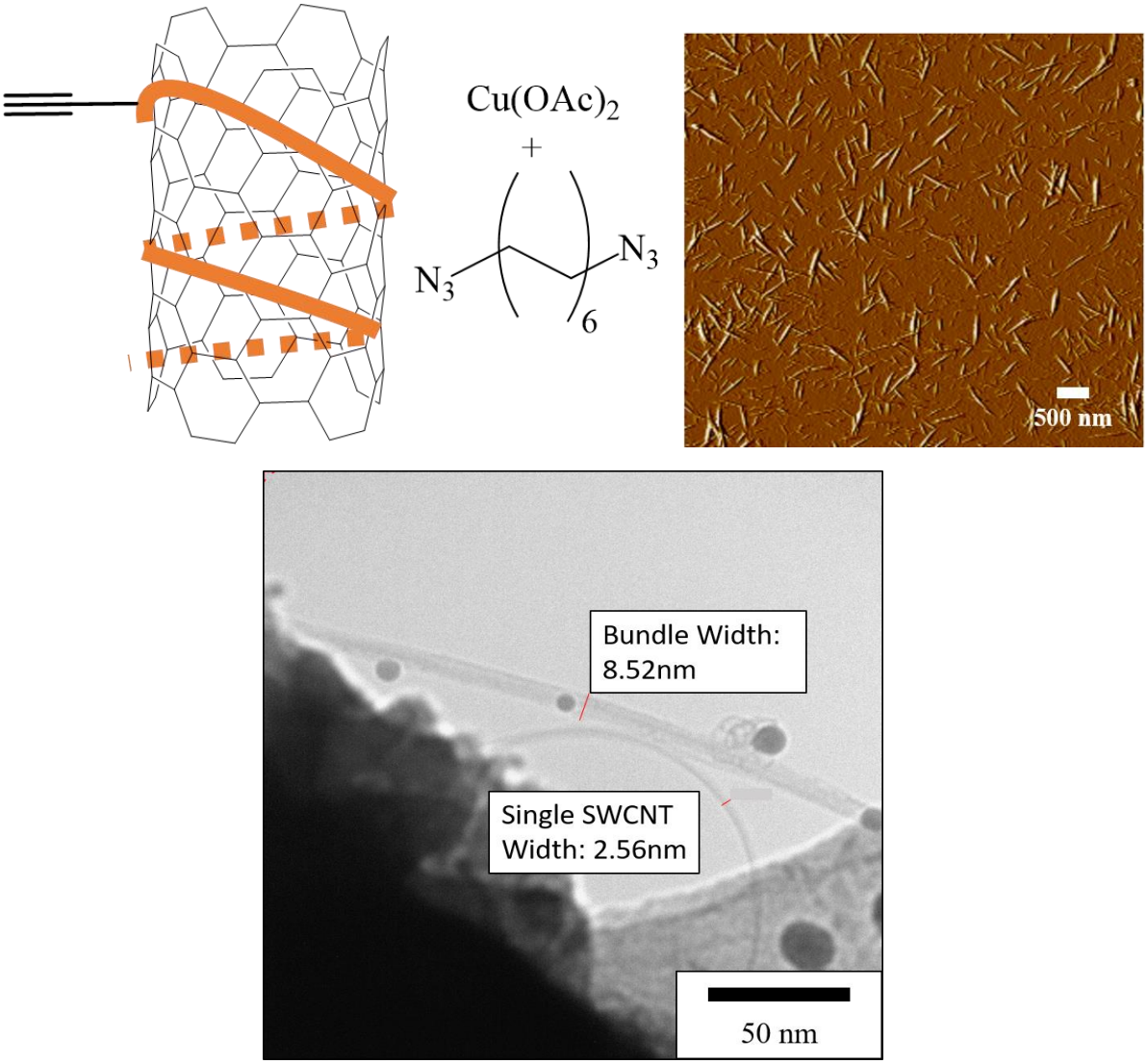

Figure 65. a) Schematic of the assembly of two SWCNTs with copper species and a bis-azide linker. AFM image of the SWCNT-based structures. b) TEM image of SWCNT-based structure with a single SWCNT present for comparison.

The pristine DNA-wrapped SWCNTs exhibit an average width of 3.1 ± 1.3 nm, as determined by AFM investigations. Differently, the alkyne-SWCNTs after reaction with $Cu(OAc)_2$ and

1,12-diazidododecane, exhibited an average width of 21.1 ± 7.2 nm, and height up to ca 29.6 nm, indicating the formation of SWCNT assemblies. This is evident from high magnification AFM images shown in Figure 66. This AFM topographical analysis suggests that on average the alkyne-SWCNT assemblies are formed by 6 to 7 nanotubes per assembly.

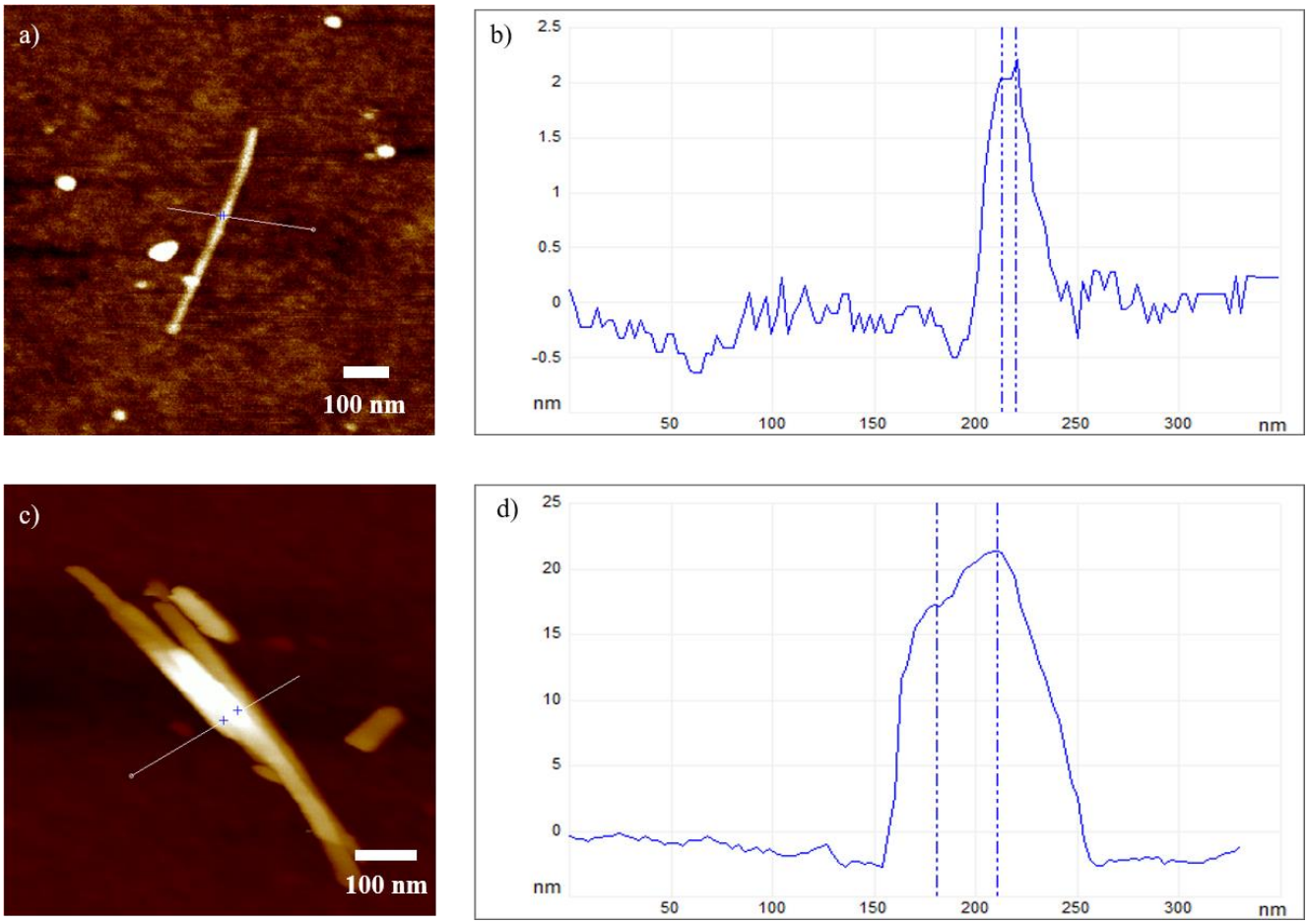

Figure 66. a) AFM of a pristine alkyne DNA-wrapped SWCNT. b) Height profile of pristine alkyne DNA-SWCNT measured: 4.4nm c) AFM of alkyne-SWCNT assemblies. d) Height profile of alkyne-SWCNT assemblies measured: 20.2 nm.

When $Cu(OAc)_2$ was employed with alkyne-SWCNTs without the presence of the 1,12-diazidododecane linker, an increase in the width of the structures was observed, with an average of 10.1 ± 5.8 nm, suggesting the formation of assemblies of 3 nanotubes. This indicates that Cu(II) displays a more efficient coordination between alkyne and azide species in our assemblies, compared to alkyne only. This can be ascribed to the generation of copper(II)

complexes in a potential copper-mediated oxidative acetylenic coupling, as previously observed in different sets of experiments.[240] Most importantly, when Cu(II) was not added to the alkyne-SWCNT solution, no assemblies were observed. Therefore, the presence of a Cu(II) species is required to form SWCNTs assemblies.

5.2.2. Cu(II) Induced SWCNT Assembly with Multiple Alkyne Functional Groups

We further investigated the behaviour in the assembly when multiple alkyne functional groups were present on each individual wrapping DNA strand. Figure 67 shows AFM topographical images of SWCNT assemblies obtained with "parallel" alkyne DNA sequences (two alkyne groups per DNA strand, see the schematic in Figure 67a) and with "zig-zag" alkyne DNA sequences (three alternating alkyne groups per DNA strand, see Figure 67b), in reactions with $Cu(OAc)_2$ and the complimentary bis-linker, 1,12-diazidododecane. Our findings show that the use of "parallel" alkyne DNA-wrapped SWCNTs give rise to SWCNT assemblies of comparable geometry to the alkyne-SWCNT assemblies (obtained with one alkyne per DNA strand). Differently, the use of "zig-zag" alkyne DNA sequences increased as expected the number of interactions per SWCNT in the formed assemblies, generating disordered star-like structures.

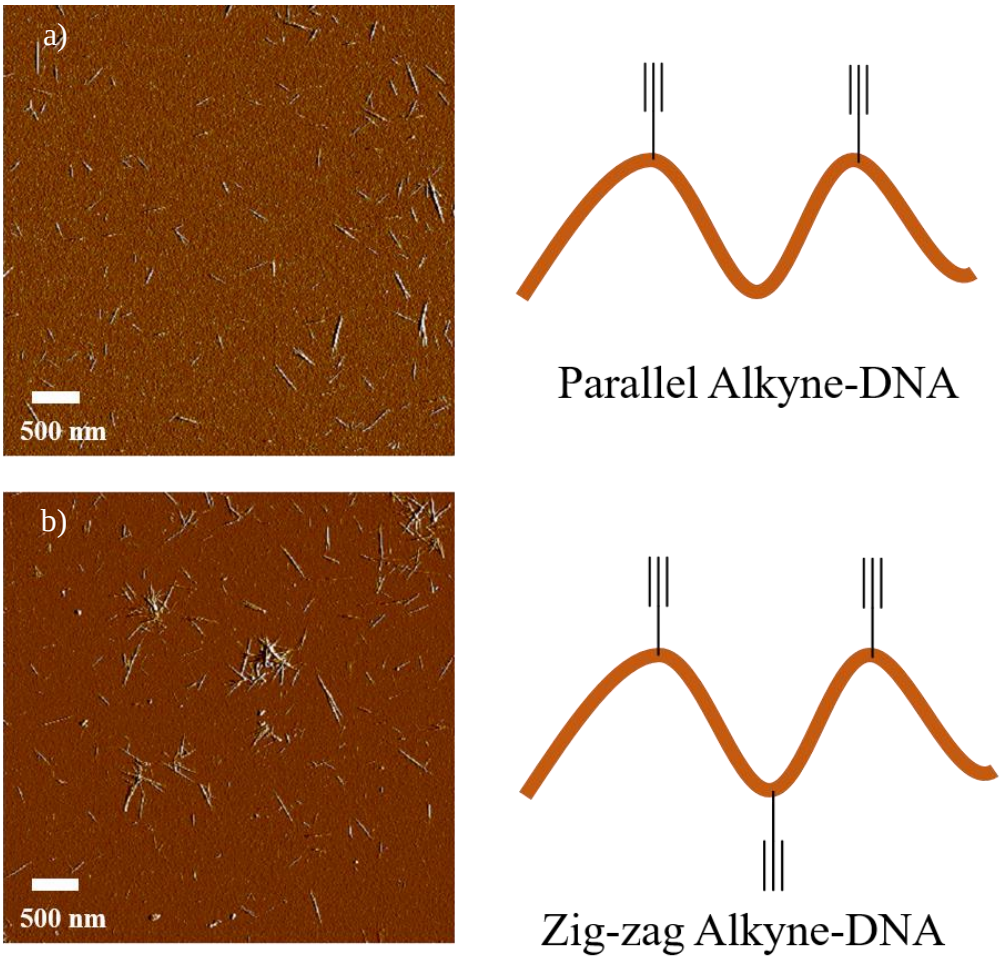

Figure 67. a) AFM image of SWCNT assemblies and parallel alkyne DNA sequence utilised; b) AFM image of SWCNT assemblies and zig-zag alkyne DNA sequence utilised.

From the results presented, the formation of SWCNT-based networks with defined spacing between each tube is a very challenging task. We concluded from this set of experiments and results that bundling of tubes is possible in 2D assemblies, but the next challenge is to develop a methodology that produces defined orientations with a high degree of precision. The method outlined could be used as a foundation for future work to attain the required level of precision.

5.2.3. Cu(II) Induced 2D Azide-SWCNT Assembly

To explore the versatility of assembly in the formation of SWCNT structures, we employed ss-DNA sequences functionalised with azide groups (azide-SWCNT) to disperse the tubes in

aqueous solution, and used alkyne molecules as side-to-side bridging linkers. Figure 68 displays AFM topographical images of the azide-SWCNT assemblies obtained employing different linkers, namely bis-alkyne and tris-alkyne molecules.

The SWCNT assemblies obtained in this case display a more ordered structure compared to assemblies from alkyl-SWCNTs, with minimal random crossing between SWCNTs and no star-like assemblies. Moreover, no significant differences were observed employing either linear or branched alkyne linkers. While the pristine azide-SWCNT exhibit an average width of 5.1 ± 1.2 nm as determined by AFM, the compact two-dimensional (2D) SWCNT structures observed exhibit a width of 20.3 ± 6.9 nm, suggesting the formation of assemblies of *ca*. four SWCNTs.

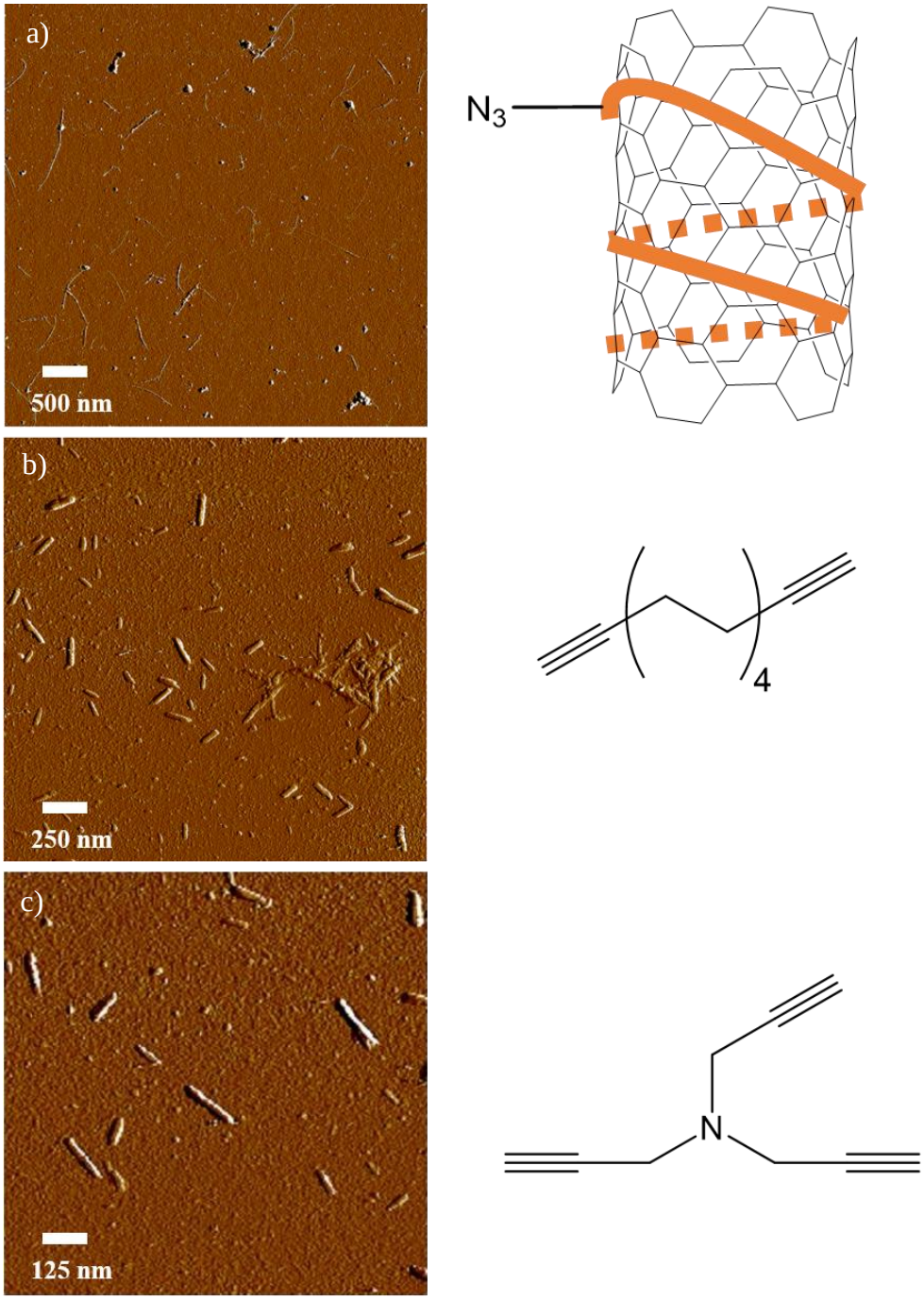

Figure 68. a) AFM image and schematic of pristine azide-functionalised DNA-SWCNTs.;b) AFM image of 2D SWCNT structures and bis-alkyne linker; c) AFM image of 2D SWCNT structures and tri-alkyne linker.

5.2.4. Cu(II) Induced 2D Structure Assembly with Alkyne-SWCNTs and azide-SWCNTs

From the results shown, it is reasonable to suggest that the functional group selection on ss-DNA is the key driving force behind the formation of SWCNT assemblies when a copper species and complimentary linker is introduced. Therefore, it is necessary to investigate whether there is a further structure available if alkyne-SWCNTs were to coordinate with azide-SWCNTs without a linker present. Adding the two pristine DNA-wrapped SWCNT solutions in equal ratio (alkyne-SWCNT and azide-SWCNT) with 0.4 M copper species lead to the formation of SWCNT assemblies with compact structural features, in line with the 2D structures obtained from azide-SWCNTs, with minimal random crossing between SWCNTs and no star-like assemblies.

Figure 69 shows a schematic of the system and a representative AFM image of the SWCNT assemblies attained in this way. The average width of these 2D SWCNT structures was found to be of 21.0 ± 6.3 nm, *i.e.* comparable to the ones obtained from azide-SWCNT experiments, indicating the presence of 4 to 5 SWCNTs per assembly.

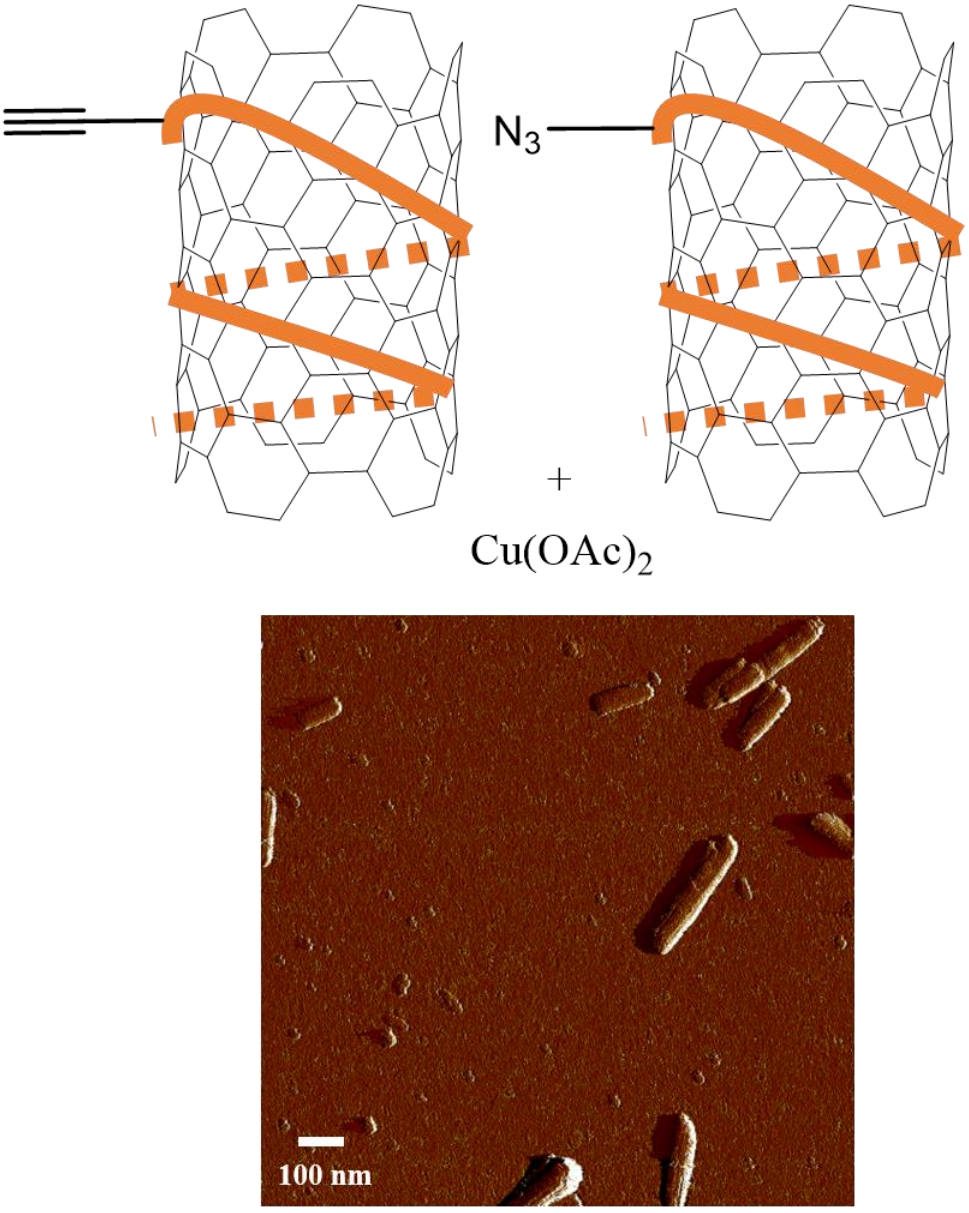

Figure 69. Schematic of copper induced coordination between parallel alkyne-SWCNTs and azide-SWCNTs. AFM topographical image of the 2D nanotube structures obtained.

Azide driven assemblies show that the overall structure of bundles can be predicted to a good degree of control. Much like alkyne driven assemblies, these findings could provide a suitable platform for future work to develop a methodology with a high degree of control in nanotube positioning. A possible explanation regarding the shorter structures observed, are that the shorter tubes give rise to these structures while longer CNTs form more disordered aggregates/networks due the greater chance of overlap between different nanostructures and

greater curvature.

Table 7 summarises the average widths of all the SWCNT assemblies obtained in the different experimental conditions investigated in this study where $CuSO_4$ is utilised as Cu(II) species.

Table 7. Average widths of various nanotube structures. The copper species must be present to coordinate between complimentary functional groups to form SWCNT assemblies. Histograms of all nanostructure assemblies are provided below.

Carbon Nanotube Structure	**Average Width (nm)**
Pristine Alkyne-SWCNT	**3.1 ± 1.3**
Pristine Azide-SWCNT	**5.1 ± 1.2**
Alkyne-SWCNT + 1,12-diazidododecane (No $CuSO_4$)	**3.6 ± 1.7**
Azide-SWCNT + dodeca-1,11-diyne (No $CuSO_4$)	**4.9 ± 1.3**
Alkyne-SWCNT + Azide SWCNT (No $CuSO_4$)	**4.7 ± 2.5**
Alkyne-SWCNT + $CuSO_4$ (No Linker)	**10.1 ± 5.8**
Azide-SWCNT + $CuSO_4$ (No Linker)	**11.2 ± 4.1**
Alkyne-SWCNT + 1,12-diazidododecane + $CuSO_4$	**21.1 ± 7.2**
Azide-SWCNT + dodeca-1,11-diyne + $CuSO_4$	**20.3 ± 6.9**
Alkyne-SWCNT + Azide-SWCNT + $CuSO_4$	**21.0 ± 6.3**

Figures 70 and 71 display the histograms of the widths measured for pristine nanotubes. These values represent the benchmark of the study when compared to the other nanotube structures. It is worth noting that the standard deviation and mean values of both pristine tubes are within tolerance of one another, 3.1 ± 1.3 nm and 5.1 ± 1.2 nm respectively.

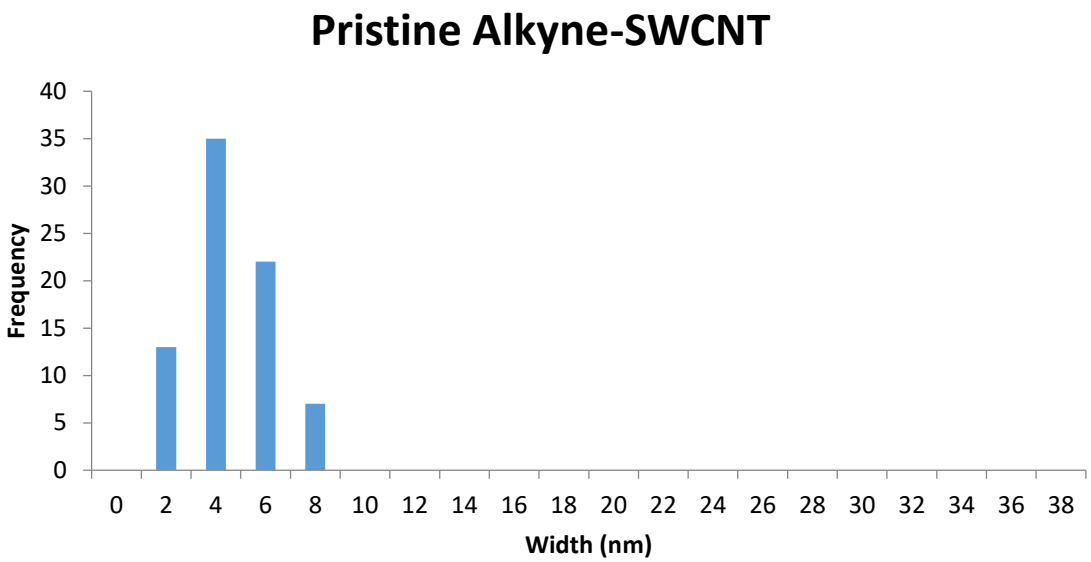

Figure 70. Histogram of pristine alkyne-SWCNTs. Average width: 3.1 ± 1.3 nm. 77 counts, 4 samples.

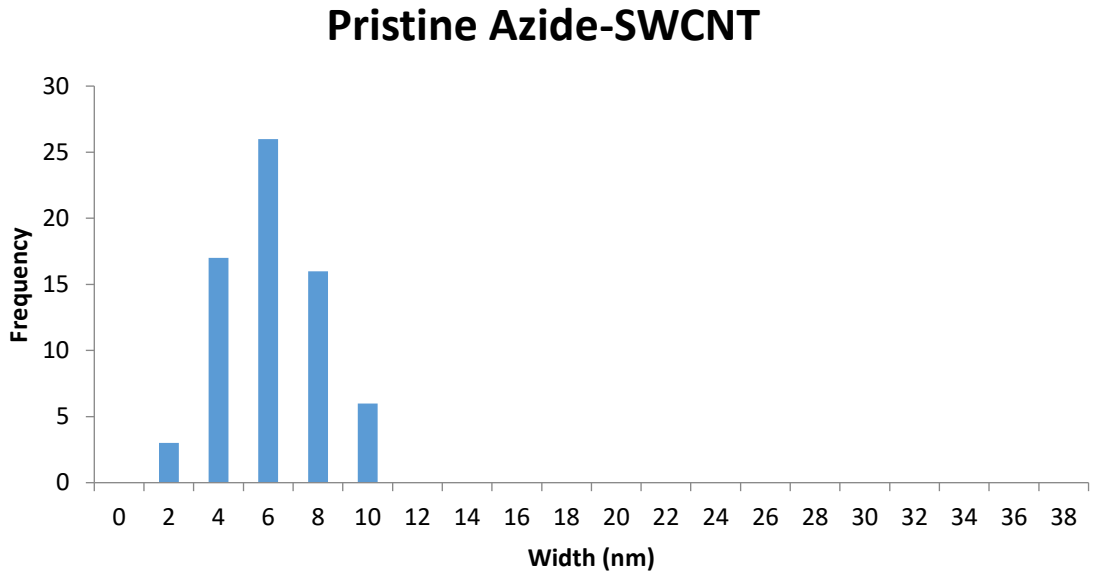

Figure 71. Histogram of pristine azide-SWCNTs Average width: 5.1 ± 1.2 nm. 69 counts, 4 samples.

To investigate the efficacy of copper species, assembly formation reactions were performed without $CuSO_4$ or $Cu(OAc)_2$. Figures 72, 73 and 74 display the histograms of pristine nanotubes with complimentary linkers without a Cu(II) species. All average and standard deviation values are within tolerance of one another, suggesting an oxidising agent or catalytic species is necessary to trigger a novel structure formation.

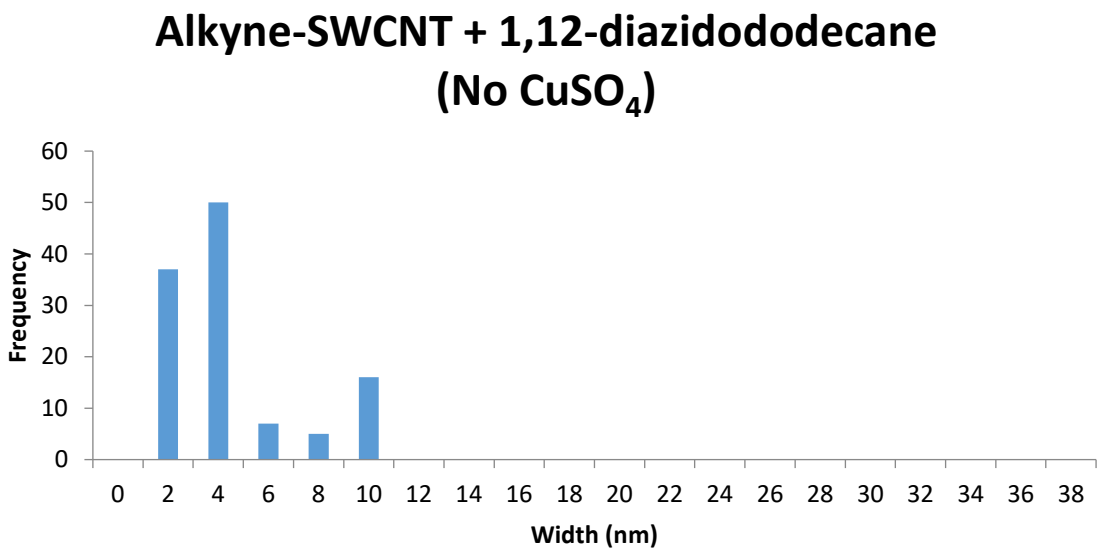

Figure 72. Histogram of pristine alkyne-SWCNTs with 1,12-diazidododecane without Cu(II) species. Average width: 3.6 ± 1.7 nm. 78 counts, 4 samples.

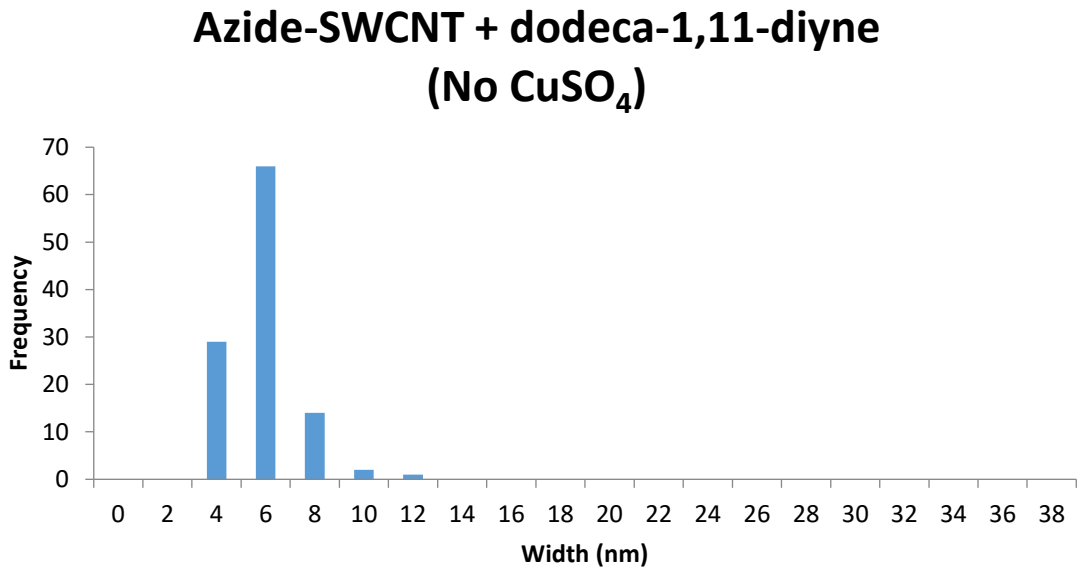

Figure 73. Histogram of pristine azide-SWCNTs with 1,12-diazidododecane without Cu(II) species. Average width: 4.9 ± 1.3 nm. 78 counts, 4 samples.

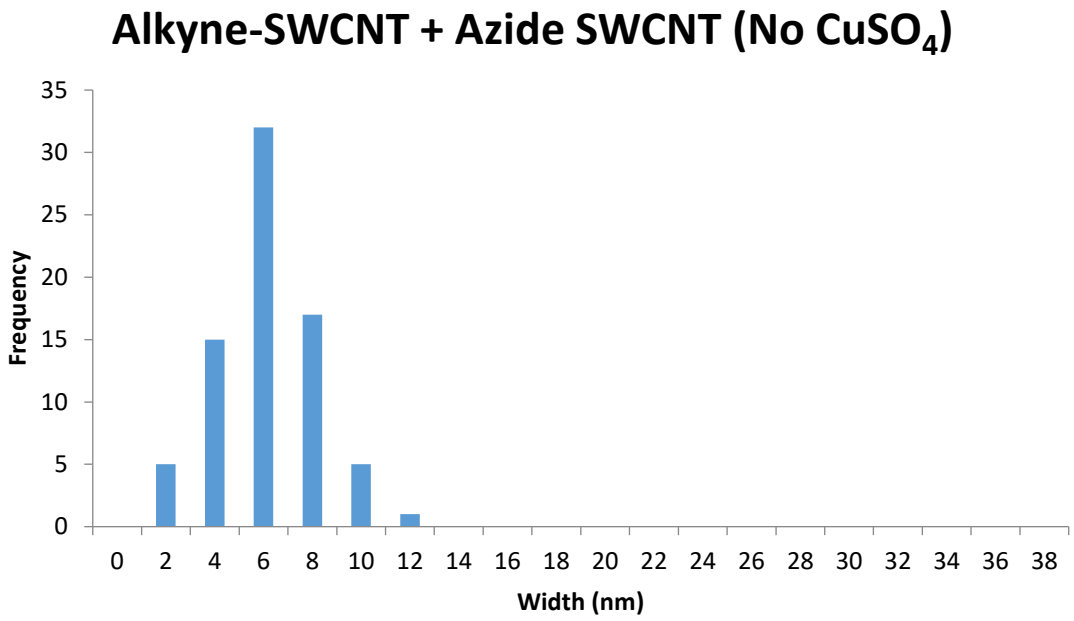

Figure 74. Histogram of pristine alkyne-SWCNTs with pristine azide-SWCNTs without Cu(II) species. Average width: 4.7 ± 2.5 nm. 76 counts, 4 samples.

Assembly reactions were performed without linkers to demonstrate the efficacy of the complimentary linkers. Figures 75 and 76 all show the histograms of pristine SWCNTs with Cu(II) as oxidising/co-ordination agent. Each average and standard deviation value are within tolerance of each another but do show an increase compared to previous results. This highlights that Cu(II) species plays an integral role in the assembly process. As previous studies have shown, Cu(II) species can oxidise terminal alkynes leading to alkyne-alkyne coupling and can co-ordinate adjacent azide species.[240–242] The result of these factors produces novel 2D structures with a relatively low yield.

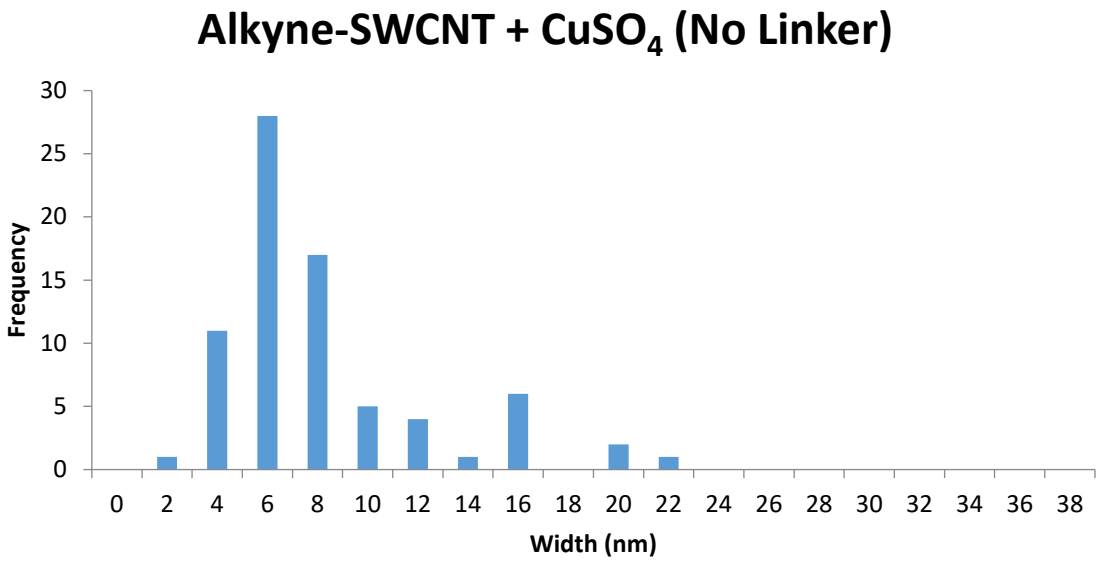

Figure 75. Histogram of pristine alkyne-SWCNTs with Cu(II) species without a linker. Average width: 10.1 ± 5.8 nm. 76 counts, 4 samples.

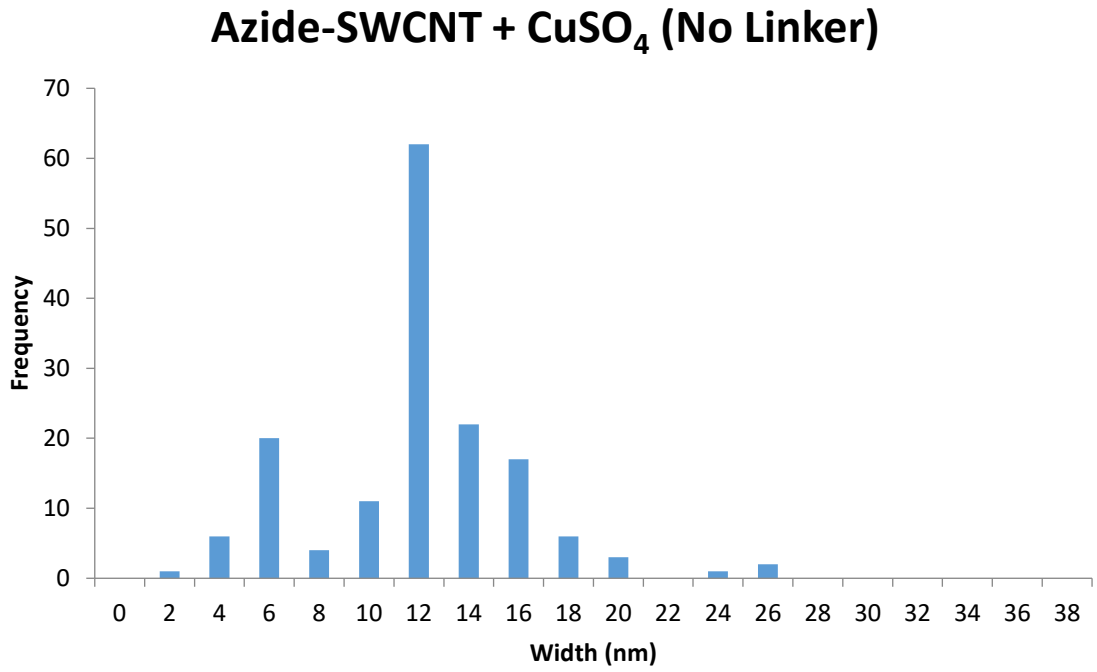

Figure 76. Histogram of pristine azide-SWCNTs with Cu(II) species without a linker. Average width. Average width: 11.2 ± 4.1 nm. 97 counts, 4 samples.

Previous results have shown a relatively low yield of assembly configurations. To fully investigate the yield of assemblies, reactions were performed with appropriate linkers and copper species. Figures 77, 78 and 79 display the histograms of pristine SWCNTs, complimentary linkers and Cu(II) species. All average and standard deviation values are within tolerance of one another and display a significant increase compared to other conditions. Complimentary functional groups with Cu(II) species indicates co-ordination across terminal groups and the potential of some 1,2,3-triazole formations at low yields. Both of these factors contribute to the bundling of nanotubes and thus an increase in width.

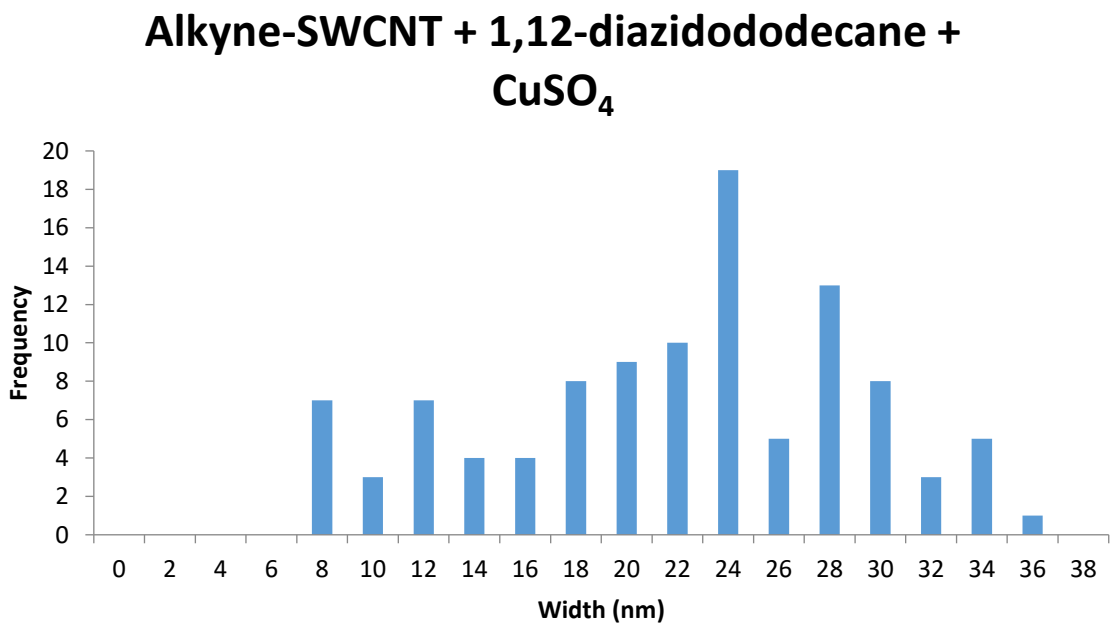

Figure 77. Histogram of pristine alkyne-SWCNTs with 1,12-diazidododecane with Cu(II) species. Average width: 21.1 ± 7.2 nm. 106 counts, 4 samples.

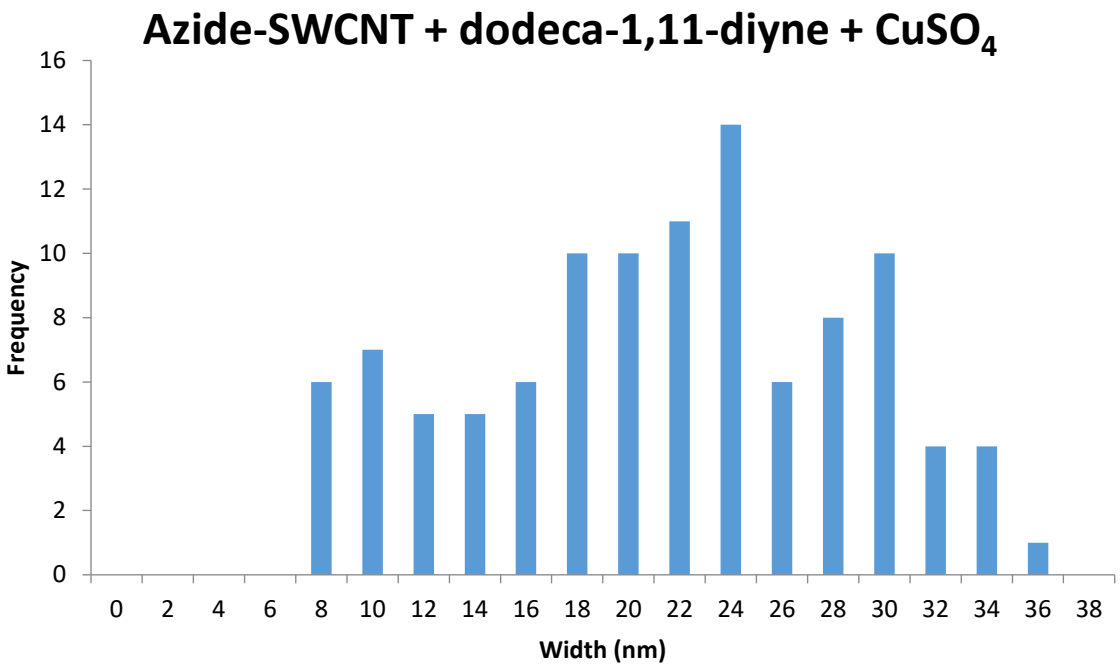

Figure 78. Histogram of pristine azide-SWCNTs with dodeca-1,11-diyne with Cu(II) species. Average width: 20.3 ± 6.9 nm. 107 counts, 4 samples.

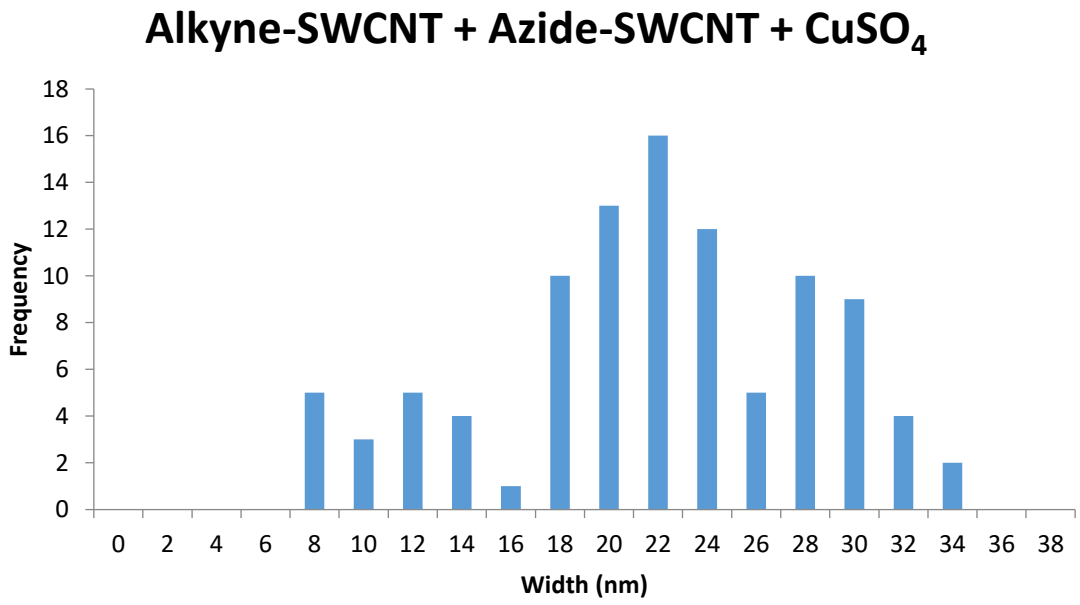

Figure 79. Histogram of pristine alkyne-SWCNTs with pristine azide-SWCNTs with Cu(II) species. Average width: 21.0 ± 6.3 nm. 100 counts, 4 samples.

5.2.5. SWCNT Network Formation *via* "Click" Chemistry

Our investigation into the formation of SWCNT assemblies in aqueous solution, shows that the geometrical configurations are driven by the presence of functional groups on SWCNTs. Copper coordination with functional groups on nanotubes induces specific structures depending on said functionality. It is necessary, therefore, to further investigate how versatile the reactions can form other structures by changing the reaction conditions. By including sodium ascorbate to the reaction conditions, the experimental methodology reflects the conditions found within a typical CuAAC or "click" reaction, *i.e.* dramatically increasing the yield of reaction.[244]

Employing "click" chemistry techniques, alkyne-SWCNTs were "clicked" with azide-SWCNTs with copper species employing sodium ascorbate as a reducing agent. The presence of ascorbate reduces the Cu(II) species to Cu(I), and catalyses the formation of a 1,2,3-triazole, and linking parallel SWCNTs with a higher stability than simple copper coordination.[244] Figure 80a shows a schematic of the final product of this reaction, while Figure 80b and 80c shows TEM images of the SWCNT assemblies obtained.

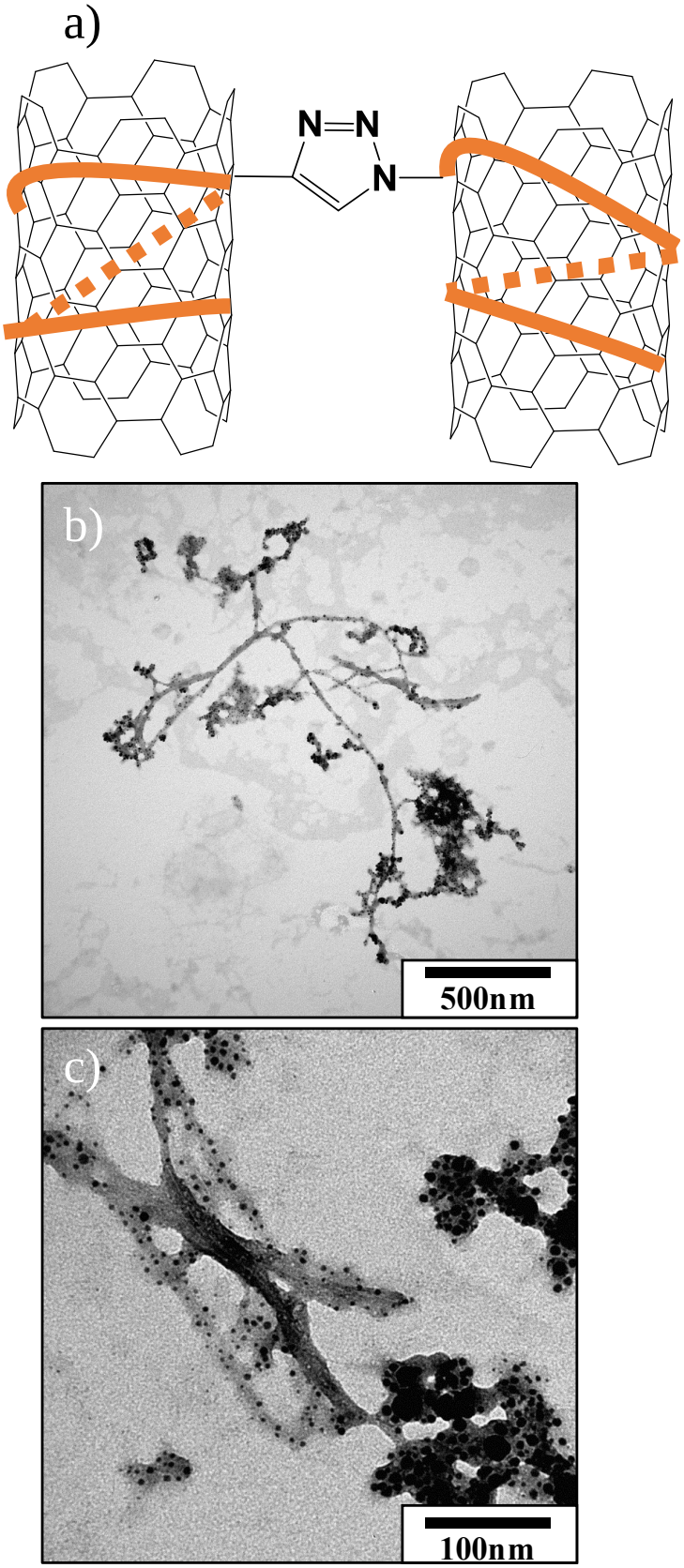

Figure 80. a) Schematic of a single 1,2,3-triazole junction between parallel SWCNTs. b) and c) TEM images of SWCNT networks.

Due to the size of the structures formed, it was necessary to image surfaces with TEM rather than AFM. It is also worth noting that the dark spots on the structures are present from copper aggregations from the catalyst. As expected, the yield of reaction is much higher than in the previous coordination-driven reactions, as more side-by-side junctions are indeed expected to form in “click” reactions compared to the number of coordination sites in 2D structures. TEM images in Figure 80 show a clear difference in overall scale of structure produced. The use of the CuAAC reaction led to the formation of SWCNTs in a network formation (Figure 80b), in addition to increased bundling of tubes (Figure 80c). Tube networks are formed due to further junction formation with branched side-chains, which are not present when only employing a copper co-ordinating species. The presence of a reducing agent allows to exploit copper as a catalyst leading to a significant increase in structure size due to the high yield of 1,2,3-triazole junctions. While the previous SWCNT assemblies display discrete structures typically found to be a few hundred nanometres in length, the length of the nanotube network shown in Figure 83 far exceeds those dimensions, with lengths in the micrometre scale. Therefore, it can be deduced that the use of “click” chemistry reactions between functionalised DNA wrapped around SWCNTs induces the formation of a new type of overall structure (a network), but with only a limited increase in structural width. It is also worth noting that precipitation was observed after 24 hours, suggesting “click” chemistry will continue past the micrometre scale and form aggregates of greater dimensions.

The approach outlined displays SWCNT networks on the micrometre scale. This implies that if the control of nanotube positioning to establish defined circuits is optimised, then there is a real potential for scaling-up network formation. By introducing a reducing agent, the differing structures (and scale) can be selected, offering a range of options when building an electrical circuit in future studies.

5.2.6. Polymer Matrix Reinforced by SWCNT Structures

SWCNTs are lightweight materials with exceptional mechanical, thermal and electrical properties. Therefore, to satisfy these properties within applications, a multifaceted approach is required. By incorporating nanotubes in larger composites, these enhanced properties can be expressed on a larger scale and ultimately in more applications. Furthermore, SWCNTs possess a high aspect ratio (*i.e.* length/diameter), which make them ideal candidates for developing functional and structural polymer/SWCNT materials.[212] Previously, polypropylene was mechanically reinforced by MWCNTs through a melt compounding process followed by hot-processing and solid state drawing.[245] Furthermore, polycarbonate nanocomposites were also reinforced with SWCNTs and MWCNTs with melt compounding.[246]

In this regard, we investigated the effect of the SWCNT assemblies obtained in our studies, on the mechanical properties (change in the Young's Modulus) of polyvinyl alcohol (PVA). By dissolving 10% of each nanotube solution into the polymer matrix, all structures were assessed with respect to the reinforcement of PVA, as reported in published procedures.[247] Force-distance curves were generated using an AFM-based technique, in which the AFM tip comes into contact with the sample surface. Young's Modulus values were then calculated from force-distance curves, followed by average and standard deviation calculation, as shown in Figure 81.

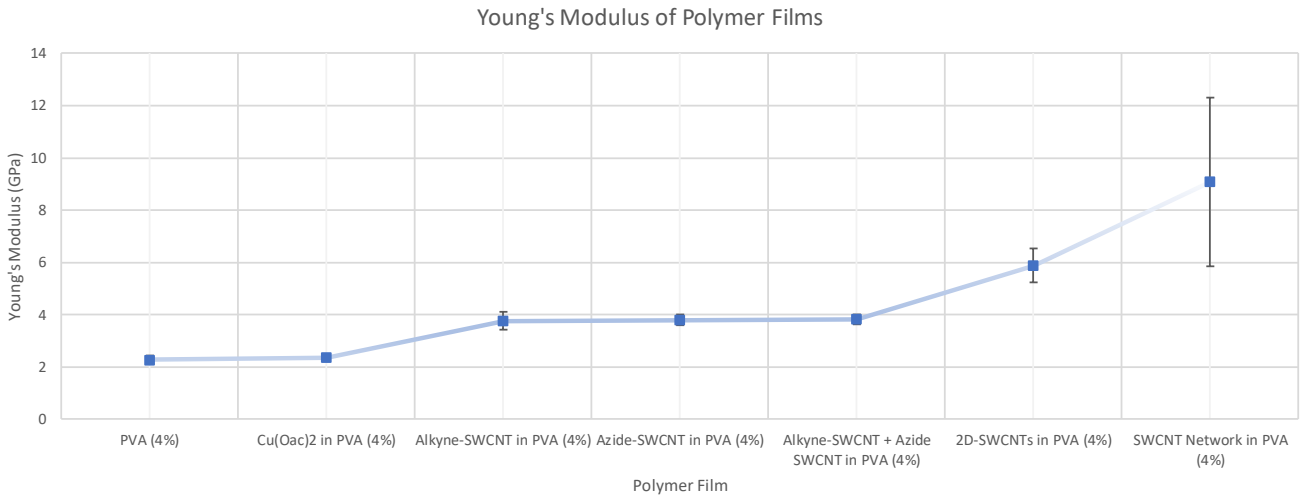

Sample	Young's Modulus (GPa)	Standard Deviation
PVA (4%)	2.3	0.2
$Cu(OAc)_2$ in PVA	2.4	0.1
Alkyne-SWCNT in PVA	3.8	0.3
Azide-SWCNT in PVA	3.8	0.2
Alkyne-SWCNTs + Azide-SWCNTs in PVA	3.9	0.2
2D SWCNT Structures in PVA	5.9	0.7
SWCNT Networks in PVA	9.1	3.2

Figure 81. Chart and table of Young's Modulus values obtained via AFM for all polymer film samples.

Pristine SWCNTs show the expected gradual increase in the Young's modulus value of PVA compared to the pristine polymer; however, the inclusion of SWCNT 2D structures and networks considerably increases the recorded Young's modulus. The presence of 2D SWCNT structures in PVA films compared to when pristine tubes are employed, gives an increase in reinforcement of *ca*. 70%. Moreover, the presence of the SWCNT networks produces an

increase in PVA's Young's modulus of *ca*. 200% compared to when pristine tubes are embedded in the polymer. This implies that the structural differences between SWCNT's 2D structures and networks with pristine tubes are significant and contribute to the overall reinforcement of the polymer film. The value of the Young modulus for PVA films with SWCNT networks also display the highest standard deviation – this is possibly due to the greater range of types of structures and lower uniformity found within the polymer film. "Click" reactions can form networks, as well as bundles (2D structures) which both contribute to the overall reinforcement of the matrix, which in turn provides the greater distribution of Young's modulus values recorded.

Despite showing an application based on another property of SWCNTs, the results outlined show a potential of reinforcing polymer matrixes with electrically active components. Reinforcing matrixes with nanotube networks could provide a starting point for bringing the electronic properties of nanotubes to larger materials.

5.3. Concluding Remarks

The ambition of this study was to form and control a network of single-molecule junctions. The development of novel 2D SWCNT structures provides the foundation for applications that take advantage of the unique electrical and mechanical properties of carbon nanotubes. By exploiting copper(II) catalysed oxidative couplings qualities and "click" chemistry reactions, we have driven the coupling of DNA-wrapped SWCNTs in 2D configurations through side-to-side junction formation, in aqueous solution. We have shown that the geometry of the assemblies can be controlled *via* simple changes in reaction conditions. While disordered crossed SWCNT junctions were initially formed, we have obtained more ordered 2-D structures and SWCNT networks by changing the chemical nature of the reaction driving the

assembly. Moreover, dispersing the different SWCNT-assemblies into a polymer film led to changes in the Young modulus of the film, as confirmed by AFM-based investigations.

5.4. Future Work

Future studies will take advantage of the knowledge developed to investigate changes in electric and electronic properties of SWCNT-based assemblies and of polymer matrices. By and large, the development of new types of SWCNT-based structures can be exploited for different applications, from electronic nanoscale devices, to high strength composites.

Chapters 3 and 4 concluded that single-molecule junctions can be achieved *via* specific procedures that demonstrated end-to-end (1-D) SWCNT assemblies. To realise the full potential of carbon nanotubes, it is necessary to ultimately develop a network of SWCNTs with electrically active components, *i.e.* single-molecule junctions. DNA-wrapped SWCNTs can facilitate end-to-end junction formation; additionally, it has been reported that functionalised ss-DNA forms bridges *via* CuAAC.[248–251] Exploiting this technique, 2D configurations for SWCNTs can be formed, as we have shown in this chapter. Figure 82 illustrates that the control of nanotubes assembly could be a useful framework for future carbon nanotube-based structures for building networks and ultimately circuits for single-molecule electronic devices. This will provide the required framework for all future carbon nanotube-based electrical circuits that utilise electrically active single-molecule junctions that can continue the miniaturisation of electronic devices with bottom-up methodologies.

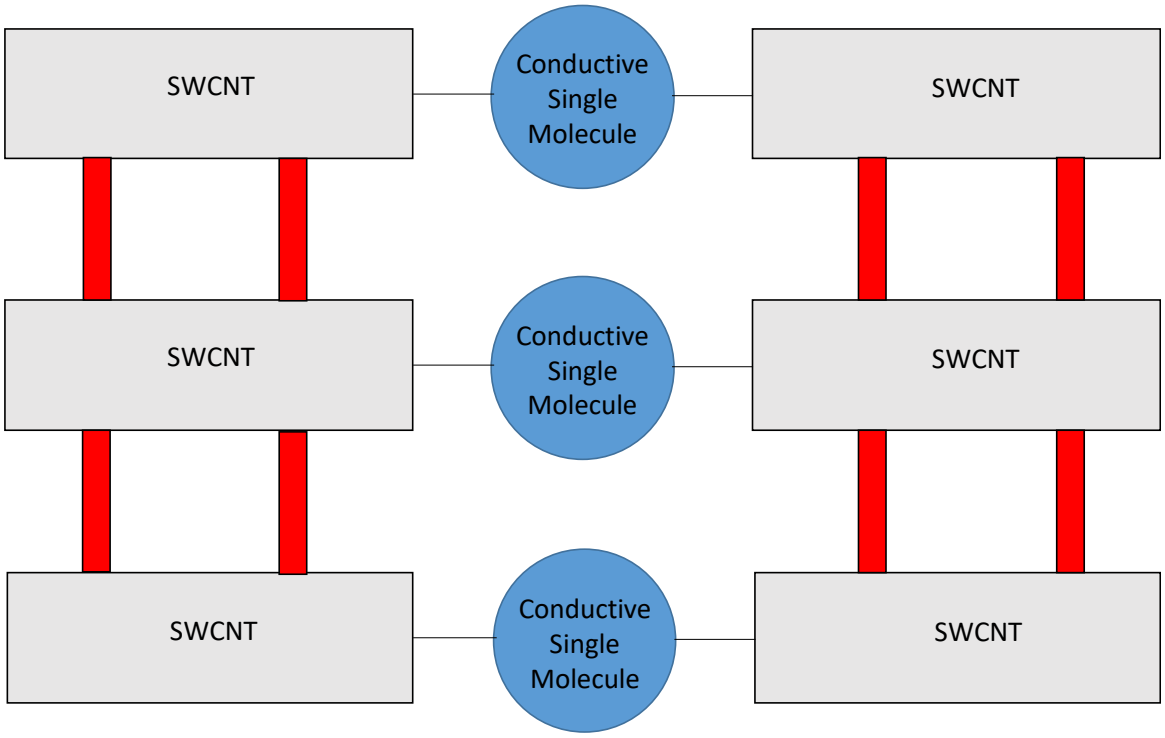

Figure 82. Proposed schematic of SWCNT single-molecule junctions in a network assembly to establish an electrical circuit. Red sections denote junctions that provide side-by-side (2D) assemblies.

6.0 Conclusion

Building nanoscale devices with an electrically active single molecule is one of the ambitions for nanotechnology. One approach to build single molecule devices is to produce molecular junctions directly in solution towards the development of solution-processable strategies for the fabrication of molecular electronic devices. The work presented here has focused on the formation of molecular transport junctions in solution employing carbon nanotubes as nanoelectrodes that were linked by selected organic conjugated molecules (that would in turn act as the electrically active component of the junction). We investigated the versatility of these carbon-based molecular transport junctions in 1-dimensional (both linear and Y-shaped) and 2-dimensional configurations.

The first main focus of the work presented here was the formation of linear molecular junctions, in aqueous solutions, with conjugated diamines, employing DNA-wrapped SWCNTs. This approach showed significant results, where different molecules have been successfully embedded between CNTs as confirmed by AFM investigations. Furthermore, the developed methodology is versatile, *i.e.* many molecular linkers tested successfully form 1-dimensional structures. The method also demonstrated a simple, affordable and environmentally friendly procedure, to form all carbon-based molecular transport junctions in solution. By creating a library of molecular linkers, investigations were carried out on the electrical properties of single molecules, using C-AFM. This can provide the foundation for further studies by extending the library, benchmarking against other findings and understanding new trends in electrical properties. It is possible that this will eventually contribute to the next generation of single-molecule electronic devices, which was explored in the second main focus of this work.

Establishing a synthetic pathway to form three-terminal junctions was a challenging task that focused on the development of a molecular linker with a specific functionality. Synthesising

the final product and demonstrating Y-shape junctions can provide a foundation for future work that exploits the non-symmetric structure of the single molecule. Creating a molecular junction where there are nanoelectrodes with different functionalities will be necessary for introducing increased complexity to developing single-molecule devices that mimic the functionality of a transistor. The next step will be to create methodologies that measure the electrical properties of each nanoelectrode, which could be done *via* progression of the C-AFM methodology described in chapter 3. These results will provide an understanding of whether controlling the positioning of CNT structures can facilitate the building of networks and ultimately electrical circuits, which was explored in the final area of study in this research.

In addition to the work on 1D carbon nanotube junctions, we also explored the fabrication of two-dimensional structures. Exploiting copper-based chemistries, we have shown that side-to-side interactions between DNA-wrapped CNTs could be controlled in order to fabricate different 2D nanotube assemblies. The interaction between the different carbon nanotubes forming these assemblies could be tuned depending on the type of configuration that was required: building nanostructures into side-by-side orientations can provide the foundation for further customisation in order to build specific electrical circuits. Moreover, by embedding the different 2D carbon nanotube assemblies into a polymer matrix, we have shown how the polymer's Young's Modulus could be tuned. In particular, the incorporation of extended 2D CNT networks into the polymer allowed for a significant improvement of the polymer's Young Modulus, an initial application that could potentially develop into electrically active devices, *i.e.* molecular junctions in 2D structures, within polymer films that provide a stiffer film with an electrical response.

What was very rewarding across all studies was how they fed into and complement one another. One could combine the investigation methodologies outlined in chapter 3 with the three-terminal junctions developed in chapter 4, in an ordered two-dimensional assembly developed

by the work described in chapter 5. Overall, this could facilitate the development of a novel electrical device/circuit that can continue the progression of Moore's Law and thus the advancement of (nano)technology. Additionally, this kind of device could assist in the development of quantum computing in future technological advances.

It must also be noted that the potential application of these devices might be unknown at the time of writing. Such is the versatility of carbon nanotube structures and the fast-paced advancement of technology, it can be difficult to predict where these results can play a key role. Nonetheless, these findings have shown significant progression from what has preceded it and can provide an excellent platform for future studies, regardless of where they may lie.

7.0 References

1. M. C. Roco, R. S. Williams, and P. Alivisatos, *Nanotechnology Research Directions: IWGN Workshop Report*. (1999).
2. R. Saini, S. Saini, and S. Sharma, *J. Cutan. Aesthet. Surg.*, 2010, **3,** 32–33.
3. R, Chau, S. Datta, M. Doczy, B. Doyle, B. Jin, J. Kavalieros, A. Majumdar, and M. Metz, *IEEE Trans. Nanotechnol.,* 2005, **4,** 153–158.
4. G. M. Whitesides, and B. Grzybowski, *Science,* 2002, **295,** 2418-2421.
5. Q. Peng, A. K. Dearden, J. Crean, L. Han, S. Liu, X. Wen, S. De, *Nanotechnol. Sci. Appl.* 2014, **7,** 1–29.
6. G. Reiss, and A. Hutten, *Handbook of Nanophysics: Nanoparticles and Quantum Dots*. (CRC Press, 2010).
7. M. Reibold, P. Paufler, A. A. Levin, W. Kochman, N. Patzke and D. C. Meyer, *Nature,* 2006, **444**, 286.
8. S. Iijima, *Nature,* 1991**, 354,** 56–58.
9. C. W. Chang, J. M. Tseng, J. J. Horng, and C. M. Shu, *Compos. Sci. Technol.* 2008, **68,** 2954–2959.
10. X. Gong, J. Liu, S. Baskaran, R. D. Voise, and J. S. Young, *Chem. Mater.* 2000, **12,** 1049–1052.
11. R. F. Service, *Science,* 1998, **281,** 940–942.
12. H, Dai, J. H. Hafner, A. G. Rinzler, D. T. Colbert, and R. E. Smalley, *Nature,* 1996, **384,** 147–150.
13. A. C. Dillon, K. M. Jones, T. A. Bekkedahl, C. H. Kiang, D. S. Bethune, and M. J. Heben, *Nature,* 1997, **386,** 377–379.
14. C. Nguyen, L. Delzeit, A. Cassell, and J. Li, *Nano Lett.,* 2002, **2,** 1079–1081.
15. W. Krätschmer, L. D. Lamb, K. Fostiropoulos, and D. R. Huffman, *Nature,* 1990, **347,** 354–358.
16. M. Jose-Yachman, M. Miki-Yoshidam, and L. Rendon, *Appl. Phys. Lett.,* 1993, **62,** 657–659.
17. T. Guo, M. D. Diener, Y. Chai, M. J. Alford, R. E. Haufler, S. M. McClure, T. Ohno, J. H. Weaver, G. E. Scuseria, and R. E. Smalley, *Science,* 1992, **257,** 1661–1664.
18. M. S. Dresselhaus, G. Dresselhaus, and R. Saito, *Carbon,* 1995, **33,** 883–891.
19. H. Zhang, B. Wu, W. Hu, and Y. Liu, *Chem. Soc. Rev.*, 2011, **40,** 1324–1336.
20. J. W. G. Wilder, L. C. Venema, A. G. Rinzler, R. E. Smalley, and C. Dekker, *Nature,* 1998, **391,** 59–62.
21. P. C. Eklund, J. M. Holden, abd R. A Jishi, *Carbon*, 1995, **33,** 959–972.
22. J. W. Mintmire, B. I. Dunlap, and C. T. White, *Phys. Rev. Lett.,* 1992, **68,** 631–634.

23. C. Dekker, *Technology,* 1999, **52,** 22–28.

24. R. Martel, V. Derycke, C. Lavoie, J. Appenzeller, K. K. Chan, J. Tersoff, and Ph Avouris, *Phys. Rev. Lett.,* 2001, **87,** 256805-1 - 256805-4.

25. H. Kataura, Y. Kumazawa, Y. Maniwa, L. Umezu, S. Suzuki, Y. Ohtsuka, and Y. Achiba, *Synth. Met.,* 1999, **103,** 2555–2558.

26. R. B. Weisman, and S. M. Bachilo, *Nano Lett.,* 2003, **3,** 1235–1238.

27. G. Sánchez-Pomales, C. Pagan-Miranda, L. Santiago-Rodriguez, and C. R. Cabrera, *Carbon Nanotubes,* 2010.

28. V. Georgakilas, D. Gournis, V. Tzitzios, L. Pasquato, and M. Guldi, *J. Mater. Chem.* 2007, **17,** 2679-2694.

29. D. Eder, *Chem. Rev.* 2010, **110,** 1348-1385.

30. X. Guo, *Adv. Mater.* 2013, **25,** 3397–3408.

31. S. E. Kooi, U. Schlecht, M. Burghard, and K. Kern, *Angew. Chemie Int. Ed.,* 2011, **41**, 1353–1355.

32. K. Balasubramanian, R. Sordan, M. Burghard, and Kern, K. *Nano Lett.,* 2004, **4,** 827–830.

33. K. Balasubramanian, M. Friedrich, C. Jiang, Y. Fan, A. Mews, M. Burghard, and K. Kern, *Adv. Mater.,* 2003, **15,** 1515–1518.

34. V. Ivanov, A. Fonseca, J. B. Nagy, A. Lucas, P. Lambin, D. Bernaerts, and X. B. Zhang, *Carbon,* 1995, **33,** 1727–1738.

35. J. Liu, A. G. Rinzler, H. Dai, J. H. Hafner, R. K. Bradley, P. J. Boul, A. Lu, T. Iverson, K. Shelimov, C. B. Huffman, F. Rodriguez-Macias, Y. S. Shon, T. R. Lee, D. T. Colbert, and R. E. Smalley, *Science,* 1998, **280,** 1253–1256.

36. J. Chen, M. A. Hamon, H. Hu, Y. Chen, A. M. Rao, P. C. Eklund, and R. C. Haddon, *Science,* 1998, **282,** 95–98.

37. Z. Liu, Z. Shen, T. Zhu, S. Hou, and L. Ying, *Langmuir,* 2000, **16,** 3569–3573.

38. J. K. Lim, W. S. Yun, M. Yoon, S. K. Lee, C. H. Kim, K. Kim, and S. K. Kim, *Synth. Met.* 2003, **139,** 521–527.

39. D. Tasis, N. Tagmatarchis, A. Bianco, and M. Prato, *Chem. Rev.,* 2006, **106,** 1105–1136.

40. C. G. Salzmann, M. A. H. Ward, R. M. J. Jacobs, G. Tobias, and M. L. H. Green, *J. Phys. Chem. C* 2007, **111,** 18520–18524.

41. M. Zheng, A. Jagota, E. D. Semke, B. A. Diner, R. S. Mclean, S. R. Lustig, R. E. Richardson, and N. G. Tassi, *Nat. Mater.,* 2003, **2,** 338–342.

42. M. Zheng, and E. D. Semke, *J. Am. Chem. Soc.,* 2007, **129,** 6084–6085.

43. M. Zheng, A. Jagota, M. S. Strano, A. P. Santos, P. Barone, S. G. Chou, and B. A. Din, *Science,* 2003, **302,** 1545–1548.

44. G. I. Dovbeshko, O. P. Repnytska, E. D. Obraztsova, and Y. V. Shtogun, *Chem. Phys.*

Lett., 2003, **372,** 432–437.

45. G. I. Dovbeshko, O. P. Repnytska, E. D. Obraztsova, Y. V. Shtogun, and E. O. Andreev, *Semicond. Physics, Quantum Electron. Optoelectron.* 2003, **6,** 105–108.

46. N. Nakashima, S. Okuzono, H. Murakami, T. Nakai, and K. Yoshikawa, *Chem. Lett.* 2003, **32,** 456–457.

47. G. K.-C. Lee, C. Sach, M. L. H. Green, L. Wong, and C. Salzmann, *Chem. Commun.* 2010, **46,** 7013–7015.

48. Y. Ma, S. R. Ali, A. S. Dodoo, and H. He, *J. Phys. Chem. B,* 2006, **110,** 16359–16365.

49. Y. Xu, P. E. Pehrsson, L. Chen, R. Zhang, and W. Zhao, *J. Phys. Chem. C,* 2007, **111,** 8638–8643.

50. Z. Liang, R. Lao, J. Wang, Y. Liu, L. Wang, Q. Huang, S. Song, G. Li, and C. Fan, *Int. J. Mol. Sci.,* 2007, **8,** 705–713.

51. W. Zhao, Y. Gao, M. Brook, and Y. Li, *Chem. Commun. (Camb).,* 2006, **1,** 3582–3584.

52. B. Gigliotti, B. Sakizzie, D. S. Bethune, R. M. Shelby, and J. N. Cha, *Nano Lett.* 2006, ***6,*** 159 - 164.

53. S. R. Vogel, M. M. Kappes, F. Hennrich, and C. Richert, *Chem. - A Eur. J.,* 2007, **13,** 1815–1820.

54. Q. H. Yang, Q. Wang, N. Gale, C. J. Oton, I. S. Nandhakumar, Z. Zhu, Z. Tang, T. Brown, and W. H. Loh, *Nanotechnology,* 2009, **20,** 195603.

55. G. N. Ostojic, J. R. Ireland, and M. C. Hersam, *Langmuir,* 2008, **24,** 9784–9789.

56. Y. Li, X. Han, and Z. Deng, *Angew. Chemie - Int. Ed.,* 2007, **46,** 7481–7484.

57. Y. Chen, H. Liu, T. Ye, J. Kim, and C. Mao, *J. Am. Chem. Soc.*, 2007, **129,** 8696–8697.

58. J. F. Campbell, I. Tessmer, H. H. Thorp, and D. A. Erie, *J. Am. Chem. Soc.,* 2008, **130,** 10648–10655.

59. H. A. Heering, K. A. Williams, S. De Vries, and C. Dekker, *ChemPhysChem* 2006, **7,** 1705–1709.

60. C. Cao, J. H. Kim, Y-J. Kwon, Y-J. Kim, E-S. Hwang, and S. Baik *Analyst,* 2009, **134,** 1294–1296.

61. Z. Zhu, Z. Tang, J. A. Phillips, R. Yang, H. Wang, and W. Tan, *J Am Chem Soc.,* 2008, **130,** 10856–10857.

62. Y. Ma, S. R. Ali, L. Wang, P. L. Chiu, R. Mendelsohn, and H. He, *J. Am. Chem. Soc.,* 2006, **128,** 12064–12065.

63. H. Takahashi, S. Numao, S. Bandow, and S. Iijima, *Chem. Phys. Lett.,* 2006, **418,** 535–539.

64. J. Rajendra, M. Baxendale, L. G. D. Rap, and A. Rodger, *J. Am. Chem. Soc.,* 2004, **126,** 11182–11188.

65. M. Shoda, S. Bandow, Y. Maruyama, and S. Lijima, *J. Phys. Chem. C.*, 2009, **113,** 6033–6036.

66. S. Meng, W. L. Wang, P. Maragakis, E. Kaxiras, *Nano Lett.*, 2007, **7,** 2312–2316.

67. G. Sánchez-Pomales, and C. R. Cabrera, *J. Electroanal. Chem.*, 2007, **606,** 47–54.

68. D. Nepal, J. I. Sohn, W. K. Aicher, S. Lee, and K. E. Geckeler, *Biomacromolecules*, 2005, **6,** 2919–2922.

69. M. Iijima, T. Watabe, S. Ishii, A. Koshio, T. Yamaguchi, S. Bandow, S. Iijima, K. Suzuki, and Y. Maruyama, *Chem. Phys. Lett.*, 2005, **414,** 520–524.

70. J. Rajendra, and A. Rodger, *Chem. - A Eur. J.*, 2005, **11,** 4841–4847.

71. E. K. Hobbie, B. J. Bauer, J. Stephens, M. L. Becker, P. McGuiggan, S. D. Hudson, and H. Wang, *Langmuir*, 2005, **21,** 10284–10287.

72. S. Badaire, C. Zakri, M. Maugey, A. Derre, J. N. Barisci, G. Wallace, and P. Poulin, *Adv. Mater.*, 2005, **17,** 1673–1676.

73. Z. Luo, L. D. Pfefferle, G. L. Haller, and F. Papadimitrakopoulos, *J. Am. Chem. Soc.*, 2006, **128,** 15511–15516.

74. C. Hu, Y. Zhang, G. Bao, Y. Zhang, M. Liu, and Z. L. Wang, *J. Phys. Chem. B.*, 2005, **109,** 20072–20076.

75. Y. Li, B. G. Cousins, R. V. Ulijn, and I. a. Kinloch, *Langmuir*, 2009, **25,** 11760–11767.

76. C. Y. Khripin, M. Zheng, and A. Jagota, *J. Colloid Interface Sci.*, 2009, **330,** 255–265.

77. H. Qian, P. T. Araujo, C. Georgi, T. Gokus, N. Hartmann, A. A. Green, A. Jorio, M. C. Hersam, L. Novotny, and A. Hartschuh, *Nano Lett.*, 2008, **8,** 2706–2711.

78. S. Toita, D. Kang, K. Kobayashi, H. Kawamoto, K. Kojima, and M. Tachibana, *Diam. Relat. Mater.*, 2008, **17,** 1389–1393.

79. S. G. Chou, H. B. Ribeiro, E. B. Barros, A. P. Santos, D. Nezich, G. G. Samsonidze, C. Fantini, M. A. Pimenta, A. Jorio, F. Plentz Filho, M. S. Dresselhaus, G. Dresselhaus, R. Saito, M. Zheng, G. B. Onoa, E. D. Semke, A. K. Swan, M. S. Unlu, and B. B. Goldberg, *Chem. Phys. Lett.*, 2004, **397,** 296–301.

80. M. S. Strano, M. Zheng, A. Jagota, B. Onoa, D. A. Heller, P. W. Barone, and M. L. Usrey, *Nano Lett.*, 2004, **4,** 543–550.

81. M. S. Arnold, A. A. Green, J. F. Hulvat, S. I. Stupp, and M. C. Hersam, *Nat. Nanotechnol.*, 2006, **1,** 60–65.

82. X. Peng, N. Komatsu, T. Kimura, and A. Osuka, *J. Am. Chem. Soc.*, 2007, **129,** 15947–15953.

83. X. Tu, S. Manohar, A. Jagota, and M. Zheng, *Nature*, 2009, **460,** 250–253.

84. J. A. Fagan, E. H. Haroz, R. Ihly, H. Gui, J. L. Blackburn, J. R. Simpson, S. Lam, A. R. Hight Walker, S. K. Doorn, and M. Zheng, *ACS Nano.*, 2015, **9,** 5377–5390.

85. H. Gui, J. K. Streit, J. A. Fagan, A. R. Hight Walker, C. Zhou, and M. Zheng, *Nano*

Lett., 2015, **15**, 1642-1646.

86. M. A. Reed, *Science*, 1997, **278,** 252–254.

87. D. Porath, A. Bezryadin, S. de Vries, and C. Dekker, *Nature*, 2000, **403,** 635–638.

88. X. D. Cui, A. Primark, X. Zarate, J. Tomfohr, O. F. Sankey, A. L. Moore, D. Gust, G. Harris, and S. M. Li, *Science*, 2001, **294,** 571–574.

89. B. Xu, and N. J. Tao, *Science*, 2003, **301,** 1221–1223.

90. T. Dadosh, Y. Gordin, R. Krahne, I. Khivrich, D. Mahalu, V. Frydman, J. Sperling, A. Yacoby, and I. Bar-Joseph, *Nature*, 2005, **436,** 677–680.

91. J. Park, A. N. Pasupathy, J. I. Goldsmith, C. Chang, Y. Yaish, J. R. Petta, M. Rinkoski, J. P. Sethna, H. D. Abruna, P. L. McEuen, and D. C. Ralph, *Nature*, 2002, **417,** 722–725.

92. W. Liang, M. P. Shores, M. Bockrath, J. R. Long, H. P. Kondo, *Nature*, 2002, **417,** 725–729.

93. G. V. Nazin, X. H. Qiu, and W. Ho, *Science*, 2003, **302,** 77–81.

94. N. P. Guisinger, N. L. Yoder, and M. C. Hersam, *Proc. Natl. Acad. Sci.*, 2005, **102,** 8838–8843.

95. P. G. Piva, G. A. DiLabio, J. L. Pitters, J. Zikovsky, M. Rezeq, S. Dogel, W. A. Hofer, and R. A. Wolkow, *Nature*, 2005, **435,** 658–661.

96. A. K. Feldman, M. L. Steigerwald, X. Guo, and C. Nuckolls, *Acc. Chem. Res.*, 2008, **41,** 1731–1741.

97. A. Aviram, and M. A. Ratner, *Chem. Phys. Lett.*, 1974, **29,** 277-283.

98. A. Nitzan, and M. A. Ratner, *Science*, 2003, **300,** 1384–1389.

99. P. Gehring, H. Sadeghi, S. Sangtarash, C. S. Lau, J. Liu, A. Ardavan, J. H. Warner, C. J. Lambert, G. A. D. Briggs, and J. A. Mol, *Nano Lett.*, 2016, **16,** 4210-4216.

100. Z. B. Henson, K. Müllen, and G. C. Bazan, *Nat. Chem.*, 2012, **4,** 699–704.

101. P. Reddy, S. -Y. Jang, R. Segalman, and A. Majumdar, *Science* 2007, **315,** 1568–1571.

102. G. Schwartz, B. C.-K. Tee, J. Mei, A. L. Appleton, D. H. Kim, H. Wang, and Z. Bao, *Nat. Commun.*, 2013, **4,** 1-8.

103. J. You, L. Dou, K. Yoshimura, T. Kato, K. Ohya, T. Moriarty, K. Emery, C.-C Chen, J. Gao, G. Li, and Y. Yang, *Nat. Commun.*, 2013, **4,** 1-8.

104. G. Gustafsson, Y. Cao, G. M. Treacy, F. Klavetter, N. Colaneri, and A. J. Heeger, *Nature*, 1992, **357,** 477–479.

105. B. A. Facchetti, M. Mushrush, H. E. Katz, and T. J. Marks, *Adv. Mater.*, 2003, **15,** 33–38.

106. H. E. Katz, A. J. Lovinger, J. Johnson, C. Kloc, T. Siegrist, W. Li, Y.-Y. Lin, and A Dodabalapur, *Nature*, 2000, **404,** 478–481.

107. J. E. Anthony, A. Facchetti, M. Heeney, S. R. Marder, and X. Zhan, *Adv. Mater.*,

2010, **22,** 3876–3892.

108. H. Park, A. K. L. Lim, A. P. Alivisatos, J. Park, and P. L. McEuen, *Appl. Phys. Lett.,* 1999, **75,** 301–303.

109. H. C. Manoharan, C. P. Lutz, and D. M. Eigler, *Nature,* 2000, **403,** 512–515.

110. M. F. Crommie, C. P. Lutz, and D. M. Eigler, *Nature,* 1993, **363,** 524–527.

111. J. Repp, G. Meyer, S. M. Stojković, A. Gourdon, and C. Joachim, *Phys. Rev. Lett.,* 2005, **94,** 1–4.

112. D. J. Wold, and C. D. Frisbie, *J. Am. Chem. Soc.,* 2000, **122,** 2970–2971.

113. D. J. Wold, and C. D. Frisbie, *J. Am. Chem. Soc.,* 2001, **123,** 5549–5556.

114. V. B. Engelkes, J. M. Beebe, and C. D. Frisbie, *J. Am. Chem. Soc.,* 2004, **126,** 14287–14296.

115. X. Guo, J. Small, J. Klare, and Y. Wang, *Science,* 2006, **311,** 356–359.

116. X. Guo, A. Whalley, J. E. Klare, L. Huang, S. O'Brien, M. Steigerwald, and C. Nuckolls, *Nano Lett.,* 2007, **7,** 1119–1122.

117. X. Guo, A. A. Gorodetsky, J. Hone, J. K. Barton, and C. Nuckolls, *Nat. Nanotechnol.,* 2008, **3,** 163–167.

118. H. Wang, N. B. Muren, D. Ordinario, A. A. Gorodetsky, J. K. Barton, and C. Nuckolls, *Chem. Sci.,* 2012, **3,** 62-65.

119. C. Jia, A. Migliore, N. Xin, S. Huang, J. Wang, Q. Yang, S. Wang, H. Chen, D. Wang, B. Feng, Z. Liu, G. Zhang, D.-H. Qu, H. Tian, M. A. Ratner, H. Q. Xu, A. Nitzan, and X. Guo, *Science,* 2016, **352,** 1443–1446.

120. M. Palma, W. Wang, E. Penzo, J. Brathwaite, M. Zheng, J. Hone, C. Nuckolls, and S. J. Wind, *J. Am. Chem. Soc.,* 2013, **135,** 8440–8443.

121. L. Sun, Y. A. Diaz-Fernandez, T. A. Gschneidtner, F. Westerlund, S. Lara-Avila, and K. Moth-Poulsen, *Chem. Soc. Rev.,* 2014, **43,** 7378–7411.

122. T. Jain, Q. Tang, T. Bjørnholm, and K. Nørgaard, *Acc. Chem. Res.,* 2014, **47,** 2–11.

123. Q. Tang, Y. Tong, T. Jain, T. Hassenkam, Q. Wan, K. Moth-Poulsen, T. Bjørnholm, *Nanotechnology,* 2009, **20,** 245205.

124. T. Jain, S. Lara-Avila, Y.-V. Kervennic, K. Moth-Poulsen, K. Nørgaard, S. Kubatkin, and T. Bjørnholm, *ACS Nano,* 2012, **6,** 3861–3867.

125. T. Hassenkam, K. Moth-Poulsen, N. Stuhr-Hansen, K. Nørgaard, M. S. Kabir, and T. Bjørnholm, *Nano Lett.,* 2004, **4,** 19–22.

126. E. Meyer, Atomic Force Microscopy. *Prog. Surf. Sci.,* 1992, **41,** 3–49.

127. G. Binnig, C. Gerber, E. Stoll, and T. R. Albrecht, *Surf. Sci.,* 1987, **1281,** 1-6.

128. Q. Zhong, D. Innis, K. Kjoller, and V. B. Elings, *Surf. Sci. Lett.,* 1993, **290,** L688–L692.

129. D. A. Bonnell, and R. L. Shao, *Curr. Opin. Solid State Mater. Sci.,* 2003, **7,** 161–171.

130. E. Ruska, and H. Rohrer, *Science,* 1932, **234,** 822–821.

131. M. M. Freundlich, *Science,* 1963, **142,** 185–188.

132. B. Zhong, and L. Wang, *Adv. Mater.,* 2003, **15,** 1497–1514.

133. G. E. Moore, *Proc. IEEE,* 1998, **86,** 82–85.

134. S. J. Wind, D. J. Frank, and H.-S. Wong, *Microelectron. Eng.,* 1996, **32,** 271–282.

135. S. Thompson, S. Parthasarathy, *Mater. Today,* 2006, **9,** 20–25.

136. J. Robertson, *Mater. today,* 2007, **10,** 36–43.

137. Q. Shen, X. Guo, M. L. Steigerwald, and C. Nuckolls, *Chemistry - An Asian Journal,* 2010, **5,** 1040–1057.

138. J. R. Heath, *Annu. Rev. Mater. Res.,* 2009, **39,** 1–23.

139. M. Ratner, *Nat. Nanotechnol.,* 2013, **8,** 378–381.

140. N. J. Tao, *Nat. Nanotechnol.,* 2006, **1,** 173–181.

141. S. M. Lindsay, and M. A. Ratner, *Adv. Mater.,* 2007, **19,** 23–31.

142. K. Moth-Poulsen, and T. Bjørnholm, *Nat. Nanotechnol.,* 2009, **4,** 551–556.

143. C. Jia, and X. Guo, *Chem. Soc. Rev.,* 2013, **42,** 5642–5660.

144. L. Sun, Y. A. Diaz-Fernandez, T. A. Gschneidtner, F. Westerlund, S. Lara-Avila, and K. Moth-Poulsen, *Chem. Soc. Rev.,* 2014, **43,** 7378–7411.

145. M. L. Perrin, E. Burzurí, and H. S. J. van der Zant, *Chem. Soc. Rev.,* 2015, **44,** 902–919.

146. S. V. Aradhya, and L. Venkataraman, *Nat. Nanotechnol.,* 2013, **8,** 399.

147. I. Diez-Perez, J. Hihath, T. Hines, Z.-S. Wang, G. Zhou, K. Mullen, and N. Tao, *Nat. Nanotechnol.,* 2011, **6,** 226–231.

148. D. Xiang, H. Jeong, D. Kim, T. Lee, Y. Cheng, Q. Wang, and D. Mayer, *Nano Lett.,* 2013, **13,** 2809–2813.

149. C. Grupe, *Nat. Nanotechnol.,* 2013, **8,** 385–389.

150. Y. Cao, S. Dong, S. Liu, Z. Liu, and X. Guo, *Angew. Chemie - Int. Ed.,* 2013, **52,** 3906–3910.

151. C. W. Marquardt, S. Grunder, A Blaszczyk, S. Dehm, F. Hennrich, H. v Lohneysen, M. Mayor, and R. Krupke, *Nat. Nanotechnol.,* 2010, **5,** 863–867.

152. Y. Cao, S. Dong, S. Liu, L. He, L. Gan, X. Yu, M. L. Steigerwald, X. Wu, Z. Liu. and X. Guo, *Angew. Chemie - Int. Ed.,* 2012, **51,** 12228–12232.

153. C. Thiele, H. Vieker, A. Beyer, B. S. Flavel, F. Hennrich, D. M. Torres, T. R. Eaton, M. Mayor, M. M. Kappes, A. Golzhauser, H. v Lohneysen, and R. Krupke, *Appl. Phys. Lett.,* 2014, **104,** 103102.

154. H. Yan, A. J. Bergren, and R. L. McCreery, *J. Am. Chem. Soc.,* 2011, **133,** 19168–19177.

155. M. J. Loiacono, E. L Granstrom, and C. D. Frisbie, *J. Phys. Chem. B*, 1998, **102,** 1679–1688.

156. X. Tu, S. Manohar, A. Jagota, and M. Zheng, *Nature*, 2009, **460,** 250–253.

157. P. Riesz, and T. Kondo, *Free Radic. Biol. Med.*, 1992, **13,** 247–270.

158. A. C. Whalley, M. L. Steigerwald, X. Guo, and C. Nuckolls, *J Am Chem Soc.*, 2007,**129,** 12590–12591.

159. L. Venkataraman, J. Klare, and C. Nuckolls, *Nature*, 2006, **442,** 904–907.

160. P. Samorí, V. Francke, K. Müllen, and J. P. Rabe, *Chem. - A Eur. J.*, 1999, **5,** 2312–2317.

161. C. Adamo, and V. Barone, *J. Chem. Phys.* 1999, **110,** 6158.

162. S. Grimme, J. Antony, S. Ehrlich, and H. Krieg, *J. Chem. Phys*,. 2010, **132,** 154104.

163. A. Klamt, and G. Schüürmann, *J. Chem. Soc. Trans.*, 1993, **2**, 799–805.

164. A. Schäfer, H. Horn, and R. Ahlrichs, *J. Chem. Phys.*, 1992, **97,** 2571.

165. C. Gómez-Navarro, P. J. De Pablo, J. Gomez-Herrero, B. Biel, F. J. Garcia-Vidal, A. Rubio, and F. Flores, *Nat. Mater.*, 2005, **4,** 534–539.

166. A. Javey, J. Guo, Q. Wang, M. Lundstrom, and H. Dai, *Nature*, 2003, **424,** 654–657.

167. D. J. Wold, R. Haag, M. A. Rampi, and C. D. Frisbie, *J. Phys. Chem. B*, 2002, **106,** 2813–2816.

168. T. Kim, Z.-F. Liu, C. Lee, J. B. Neaton, and L. Venkataraman, *Proc. Natl. Acad. Sci.*, 2014, **111,** 10928–10932.

169. G. Ao, C. Khripin, and M. Zheng, *J. Am. Chem.* 2014, **136,** 10383-10392.

170. R. S. McLean, X. Huang, C. Khripin, A. Jagota, and M. Zheng, *Nano Lett.*, 2006, **6,** 55–60.

171. G. Ao, and M. Zheng, *Curr. Protoc. Chem. Biol.*, 2015, **7,** 43–51.

172. J. Zhu, J. McMorrow, R. Crespo-Otero, G. Ao, M. Zheng, W. P. Gillin, and M. Palma, *J. Am. Chem. Soc.*, 2016, **138,** 2905–2908.

173. G. E. Moore, *Technol. Int.*, 1965.

174. J. E. Lilienfeld, *US Patent*, 1930, *1,745,175*, 1–4

175. I. M. Ross, *Phys. Today*, 1997, **50,** 34.

176. J. Millman, C. C. Halkias, Electronic Devices and Circuits, McGraw-Hill, (1967).

177. D. H. Waldeck, and D. N. Beratan, *Science*, 1993, **261,** 576–577.

178. T. Hertel, R. Martel, and P. Avouris, *J. Phys. Chem.*, 1998, **5647,** 910–915.

179. Y. Y. Liang, H. Chen, H. Mizuseki, and Y. Kawazoe, *J. Chem. Phys.*, 2011, **134,** 144113.

180. M. Galperin, M. A. Ratner, A. Nitzan, T. Shimazaki, and K. Yamashita, *Nanotechnology* 2007, **18,** 424012.

181. M. Di Ventra, S. T. Pantelides, and N. D. Lang, *Appl. Phys. Lett.* 2000, **76,** 3448.

182. E. A. Osorio, T. Bjørnholm, J.-M. Lehn, M. Ruben, and H. S. J. van der Zant, *J. Phys. Condens. Matter*, 2008, **20,** 374121.

183. Y. Xu, C. Fang, B. Cui, G. Ji, Y. Zhai, and D. Liu, *Appl. Phys. Lett.* 2011, **99,** 043304.

184. S. Ke, H. U. Baranger, and W. Yang, *Phys. Rev. B,* 2005, **71,** 113401.

185. B. Xu, X, Xiao, X. Yang, L. Zang, and N. Tao, *J Am Chem Soc*, 2005, **127,** 2386–2387.

186. N. Tao, *J. Mater. Chem.*, 2005, **15,** 3260–3263.

187. S. Grunder, R. Huber, S. Wu, M. Calame, and M. Mayor, *Chimia (Aarau).*, 2010, **64,** 140–144.

188. H. S. White, G. P. Kittlesen, and M. S. Wrighton, *J Am Chem Soc*, 1984, **106,** 5375–5377.

189. Z. K. Keane, J. W. Ciszek, J. M. Tour, and D. Natelson, *Nano. Lett.*, 2006, **6,** 1518-1521.

190. A. W. Ghosh, T. Rakshit, and S. Datta, *Nano Lett.* 2004, **4,** 565–568.

191. A. P. Alivisatos, and P. L. Mceuen, *Nature*, 2000, **407,** 57–60.

192. C. A. Martin, J. M. Van Ruitenbeek, and H. S. J. van der Zant, *Nanotechnology* 2010, **21,** 265201.

193. V. V. Rostovtsev, L. G. Green, V. V. Fokin, and K. B. Sharpless, *Angew. Chemie - Int. Ed.* 2002, **41,** 2596–2599.

194. K. Sonogashira, *J. Organomet. Chem.* 2002, **653,** 46–49.

195. K. Sonogashira, Y. Tohda, and N. Hagihara, *Tetrahedron Lett.*, 1975, **16,** 4467–4470.

196. A. L. Kohnen, R. L. Danheiser, S. E. Denmark, and X. Liu, *Org. Synth.*, 2007, **84,** 77–87.

197. S. Frigoli, C. Fuganti, L. Malpezzi, and S. Serra, *Org. Process Res. Dev.*, 2005, **9,** 646–650.

198. A. O. King, and N. Yasuda, *Organometallics Process Chem.*, 2004, **6,** 205–245.

199. A. Pinto, L. Neuville, and J. Zhu, *Angew. Chemie - Int. Ed.*, 2007, **46,** 3291–3295.

200. B. Soberats, L. Martínez, M. Vega, C. Rotger, and A. Costa, *Adv. Synth. Catal.*, 2009, **351,** 1727–1731.

201. D. A. Alonso, C. Nájera, and M. C. Pacheco, *Adv. Synth. Catal.*, 2003, **345,** 1146–1158.

202. M. J. Mio, L. C. Kopel, J. B. Braun, T. L. Gadzikwa, K. L. Hull, R. G. Brisbois, C. J. Markworth, and P. A. Grieco, *Org. Lett.*, 2002, **4,** 3199–3202.

203. T. Hundertmark, A. F. Littke, S. L. Buchwald, and G. C. Fu, *Org. Lett.*, 2000, **2,** 1729–1731.

204. A. Koellhofer, and H. A. Plenio, *Adv. Synth. Catal.*, 2005, **347,** 1295–1300.

205. R. A. Batey, M. Shen, and A. J. Lough, *Org. Lett.*, 2002, **4,** 1411–1414.

206. Y. Liang, Y. Xie, and J. Li, *J. Org. Chem.*, 2006, **71,** 379–381.

207. B. Liang, M. Dai, J. Chen, and Z. Yang, *J. Org. Chem.*, 2005, **70,** 391–393.

208. A. Soheili, J. Albaneze-Walker, J. A. Murry, P. G. Dormer, and D. L. Hughes, *Org. Lett.*, 2003, **5,** 4191–4194.

209. A. Komáromi, and Z. Novák, *Chem. Commun. (Camb).*, 2008, **0,** 4968–4970.

210. R. Widenhoefer, and S. Buchwald, *Organometallics*, 1996, **7333,** 3534–3542.

211. M. S. Wang, J. Y. Wang, Q. Chen, and L.-M Peng, *Adv. Funct. Mater.*, 2005, **15,** 1825–1831.

212. R. Baughman, A. Zakhidov, and W. de Heer, *Science*, 2002, **297,** 787–792.

213. G. S. Roberts, and P. Singjai, *Nanoscale*, 2011, **3,** 4503.

214. S. K. Doorn, M. J. O'Connell, L. Zheng, Y. T. Zhu, S. Huang, and J. Liu, *Phys. Rev. Lett.*, 2005, **94,** 1–4.

215. L. B. Ruppalt, and J. W. Lyding, *Small*, 2007, **3,** 280–284.

216. Z. Osvath, A. A. Koos, Z. E. Horvath, J. Gyulai, A. M. Benito, M. T. Martinez, W. K. Maser, and L. P. Biro, *Chem. Phys. Lett.*, 2002, **365,** 338–342.

217. M. Ouyang, *Science*, 2001, **291,** 97–100.

218. C. Jin, K. Suenaga, and S. Iijima, *Nat. Nanotechnol.*, 2008, **3,** 17–21.

219. M. Sano, A. Kamino, J. Okamura, and S. Shinkai, S*cience*, 2001, **1299,** 1299–1301.

220. P. W. Chiu, G. S. Duesberg, U. Dettlaff-Weglikowska, and S. Roth, *Appl. Phys. Lett.*, 2002, **80,** 3811–3813.

221. D. M. Chenoweth, M. Timothy, and C. Link, *J Am Chem Soc.*, 2010, **132,** 14009–14011.

222. M. Sano, A. Kamino, and S. Shinkai, *Angew. Chemie - Int. Ed.*, 2001, **40,** 4661–4663.

223. C. Do, H. S. Jang, and S. M. Choi, *J. Chem. Phys.* 2013, **138,** 114701.

224. T.-H. Kim, C. Do, S.-H Kang, M.-J. Lee, S.-H. Lim, and S.-M. Choi, *Soft Matter*, 2012, **8,** 9073.

225. C. Doe, H. S. Jang, T. H. Kim, S. R. Kline, and S. M. Choi, *J. Am. Chem. Soc.*, 2009, **131,** 16568–16572.

226. H.-S. Jang, T.-H. Kim, C. Do, M.-J. Lee, and S.-M. Choi, *Soft Matter* 2013, **9,** 3050.

227. S. H. Lim, H.-S. Jang, J.-M. Ha, T.-H. Kim, P. Kwasniewski, T. Narayanan, K. S. Jin, and S.-M. Choi, *Angew. Chemie - Int. Ed.*, 2014, **53,** 12548–12554.

228. F. Cannone, G. Chirico, A. R. Bizzarri, and S. Cannistraro, *J. Phys. Chem. B*, 2006, **110,** 16491–16498.

229. H. T. Maune, S. Han, R. D. Barish, M. Bockrath, W. A. Goddard, P. W. K. Rothemund, and E. Winfree, *Nat. Nanotechnol.*, 2010, **5,** 61–66.

230. G. Dukovic, M. Balaz, P. Doak, N. D. Berova, M. Zheng, R. S. Mclean, and L. E. Brus, *J. Am. Chem. Soc.*, 2006, **128,** 9004–9005.

231. M. Pumera, *J. Nanosci. Nanotechnol.*, 2009, **9,** 2671–2676.

232. S. Han, H. Maune, R. Barish, M. Bockrath, and W. A. Goddard, *Nano Lett.*, 2012, **12,** 1129–1135.

233. C. Zhao, K. Qu, J. Ren, and X. Qu, X. *Chem. Eur. J.* 7013–7019 (2011).

234. C. Zhao, K. Qu, C. Xu, J. Ren, and X. Qu, *Nucleic Acid Res.*, 2011, **39,** 3939–3948.

235. H. Sun, J. Ren, and X. Qu, *Acc. Chem. Res.* 2015, **49,** 461-470.

236. A. Cao, *Science*, 2005, **310,** 1307–1310.

237. Y.-L. Li, I. A. Kinloch, and A. H. Windle, *Science*, **304,** 276–278 (2004).

238. J. Miyamoto, Y. Hattori, D. Noguchi, H. Tanaka, T. Ohba, S. Utsumi, H. Kanoh, Y. A. Kim, H. Muramatsu, M. Endo, and K. Kaneko, *J. Am. Chem. Soc.*, 2006, **128,** 12636–12637.

239. J. Zou, J. Liu, A. S. Karakoti, A. Kumar, D. Joung, Q. Li, S. I. Khondaker, S. Seal, and L. Zhair, *ACS Nano*, 2010, **4,** 7293–7302.

240. P. Siemsen, R. C. Livingston, and F. Diederich, *Angew. Chem. Int. Ed. Engl.*, 2000, **39,** 2632–2657.

241. J. E. Hein, and V. V. Fokin, *Chem. Soc. Rev.*, 2010, **39,** 1302–1315.

242. V. O. Rodionov, S. I Presolski, D. D. Diaz, V. V. Fokin, & M. G. Finn, *J. Am. Chem. Soc.*, 2007, **129,** 2210–2215.

243. B. F. Straub, *Chem. Commun*, 2007, 3868–3870.

244. H. C. Kolb, M. G. Finn, and K. B. Sharpless, *Angew. Chemie - Int. Ed.*, 2001, **40,** 2004–2021.

245. H. Deng, E. Bilotti, R. Zhang, and T. Peijs, *J. Appl. Polym. Sci.*, 2010, **118,** 30–41.

246. Z. Wang, E. Bilotti, and T. Peijs, *Adv. Compos. Lett.*, 2010, **19,** 182–187.

247. X. Zhang, T. Liu, T. V. Sreekumar, S. Kumar, V. C. Moore, R. H. Hauge, and R. E. Smalley, *Nano Lett.*, 2003, **3,** 1285–1288.

248. S. S. Pujari, H. Xiong, and F. Seela, *J. Org. Chem.*, 2010, **75,** 8693–8696.

249. H. Xiong, and F. Seela, *Bioconjug. Chem.*, 2012, **23,** 1230–1243.

250. S. S. Pujari, and F. Seela, *J. Org. Chem.*, 2012, **77,** 4460–4465.

251. S. S. Pujari, S. A. Ingale, and F. Seela, *Bioconjug. Chem.*, 2014, **25,** 1855–1870.